SunFesT

(http://www.seas.upenn.edu/sunfest/)

2014

SUMMER UNDERGRADUATE FELLOWSHIPS IN SENSOR TECHNOLOGIES

TECHNICAL REPORT
TR-CST AUG 2014

Center for Sensor Technologies
University of Pennsylvania
Philadelphia, PA 19104

Acknowledgement

This material is based upon work supported by the National Science Foundation under Grant No.1062672.

Disclaimer


CAGD

SUNFEST 2014

SUMMER UNDERGRADUATE FELLOWSHIP IN SENSOR TECHNOLOGIES

Sponsored by the National Science Foundation (Award no. 1062672)

From June 2 through August 8, 2014 ten students participated in the SUNFEST program, which is organized by the Center for Sensor Technologies of the School of Engineering and Applied Science at the University of Pennsylvania. This unique "Summer Experience for Undergraduates in Sensor Technologies" program was initiated in 1986 and has grown considerably in size. It is now recognized as one of the most successful summer programs for undergraduates in the country. I would like to express my sincere gratitude to the National Science Foundation for their continued support since 1987 for this REU Site.

The purpose of the SUNFEST program is to provide bright, motivated undergraduate students with the opportunity to become involved in active research projects under the supervision of a faculty member and his graduate student(s). The general area of research concentrates on sensor technologies and includes projects such as materials and technology for sensors, nanotechnology and microstructures, smart imagers, sensors for biomedical applications and robotics. By providing the students with hands-on experience and integrating them with a larger research group where they can work together with other students, the program intends to guide them in their career choices. By exposing the students to the world of research, we hope they will be more inclined to go on for advanced degrees in science and engineering, as many have done.

The students participated in a variety of hands-on workshops in order to give them the tools to do first-rate research or enhance their communication skills. These included "Ethics in Science and Engineering", "Information Retrieval and Evaluation", "Applying to Graduate School", "Poster Presentations", and "Writing Technical Reports". Students also had plenty of opportunity for social interactions among themselves or with faculty and graduate student advisors.

As we did last year, group of judges selected the top project and two honorable mentions. The projects were selected based on the technical quality of the results, the quality of the poster and the slide presentation, and answering questions. The choices were very hard since all projects were excellent. The first prize went to Jacob Sacks for his project "A Wireless, Real-Time Embedded System for Closed-Loop Myoelectric Control of Sedated Primates," under the supervision of Professor Van der Spiegel, Dr. Milin Zhang and Xilin Liu. The two honorable mentions went to Jamie Johnson *for his project on "Playing with Transition Metal Dichalcogenides," with Professor A.T. Charlie Johnson; and to Marcus Pan for his project on "Signal Processing for Directional Speakers," under the supervision of Professor Daniel D. Lee.*

This booklet contains reports from this year's projects, the quality of which testifies to the high level of research and commitment by these students and their supervisors. I would like to express my sincere thanks to the students for their enthusiastic participation; the help of the faculty members, graduate students and support staff is very much appreciated. I would also like to thank Linda Kalb, Joshua Taton, Sid Deliwala, Jessica Leon, Douglas McGee, Lilian Wu, Susan Margulies and the ESE staff for their invaluable help in making this program run smoothly.

Jan Van der Spiegel, Director

FINAL REPORT

2014 SUMMER UNDERGRADUATE FELLOWSHIP
IN SENSOR TECHNOLOGIES
Sponsored by the National Science Foundation

http://www.seas.upenn.edu/sunfest/alumni-projects-14.php

TABLE OF CONTENTS

LIST OF STUDENT PARTICIPANTS IN THE SUNFEST PROGRAM SINCE 1986

Summer 2014

Justin Aird	Hampton College
Porscha Baines	Lincoln University
Antonio Basukoski	Columbia University
Jennifer Bourlier	University of Michigan at Dearborn
Jamie Johnson (Honorable Mention)	Broward College
Marcus Pan (Honorable Mention)	University of Pennsylvania
Golden Rockefeller	University of Delaware
Abel Rodriguez	The George Washington University
Jacob Sacks (Winner, Best Presentation & Poster Award)	The University of Texas at Austin
Jordan White	Hampton College

Summer 2013

George Chen (Winner, Best Presentation & Poster Award)	Johns Hopkins University
Cedric Destin	Temple University
Rodolfo Finocchi	Johns Hopkins University
Ty'Quish Keyes	Morehouse College
Andrew Knight	Norfolk State University
Samantha Muñoz	Vanderbilt University
Gedeon Nyengele (Honorable Mention)	Georgia Perimeter College
Quentin Morales-Perryman	Hampton University
Gabriela Romero (Honorable Mention)	Worcester Polytechnic Institute
Basheer Subei	University of Illinois at Chicago

Summer 2012

Larry Jason Allen	University of the District of Columbia
Karl Bayer	Columbia University
Thomas Belatti	Villanova University
Carlos Biaou (Winner, Best Presentation & Poster Award)	Prince George's County Community College
Matt Biggers	University of North Carolina
Stephanie Diaz	Birmingham University
Xavier Hanson-Lerma	University of Florida
Sezan Hessou	Penn State University
William Marshall (Honorable Mention)	Lehigh University
Blake McMillian	Hampton University
Ugonna Ohiri	University of Maryland
Anish Raghavan	Trinity College Dublin
Megan Schmidt (Honorable Mention)	University of Missouri

Summer 2011

Adeboye A. Adejare Jr.	University of the Sciences in Philadelphia
Jason Allen	University of the District of Columbia
Crystal Batts	Winston-Salem University
Matthew Hale	University of Pennsylvania
Syrena Huynh (Honorable Mention)	North Carolina State University
Monroe Kennedy	University of Maryland
Nyeemah Kennedy	Pennsylvania State University
Adam Lowery	Cornell University
Peter Malamas	John Hopkins University
Piyush Poddar (Honorable Mention)	John Hopkins University
Daniel J. Preston (Winner, Best Presentation Award)	The University of Alabama
James Resczenski	Virginia Polytechnic Institute and State University
Ziwei Zhong	Purdue University

Summer 2010

Jason C. Carter	Morgan State University
Carlos Torres Casiano	University of Puerto Rico, at Mayagüez
Nathalia Garcia Acosta (Honorable Mention)	Temple University
Brian Helfer (Winner, Best Project & Presentation Award)	University of Connecticut
Sarena Horava	University of Massachusetts Amherst
Brett Kuprel	University of Michigan
Logan Osgood-Jacobs (Honorable Mention)	Swarthmore College
Sriram Radkrishnan	University of Pennsylvania
Johary Rivera	University of Puerto Rico, Río Piedras Campus
Jennifer L. Smith	North Carolina State University
Noah Tovares	Occidental College

Summer 2009

Hank Bink	Lafayette College
Allison Connolly	Johns Hopkins University
Phillip Dupree	Columbia University
Katherine Gerasimowicz	University of Pennsylvania
Willie Gonzalez	Univ. of Puerto Rico, Mayaguez

Sarah Koehler	Cornell University
Linda McLaughlin	Community College of Philadelphia
Ieva Narkeviciute	Univ. of Massachusetts Amherst
Jeffrey Perreira	Lehigh University
Andrew Townley	University of Pennsylvania
Desiree Velazquez	Univ. of Puerto Rico at Humacao)
Valerie Walters	Virginia Polytechnic Institute and State University

Summer 2008

Clarence Agbi	Yale University
Uchenna Anyanwu	San Jose State University
Christopher Baldassano	Princeton University
Alta Berger	George Washington University
Ramon Luis Figueroa	University of Puerto Rico
David Joffe	Carnegie Mellon University
Erika Martinez	University of Puerto Rico
Alexei Matyushov	Arizona State University
Kamruzzaman Rony	Stony Brook University
Anil Venkatesh	University of Pennsylvania
Emily Wible	University of Pennsylvania

Summer 2007

Mulutsga Bereketab	Virginia Polytechnic Institute
Sonia A. Bhaskar	Princeton University
Patrick Duggan	Providence College
Nataliya Kilevskaya	University of Florida
Ryan Li	Case Western Reserve University
Viktor L. Orekhov	Tennessee Technological University
Andrew Potter	Brown University
Pamela Tsing	University of Pennsylvania
Victor Uriarte	Florida International University
Adriane Wotawa-Bergen	University at Buffalo
Arelys Rosado Gomez	University of Puerto Rico

Summer 2006

Sam Burden	University of Washington
Jose M. Castillo Colon	University of Puerto Rico
Alexsandra Fridshtand	Lehigh University
Shakera Guess	Lincoln University
Journee Isip	Columbia University
Nathan Lazarus	University of Pennsylvania
Armand O’Donnell	University of Pennsylvania

William Peeples	Lincoln University
Raúl Pérez Martínez	University of Puerto Rico
Helen Schwerdt	Johns Hopkins University
Xiaoning Yuan	Duke University

Summer 2005

Robert Callan	University of Pennsylvania
David Cohen	University of Pennsylvania
Louie Huang	University of Pennsylvania
Roman Geykhman	University of Pennsylvania
An Nguyen	University of Pennsylvania
Olga Paley	University of California at Berkeley
Miguel Perez Tolentino	University of Puerto Rico
Ebenge Usip	University of Southern California
Adam Wang	University of Texas, Austin
Kejia Wu	University of Pennsylvania

Summer 2004

Benjamin Bau	Massachusetts Institute of Technology
Alexander H.Chang	University of Pennsylvania
Seth Charlip-Blumlein	University of Pennsylvania
Ling Dong	University of Rochester
David Jamison	Johns Hopkins University
Dominique Low	University of Pennsylvania
Emmanuel U. Onyegam	University of Texas, Dallas
J. Miguel Ortigosa	Florida Atlantic University
William Rivera	University of Puerto Rico, Mayaguez
Matthew Sauceda	Texas A&M University, Kingsville
Olivia Tsai	Carnegie Mellon University

Summer 2003

Emily Blem	Swarthmore College
Brian Corwin	University of Pennsylvania
Vinayak Deshpande	University of Virginia
Nicole DiLello	Princeton University
Jennifer Geinzer	University of Pittsburgh
Jonathan Goulet	University of Pennsylvania
Mpitulo Kala-Lufulwabo	University of Pittsburgh
Emery Ku	Swarthmore College
Greg Kuperman	University of Pennsylvania
Linda Lamptey	University of Pennsylvania
Prasheel Lillaney	University of Pennsylvania
Enrique Rojas	University of Pennsylvania

Summer 2002

Christopher Bremer	Colorado School of Mines
Aslan Ettehadien	Morgan State University
April Harper	Hampton University
Catherine Lachance	University of Pennsylvania
Adrian Lau	University of Pennsylvania
Cynthia Moreno	University of Miami
Yao Hua Ooi	University of Pennsylvania
Amber Sallerson	University of Maryland/Baltimore
Jiong Shen	University of California-Berkeley
Kamela Watson	Cornell University
John Zelena	Wilkes University

Summer 2001

Gregory Barlow	North Carolina State University
Yale Chang	University of Pennsylvania
Luo Chen	University of Rochester
Karla Conn	University of Kentucky
Charisma Edwards	Clark Atlanta University
EunSik Kim	University of Pennsylvania
Mary Kutteruf	Bryn Mawr College
Vito Sabella	University of Pennsylvania
William Sacks	Williams College
Santiago Serrano	Drexel University
Kiran Thadani	University of Pennsylvania
Dorci Lee Torres	University of Puerto Rico

Summer 2000

Lauren Berryman	University of Pennsylvania
Salme DeAnna Burns	University of Pennsylvania
Frederick Diaz	University of Pennsylvania (AMPS)
Hector Dimas	University of Pennsylvania (AMPS)
Xiomara Feliciano	University of Turabo (Puerto Rico)
Jason Gillman	University of Pennsylvania
Tamara Knutsen	Harvard University
Heather Marandola	Swarthmore College
Charlotte Martinez	University of Pennsylvania
Julie Neiling	University of Evansville, Indiana
Shiva Portonova	University of Pennsylvania

Summer 1999

David Auerbach	Swarthmore College
Darnel Degand	University of Pennsylvania
Hector E. Dimas	University of Pennsylvania
Ian Gelfand	University of Pennsylvania
Jason Gillman	University of Pennsylvania
Jolymar Gonzalez	University of Puerto Rico
Kapil Kedia	University of Pennsylvania
Patrick Lu	Princeton University
Catherine Reynoso	Hampton University
Philip Schwartz	University of Pennsylvania

Summer 1998

Tarem Ozair Ahmed	Middlebury University
Jeffrey Berman	University of Pennsylvania
Alexis Diaz	Turabo University, Puerto Rico
Clara E. Dimas	University of Pennsylvania
David Friedman	University of Pennsylvania
Christin Lundgren	Bucknell University
Heather Anne Lynch	Villanova University
Sancho Pinto	University of Pennsylvania
Andrew Utada	Emory University
Edain (Eddie) Velazquez	University of Pennsylvania

Summer 1997

Francis Chew	University of Pennsylvania
Gavin Haentjens	University of Pennsylvania
Ali Hussain	University of Pennsylvania
Timothy Moulton	University of Pennsylvania
Joseph Murray	Oklahoma University
O'Neil Palmer	University of Pennsylvania
Kelum Pinnaduwage	University of Pennsylvania
John Rieffel	Swarthmore College
Juan Carlos Saez	University of Puerto Rico, Cayey

Summer 1996

Rachel Branson	Lincoln University
Corinne Bright	Swarthmore College
Alison Davis	Harvard University
Rachel Green	Lincoln University
George Koch	University of Pennsylvania
Sandro Molina	University of Puerto Rico-Cayey
Brian Tyrrell	University of Pennsylvania
Joshua Vatsky	University of Pennsylvania
Eric Ward	Lincoln University

Summer 1995

Maya Lynne Avent	Lincoln University
Tyson S. Clark	Utah State University
Ryan Peter Di Sabella	University of Pittsburgh
Osvaldo L. Figueroa	University of Puerto Rico-Humacao
Colleen P. Halfpenny	Georgetown University
Brandeis Marquette	Johns Hopkins
Andreas Olofsson	University of Pennsylvania
Benjamin A. Santos	University of Puerto Rico-Mayaguez
Kwame Ulmer	Lincoln University

Summer 1994

Alyssa Apsel	Swarthmore College
Everton Gibson	Temple University
Jennifer Healy-McKinney	Widener University
Peter Jacobs	Swarthmore College
Sang Yoon Lee	University of Pennsylvania
Paul Longo	University of Pennsylvania
Laura Sivitz	Bryn Mawr College
Zachary Walton	Harvard University

Summer 1993

Adam Cole	Swarthmore College
James Collins	University of Pennsylvania
Brandon Collings	Hamilton University
Alex Garcia	University of Puerto Rico
Todd Kerner	Haverford College
Naomi Takahashi	University of Pennsylvania
Christopher Rothey	University of Pennsylvania
Michael Thompson	University of Pennsylvania
Kara Ko	University of Pennsylvania
David Williams	Cornell University
Vassil Shtonov	University of Pennsylvania

Summer 1992

James Collins	University of Pennsylvania
Tabbetha Dobbins	Lincoln University
Robert G. Hathaway	University of Pennsylvania
Jason Kinner	University of Pennsylvania
Brenelly Lozada	University of Puerto Rico
P. Mark Montana	University of Pennsylvania
Dominic Napolitano	University of Pennsylvania
Marie Rocelie Santiago	Cayey University College

Summer 1991

Gwendolyn Baretto	Swarthmore College
Jaimie Castro	University of Puerto Rico
James Collins	University of Pennsylvania
Philip Chen	University of Pennsylvania
Sanath Fernando	University of Pennsylvania
Zaven Kalayjian	University of Pennsylvania
Patrick Montana	University of Pennsylvania
Mahesh Prakriya	Temple University
Sean Slepner	University of Pennsylvania
Min Xiao	University of Pennsylvania

Summer 1990

Angel Diaz	University of Puerto Rico
David Feenan	University of Pennsylvania
Jacques Ip Yam	University of Pennsylvania
Zaven Kalayjian	University of Pennsylvania
Jill Kawalec	University of Pennsylvania
Karl Kennedy	Geneva
Jinsoo Kim	University of Pennsylvania
Colleen McCloskey	Temple University
Faisal Mian	University of Pennsylvania
Elizabeth Penadés	University of Pennsylvania

Summer 1989

Peter Kinget	Katholiek University of Leuven
Chris Gerdes	University of Pennsylvania
Zuhair Khan	University of Pennsylvania
Reuven Meth	Temple University
Steven Powell	University of Pennsylvania
Aldo Salzberg	University of Puerto Rico
Ari M. Solow	University of Maryland
Arel Weisberg	University of Pennsylvania
Jane Xin	University of Pennsylvania

Summer 1988

Lixin Cao	University of Pennsylvania
Adnan Choudhury	University of Pennsylvania
D. Alicea-Rosario	University of Puerto Rico
Chris Donham	University of Pennsylvania
Angela Lee	University of Pennsylvania
Donald Smith	Geneva
Tracey Wolfsdorf	Northwestern University
Chai Wah Wu	Lehigh University
Lisa Jones	University of Pennsylvania

Summer 1987

Salman Ahsan	University of Pennsylvania
Joseph Dao	University of Pennsylvania
Frank DiMeo	University of Pennsylvania
Brian Fletcher	University of Pennsylvania
Marc Loinaz	University of Pennsylvania
Rudy Rivera	University of Puerto Rico
Wolfram Urbanek	University of Pennsylvania
Philip Avelino	University of Pennsylvania
Lisa Jones	University of Pennsylvania

Summer 1986

Lisa Yost	University of Pennsylvania
Greg Kreider	University of Pennsylvania
Mark Helsel	University of Pennsylvania

Amplification of Output Sound of Directional Ultrasonic Speakers for Bus Collision Warning System

NSF SUNFEST

Justin Aird (Electrical Engineering) – Virginia Polytechnic Institute and State University

Partner: Marcus Pan

Advisors: Dr. Daniel Lee, Alex Burka

Summer 2014

ABSTRACT

Parametric speakers utilize ultrasonic waves that have very sharp directivity. They transmit sound energy in a very straight path to a narrow area. Ultrasonic sound can affect the direction of sound. This effect is called "Directivity." Speakers with a high directivity can send a sound straight ahead in a narrower area. The goal of this project was to design ultrasonic parametric speakers that could be attached to a 12V battery of a bus, to be used as a pedestrian directional warning system to reduce bus-pedestrian incidents on street corners. We would design ultrasonic speakers so that it could play an input sound to alert the intended target. Making sure that if this warning system were to be played late at night it would not disturb others. We would build a power amplifier circuit for the ultrasonic speaker that it could draw as much power as possible from a 12V battery. We looked to see if the speaker was directional and loud enough to be heard at certain distances. After testing this project we plan to look into which other areas these ultrasonic speakers could be used, such as helping guide the blind, and to communicate with some animals since they use ultrasonic frequencies to communicate.

Introduction/Background

Over the past decade, bus collisions with pedestrians have been on the rise. The most likely cause of the increase of these incidents is that pedestrians of today seem to be more distracted and less aware of their surroundings [1]. SEPTA, the Southeastern Pennsylvania Transportation Authority, reports that most of these incidents occur on the street corners as buses are turning. Bus organizations all over the country have had issues with these accidents, frequently with injured pedestrians suing the organizations with which they have had an accident. It is estimated that such claims cost SEPTA over $40 million per year in compensation and legal fees [2]. The pedestrian loss of life and financial losses from increased collisions have made it critical to develop a system to prevent such accidents from occurring. This problem could be solved by a directional ultrasonic speaker array, which warns only the person in the direct path of the speaker [4]. This ultrasonic array is comprised of parametric speakers. There is an audible input in the human hearing range (20 Hz to 20 kHz), which is then amplified to an ultrasonic frequency [3]. Once that hits the air, since air is not linear, it will create an output sound matching the input in which any person in a direct path of the speaker can hear. The plan for this project is to adjust the hardware of the speakers to see how it affects the amplification of the output sound. First looking at the circuitry of the amplifiers seeing if there are any replacement parts that would allow more current to flow leading to more power generating a louder sound. Also, the application of a diaphragm which in most cases is a cone shaped material that vibrates

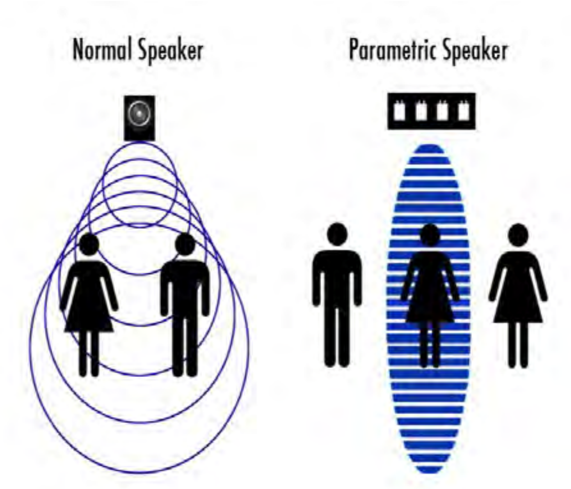

Figure 1: **Normal Speaks Verse Parametric Speakers**

and then helps to amplify the output sound of a speaker making the output louder. The diaphragm is a thin membrane layer, usually in a cone shape, but can be developed in various ways for specific applications depending on the speakers [5]. Sound is generated and is amplified by the diaphragm but its effects vary on the type of speaker. Different materials such as plywood, aluminum, brass, and polystyrene will be used to create several diaphragms to examine how those materials affect the output sound of the speaker. These will determine which materials are the easiest to use and are the most cost efficient [6]. This could be used to see if the addition of a diaphragm could help produce a more concentrated directional sound.

Background

There are three main sections of circuitry necessary for the output of the ultrasonic direction speaker array system from input to output. The filter chip, the PWM and inverter, and the BJT's and MOSFETS. These allow the input signal to come out as ultrasonic with the appropriate amplitude gain when setup correctly. Each of these sections is described below.

Filter Chip

The filter chip is an ADAU1701 used to sort out frequencies from an input signal. It is a single-chip audio system 28-/56-bit audio DSP, ADACs, DACs, and microcontroller-like control interfaces. Its processing can be used to make up for real-world limits of speakers and amplifiers showing improved audio quality perception [7]. Programs can be loaded onto it at power-up from serial EEPROM with an external microcontroller, or on power-down. Two ADCs and Four DACs allow a 98.5 dB analog input to analog output dynamics. Also having digital input and output ports allowing glueless connection, and this chip communicates through an ��^{2}C bus or a 4-wire SPI Port

[7].

Figure 2: **ADAU1701 chip**

PWM & Inverter

The Pulse-Width-Modulation Control Circuit (PWM) is a single chip designed for power-supply control. It contains two error amplifiers, and an on chip adjustable oscillator [8]. This is what is used to adjust the frequency of the output signal using potentiometers as

Figure 3: **PWM**

well as fix the width of the duty cycle of the pulse.

The inverter chip is a CD74HC4904 which has input protection that allows it to be used as logic level

Figure 4:

Inverter Chip

translators that convert high-level log to low level-logic, all while being operated on a low-level logic supply [9]. This is used to provide part of the total gain of the amplitude in the circuit.

BJTs & MOSFETs

The Bipolar Junction Transistors (BJT) used for this circuit are NPN 2N2222 and PNP 2N2907. With the NPN made for small signal and general purpose switching applications [10]. While the PNP device being designed as a general-purpose amplifier [11].

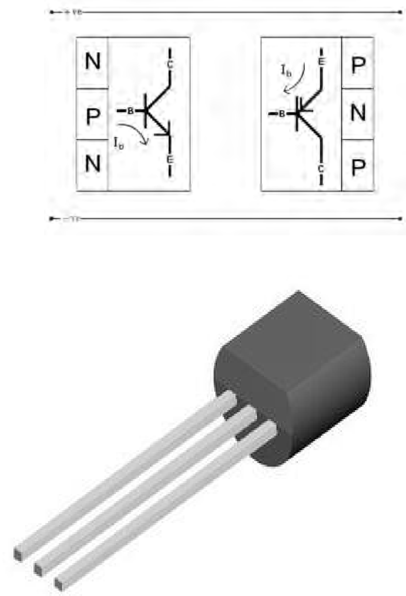

Figure 5: **BJT Model**

MOSFET is a metal-oxide-semiconductor field-effect transistor. The MOSFETs used are the

FDS8984 and FDS4935. This 8984 is an "N-Channel MOSFET has been designed specifically to improve the overall efficiency of DC/DC converters using either synchronous or conventional switching PWM controllers. It has been optimized for low gate charge, low rDS(ON) and fast switching speed"[12]. While the 4935 is a "P-Channel MOSFET is a rugged gate version of

Semiconductor's advanced PowerTrench process. It has been optimized for power management applications requiring a wide range of gave drive voltage ratings (4.5V – 20V)” [13].

Figure 5: **BJT Model**

The BJTs and MOSFETs when used correctly, will output the majority of the amplitude gain in the circuit, allowing maximum power output for the ultrasonic speaker array.

Safety

For electrical safety refer to OSHA electrical safety rules and regulations [14]. As for ultrasonic sound safety, there is little information on it, but there has been some research done. Ultrasonic safety should be treated as normal sound safety. Even though it cannot be heard, ultrasonic decibel levels of 115 and up can cause damage to hearing leading to tinnitus (ringing in the ears) and loss of hearing. Also, there have been studies showing “the eye can serve as an acoustic window to the ear via the intracranial soft tissues. The frequency response is in the low ultrasonic range, and this type of hearing is termed *eye conduction*. Auditory and vestibular coding is postulated.”[15]. Meaning that ultrasonic waves can be absorbed through the eyes leading to conditions that could possibly harm the brain in addition to hearing. Make sure to wear ear protection, such as ear plugs and/or ear muffs, as well as keeping eyes at a safe distance, and not directly in front of any speaker array that produces ultrasonic waves.

Experimental Procedures

The ultrasonic speaker array was based off of the Soundlazer Parametric speaker with some modifications for the intended research concerning bus an pedestrian street corner coll off with the designed power amplifier on the bread board which was then converted into a Proto Board. After which would be used to conduct a few test concerning the directivity of the new speaker array as well as the decibel readings at different distances compared to not only the Soundlazer but also a normal speaker.

Figure 6: **MOSFET Chip**

Building Breadboard

The breadboard was made up of the PWM, inverter, BJTs and MOSFETS. First off, the power supplies and grounds need to be established knowing that the circuit needs both a 6V and 12V power supply. Once those have been established using the data sheet, it is possible to place the PWM TL494 chip so that the correct input and output pins can be established [8]. It also has the resistors and potentiometers, which allow users to fine-tune the output frequency to 40 KHz. This is then hooked-up to the CD74HC inverter chip, which just has wires attached to the appropriate pins, has a 6V power supply [9]. This has input from the output of the PWM, and then outputs the BJTs. The inverter is hooked-up directly to the bases of the NPN and PNP so that the frequency outputted can go through the correct collectors and emitters also powered by 6V [10], [11]. This is then hooked-up to the input of the MOSFET FDS 8984 and FDS4935A through a set of diodes, capacitors, and resistors hooked up to 6 and 12 volts which then outputs the final frequency. After construction is completed, look over circuit to insure that no obvious short circuits are present, and then hook it up to two power generators, an oscilloscope, and a frequency generator. Using the frequency generator to input a continuous 1K Hz sine wave, and the power supplies to hook up the 12V and 6V connections. Use the oscilloscope set to measure frequency

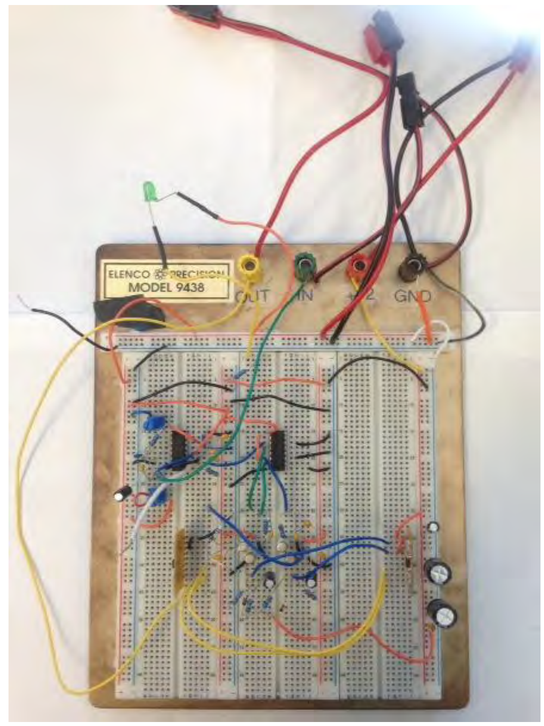

Figure 7:

Bread Power Amplifier Circuit

and peak to peak amplitude to test and make sure the input signal frequency matches that of the frequency generator. Then test the output frequency after the PWM chip. If that output is not 40K Hz, using a small flat head screwdriver, set the potentiometers until the oscilloscope shows that the output frequency after the PWM is 40K Hz. After that check the output frequency and peak to peak amplitude of the final output which comes out of PIN 8 of the MOSFET FDS 8984 [12]. Make sure that the oscilloscope says that the output is 40K Hz and the peak to peak amplitude is 30-40V showing that there is a gain in the power amplifier setup. If this is not the case (the output is not giving those values), go back and test the output at the PWM chip, the inverter chip, and after the BJT's, to figure out where the issue is.

Proto Board

The proto board is the same setup as the breadboard with PWM, inverter, BJTs, and MOSFETs. All the connectors are soldered on instead of having already existing connections like in the breadboard. The pros to the proto board are that it is smaller and easier to transport for experiments. The cons are that it takes longer to complete because any mistakes can lead to completely starting over since each piece has to be soldered into place with the right connections. This also needs to have the 6 and 12 volt connections for a power supply. The setup is the same as the breadboard however, it can be setup in the fashion which is easiest for the person making it. It will be built the same as the breadboard with the PWM chip having the input go in through that. However, at this time, it is recommend to test the input and output using the oscilloscope and frequency generator after each chip is soldered into place instead of when the whole thing is completed. That is to insure there are no mistakes. Then comes the inverter chip like before, and once that is hooked up to the PWM, take it back to the oscilloscope to make sure it is outputting correctly. Next comes the BJT and MOSFET setup with the correct power supplies, resistors, diodes, and capacitors and once that is done and hooked up to the inverter and PWM the circuit is complete. Run final test using the oscilloscope at the test points after the

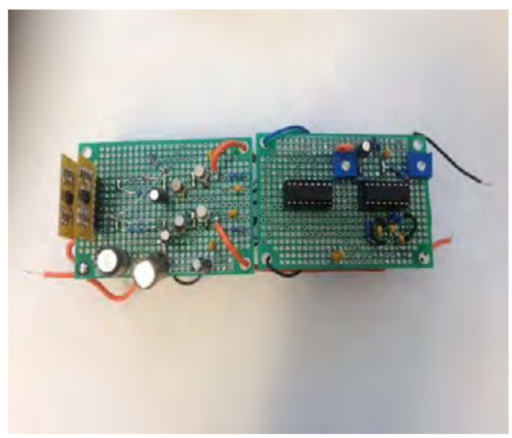

Figure 8:

Proto Board Power Amplifier Circuit

PWM, inverter, BJTs and MOSFETs to insure that the proto board is working correctly.

Classroom Directivity Test

An empty classroom was used to experiment the directivity of the speaker array that was created compared to the Soundlazer model it was based off, of as well as normal speakers. The test was done in an open space in a classroom measuring out the decibel levels at one meter increments up to six meters at 0°, 15°, and 30°. Then using vertical and horizontal displacement to record the distances at each angle. This setup was used to see just how loud each speaker is in the same setting as well as test how directed the sound if for each speaker.

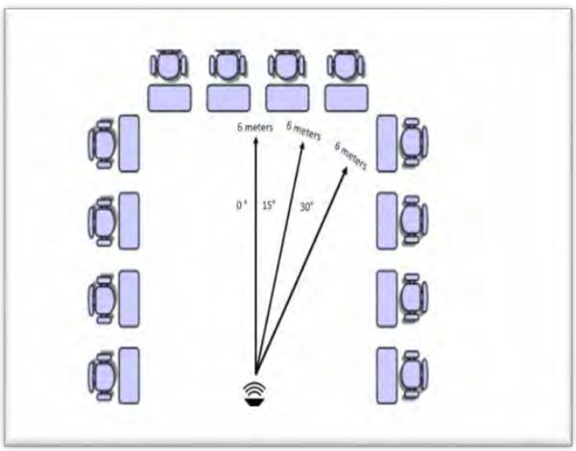

Distance Test

After the directivity, the next step was to take the ultrasonic speaker array outside, to see how far a microphone could record the sound produced from the array, and compare it to the Soundlazer model, as well as normal speakers. This would entail going outside using the speakers hooked to a 12V battery and using the microphone to record sound at whole meter increments between one meter and 25 meters. This would require using measuring tape to measure out the meter increments and tape to label them. As well as a microphone hooked up to a laptop which would use Audacity a sound recording program to record the sound produced at each distance.

Results & Discussion

Table 10.

Normal Speakers Directivity Test Displacement and Sound Levels

Normal Speakers		
Horizontal Displacemnt (m)	Vertical Dispalcement (m)	Decibals(dB)
0	1	82.6
0	2	78.55
0	3	77.3
0	4	76.55
0	5	75.35
0	6	72.3
0.026	0.97	83.65
0.52	1.91	77.7
0.78	2.9	76.2
1.04	3.86	75.85
1.29	4.83	74.55
1.55	5.8	73.2
0.5	0.87	82
1	1.73	77.2
1.5	2.6	76.1
2	3.46	75.5
2.5	4.33	75.5
3	5.2	72.5

Table 11. **Soundlazer**

Directivity Test

Displacement and Sound

Soundlazer		
Horizontal Displacemnt (m)	Vertical Dispalcement (m)	Decibals(dB)
0	1	109.35
0	2	86.75
0	3	85
0	4	80.75
0	5	77
0	6	75.2
0.026	0.97	68.4
0.52	1.91	65.35
0.78	2.9	62.45
1.04	3.86	61.4
1.29	4.83	62.4
1.55	5.8	59.65
0.5	0.87	73.15
1	1.73	69.3
1.5	2.6	64.95
2	3.46	62.85
2.5	4.33	60.45
3	5.2	58.75

Table 12.

198 Speaker Ultrasonic Array

Displacement and Sound

198 Speaker Ultrasonic Array		
Horizontal Displacemnt (m)	Vertical Dispalcement (m)	Decibals(dB)
0	1	110.25
0	2	86.3
0	3	82.15
0	4	77.2
0	5	73.75
0	6	69.8
0.026	0.97	71.9
0.52	1.91	59.9
0.78	2.9	64.2
1.04	3.86	51.4
1.29	4.83	54.15
1.55	5.8	58
0.5	0.87	73.45
1	1.73	61.3
1.5	2.6	66.3
2	3.46	50.8
2.5	4.33	54.75
3	5.2	57.9

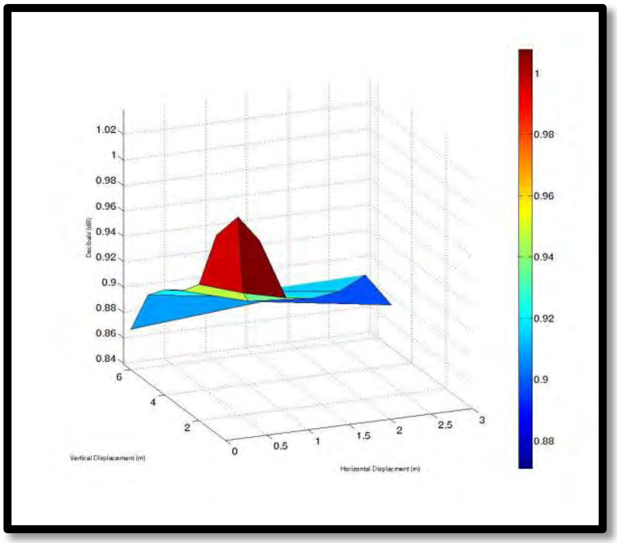

Figure 13.

Normal Speakers 3-D

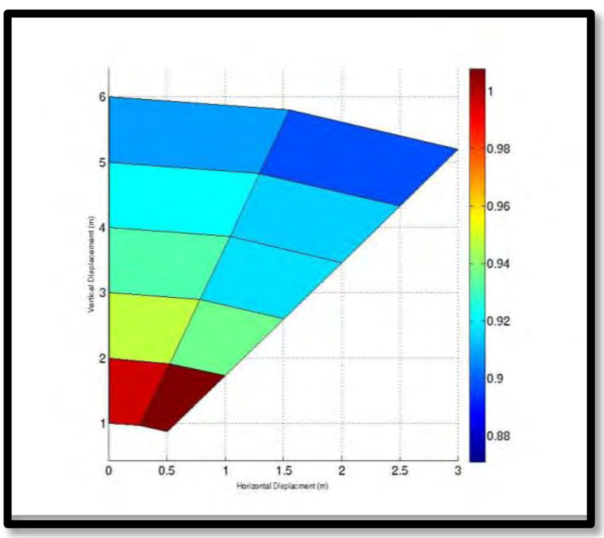

Figure 14.

Normal Speakers Top View

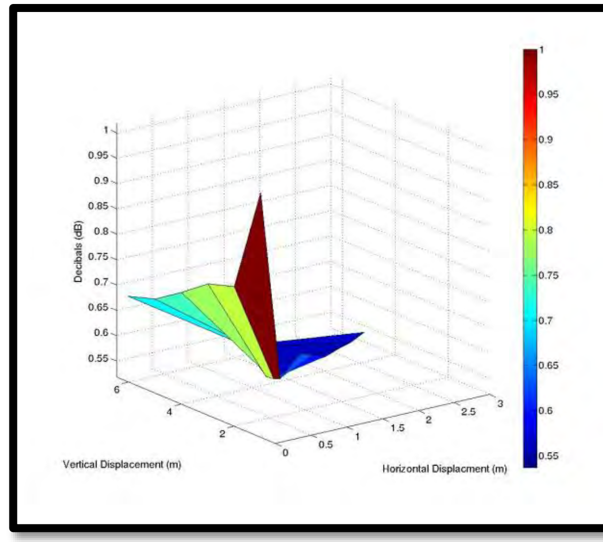

Figure 15.

Soundlazer 3-D

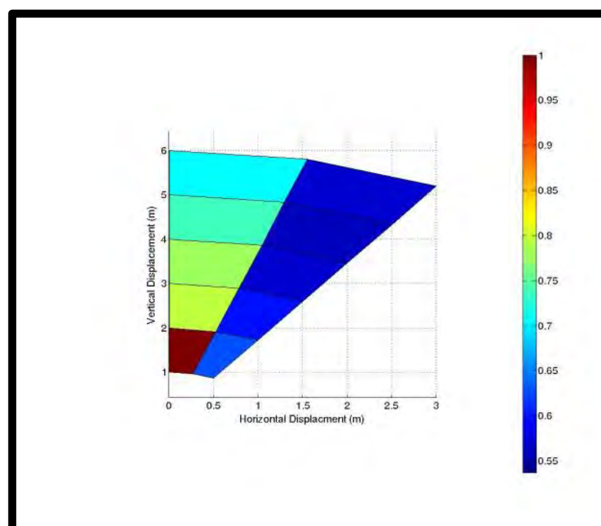

Figure 16. **Soundlazer Top View**

Normalized graphs from class room test showing max dB level as one so that all graphs are scaled equally, refer to data above in previous section to note specific dB levels at each displacement.

The data collected for this test was a recording from a microphone and below is an example of what the data looks like and the fully analysis can be done after the spectrogram.

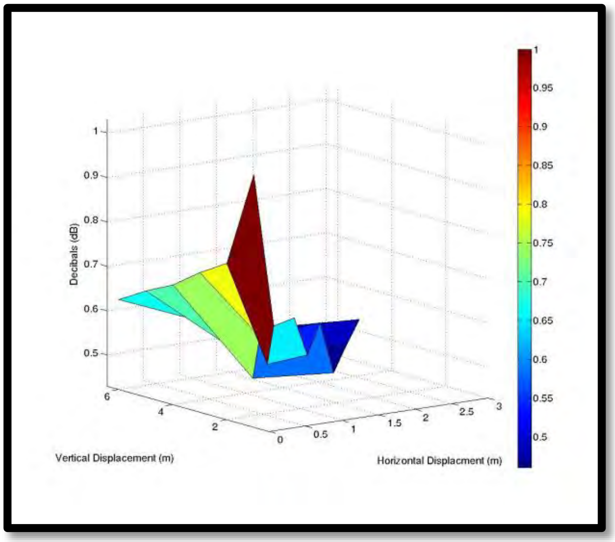

Figure 17.

198 Speaker Array 3-D

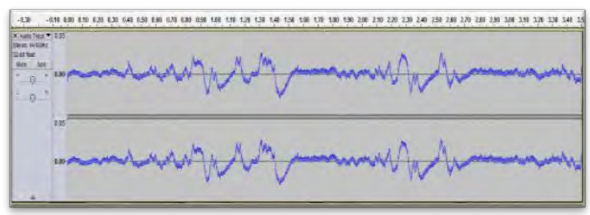

Figure 19.

Microphone recording Audacity

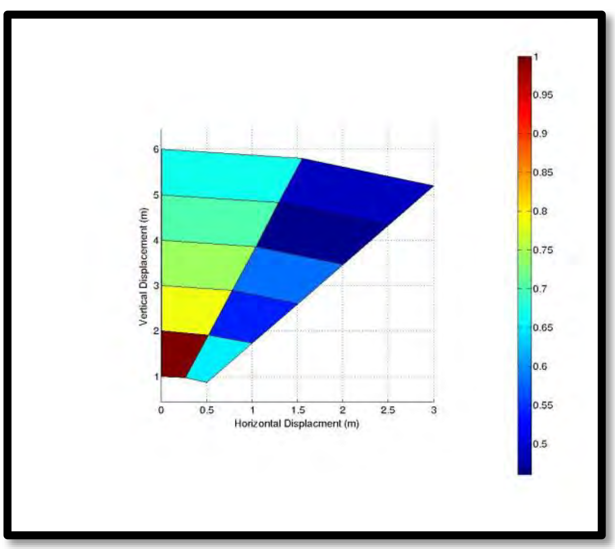

Figure 18.

198 Speaker Array Top View

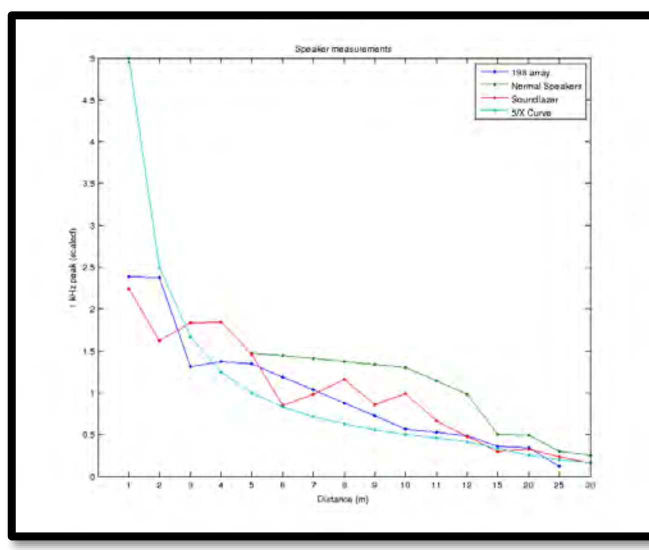

Figure 20.

Plot of 1K Hz frequency Peaks from Spectrogram

Observations:

First, before the discussion of data there were notable observations that were recorded, and could be useful in future studies involving this line of ultrasonic research. The most important observation in regards to safety, is that even when there was no input source, the sound meter was still able to pick up dB readings from the ultrasonic speaker array. This means that it can be concluded that even though there is no sound waves in the audible range being played there are still ultrasonic frequencies coming out when the speakers were powered. Showing that even though there was no input source it is dangerous to put a person's ears or eyes in direct contact of the speaker less than a one meter away when it is being powered. There are not many studies showing the dangers of ultrasonic waves. However, with the speakers having dB readings of up to 130dBs, at less than a meter away, this could damage a person's hearing.

Another notable observation was the pilot test which we ran before doing the speaker distance test. By taking out the Soundlazer to a busy street corner and having one lab member hold the speaker while the other stood across the street with a sound meter to see if it could be heard with traffic passing by. It was noted that the Soundlazer could be heard by the person listening, however the sound meter could not pick up the sounds produced by the Soundlazer only recording the readings of the sound of traffic in the area.

While running the experimenter to pick up speaker frequency at different distances outdoors, it was noted that there was a squirrel that, whenever the ultrasonic speaker array was being played, would stop digging for food and turn towards the speaker sound. It would continuously look at the speaker when it was powered on and then stop when it was powered off. This lead to some research on whether or not squirrels could hear ultrasonic frequencies, and the lab learning that squirrels can indeed hear up to 50K Hz showing that ultrasonic speakers could be useful towards animal communication.

Discussion:

After collecting data, it was analyzed. The directivity test first showed that the normal speakers have similar dB levels in all directions, given their displacement (Table 10). This was then plotted showing how the dB levels look in the room in three dimensions giving the horizontal displacement, vertical displacement, and dB levels normalized to compare to other speakers refer to (Figs. 13 and 14). The Soundlazer shows that at zero horizontal displacement the dB levels were the highest and then dies off on the sides where there is horizontal displacement refer to (Table 11). The normalized plot of the Soundlazer shows a beam of high dB levels at zero degrees and then quieter sound at fifteen and thirty degrees refer to (Figs. 15 and 16). 198 array was similar to the Soundlazer having the zero displacement have the largest dB levels while the sides were much lower. However from the raw data and plotted data the 198 array was louder than the Soundlazer showing that it draws more power refer to (Table 12 and Figs. 17-18).

The second test was the distance test done outside showing how the different speakers compared to each other in an outside setting. Testing the beam of sound produced by each in one direction. The data was recorded using a microphone and the program audacity refer to (Fig. 19). This was then taken into MATLAB, which analyzed all the sound files produced, and then plotted the peaks of the 1K Hz input that was placed into each speaker. The graph showed that the Soundlazer and the 198 array both follow and inverse x fit. The normal speaker did not follow that fit. That could be due to the face that indoor speakers were used and do not function properly outdoors, because they use walls to amplify their sound, and there were no walls present for the experiment (Fig. 20).

Conclusion

In conclusion, we were able to design a replica of the Soundlazer with modifications to the power amplifier circuit. After finishing up all experiments it could be concluded that the larger speaker array was able to draw more current leading to a more powerful speaker producing a louder directional sound. This speaker array can easily be hooked-up to a 12V battery which is the same source produced from the busses. The speaker is in fact directional and is loud enough to be heard in busy intersection up to 25 meters away.

Future Work

The future goals for this project, now that the speaker array is correctly working, are to get onto the bus, making it easy to hook up, and then test how efficiently it works in a street corner situation. Also, we can look into other future applications for direction speakers. When looking back onto the observations, we see that directional ultrasonic speakers could be useful for communication tagging of animals that can hear ultrasonic frequencies, as well as giving the blind a warning system that could alert them of upcoming obstacles, helping to better guide them around more difficult areas to navigate.

Acknowledgments

We would like to acknowledge the University of Pennsylvania for allowing us to use their facilities to conduct our experiments. As well as the SUNFEST program and NSF for helping this research be done.

References:

[1] de Jong, D. Distraction And Pedestrian Safety: How Talking On The Phone, Texting, And Listening To Music Impact Crossing The Street (2012). *Accident Analysis & Prevention*: n. pag. *Science Direct.* (Retrieved June 26, 2014). Web.

[2] SEPTA Accidents. (n.d.). (Retrieved June 2, 2014), from http://www.jaffehough.com/practice-areas/septa-accidents/

[3] Miura K. Ultrasonic Directive Speaker (2011). Elecktor. (Retrieved June 2, 2014). Web.

[4] Pompei J. Sound From Ultrasound: The Parametric Array as an Audible Sound Source (2002). MIT. (Retrieved June 2, 2014).

[5] History and Types of Loudspeakers (2011). Edison Tech Center. (Retrieved June 12, 2014). Web.

[6] Okuyama, M. Development of a capacitive ultrasonic sensor having parylene diaphragm and characterization of receiving performance of arrayed device (2008). *Sensors and Actuators A: Physical*: 94-102. *Science Direct*. (Retrieved June 26, 2014). Web.

[7] Analog Devices, “SigmaDSP 28-/56-Bit Audio Processor with Two ADCs and Four DACs,” ADAU701 datasheet, Last Updated Mar. 2013.

[8] Texas Instruments, “Pulse-Width-Modulation Control Circuits,” TL494 datasheet, Jan. 1983, Revised Jan. 2014.

[9] Texas Instruments, “High-Speed CMOS Logic Hex Buffers, Inverting and Non-Inverting,” CD74HC4049 datasheet, Feb. 1998, Revised Feb. 2005.

[10] Central, “Silicon NPN Transistors,” NPN 2N2222 datasheet, July 2013.

[11] FAIRCHILD, “PNP General-Purpose Transistor,” PNP 2N2907 datasheet, Jan. 2014.

[12] FAIRCHILD, “N-Channel PowerTrench MOSFET,” FDS8984 datasheet, Feb. 2010.

[13] FAIRCHILD, “Dal 30V P-channel PowerTrench MOSFET,” FDS4935A datasheet, March 2002.

[14] Occupational Safety & Health Administration, *OSHA Electrical Safety.* Washington D.C.: U.S. Department of Labor, n.d.

[15] Lenhardt ML. Eyes as Fenestrations to the Ears: A Novel Mechanism for High-Frequency and Ultrasonic Hearing. Int Tinnitus J. 2007;13(1):3-10

[16] KOBITONE, “Ultrasonic Transducers,” 255-400ST12M-ROX, 255-400SR12M-ROX datasheet, Nov. 2012

Electrospinning Polymer Polyvinylidene Fluoride, Based Piezoelectric Transducer For The Hearing Impaired

Porscha Baines (Lincoln University- Biology), *SUNFEST Fellow*

Dr. Jorge Santiago, Engineering

Abstract— **This paper describes the efforts undertaken in the development of a polymer based piezoelectric transducer. Through the process of electrospinning Polyvinylidene fluoride, the fibers are to act as the hair cells present in the ear. Electrospinning is a method where the electrical force of a liquid solution overcomes the surface tension to produce very fine fibers. It has been theorized that a piezoelectric transducer may be a proper substitution for the hair cell, resulting in hearing improvements. Currently, cochlear implants are effective in the treatment of severe hearing loss. The cochlear implant of today is made up of microphones, electrodes, a transmitter, magnets, and microcomputers in which some components are external to the human body. Through previous studies, device requirements were found to have small dimensions, flexibility, high sensitivity, impedance matching, and biocompatibility. The proposed piezoelectric polymer will meet these requirements and will require no external circuitry. The idea of the new device is to mask the fact that there is an implant surgically installed. The project was tackled during a mere ten week period, so there are more tests that can be carried out. Further study is to be done by testing the fibers using the SEM and FTIR to verify if the fibers meet the device requirements.**

I. Introduction

Scientists today are working towards designing an improved cochlear implant that will mask the fact that there is a device surgically installed into the patient's inner ear. Sensorineural hearing loss occurs when there is damage to the cochlea or inner ear. The major cause of this particular hearing impairment is abnormalities in the hair cell including poor hair cell function [5]. An individual's hair cells may be categorized as being congenital or acquired hearing loss.

According to Brian Kandell, it has been theorized that a piezoelectric transducer may be a proper substitution for the hair cell, resulting in hearing improvements [9]. Some complications with the ones that exists are that the cochlear implant requires patients to have an inch long, disk shaped transmitter attached to their skull [1]. Instead of a microchip implant, the signal from the piezoelectric sensor would travel and transmit an electrical signal and pass it to an electrode in the cochlear.

Researchers at Microsystems technology Laboratory (MTL), along with physicians at Harvard Medical School and the Massachusetts Eye and Ear Infirmary (MEEI) have developed a low power signal-processing piezoelectric transducer with the idea to create a cochlear implant device with no exterior hardware [1]. The implant would be wirelessly charged with a battery life of eight hours.

This paper presents general information regarding cochlear implant designs, difficulties, progress to date, and the process of electrospinning. The research project is intended to produce polymer Polyvinylidene fluoride (PVDF) fibers for cochlear implantation. Sect. 2 provides background of the human ear, sensorineural hearing loss, cochlear implants, piezoelectricity, and electrospinning in order to contextualize this particular project. Sect. 3 will give the materials and instrumentation used throughout this project and the methodology behind their uses. Sect. 4 will provide the results gained from various tests. Sect. 5 will conclude this paper and project.

II. Background

1.1 The Human ear

The human ear serves as a transducer that detects and interprets sound. The ear consists of three parts – the outer ear, the middle ear, and the inner ear. Each part serves a different purpose. An illustration of the ear is shown in figure 1.1.1 of the ear.

1.1.2 The Outer Ear

The outer ear is the external portion of the ear which serves to collect and transfer sound to the middle ear [2]. The first link in conduction to sound also provides protection in order to prevent damage to the eardrum.

1.1.3 The Middle Ear

The middle ear serves to transform the energy of sound wave into internal vibrations to the cochlea of the inner air [2]. The middle ear has five major parts: The cavity and mastoid air spaces; the tympanic membrane (eardrum); the auditory ossicles (bones), malleus, incus and stapes; the middle ear muscles; and, the Eustachian tube [3].

1.1.4 The Inner Ear

The inner ear serves to transform energy of a compressional wave into the nerve impulses that are transmitted to the brain [2]. The inner ear consists of a cochlea, the semicircular canals, and the auditory nerve. Each division has a specialized sensory apparatus and a separate function. The cochlea detects the different pressure changes caused by high pitched and low pitched sounds. High pitched sounds are detected at the base of the cochlea, while lower pitched sounds are detected at the end of the cochlea's spiral [4]. The inner surface of the cochlea is lined with over 20,000 hair-like nerve cells that release an electrical impulse that passes along the auditory nerve towards the brain [2]. The cochlea and semicircular canals are filled with fluid. The fluid and nerve cells of the semicircular canal are not used for hearing but serve to detect movement and help maintain balance [2]. The semicircular canals are lined with cilia and fluid called endolympth. When there is movement of the head, the endolymph moves the cilia which communicates to the brain. As a result balance is kept. The auditory nerve takes electrical impulses from both the cochlea and semicircular canals and makes connections with the auditory areas of the brain [4].

Figure.1.The Ear

1.2 Sensorineual Hearing Loss

Among the different kinds of hearing disorders, sensorineural hearing loss occurs when there is damage to the cochlea or inner ear. The causes can be categorized into either congenital or acquired hearing loss. Congenital hearing loss is present at birth, and can be either inherited or caused by abnormal development in the fetal stages [6]. Acquired hearing loss occurs after birth, during any time of the patient's life. The major cause of this particular hearing impairment is abnormalities in the hair cell including poor hair cell function [5]. An individual's hair cells may be abnormal at birth, or damage can be caused by exposure to loud noises, such as loud music in ear buds for a prolonged period, or being exposed to loud volumes without proper ear protection. In patients, normal amplification with hearing aids or middle ear reconstructive surgery cannot enhance hearing potential, and sensorinueral hearing loss can be permanent [3].

1.3 Cochlear Implants

A cochlear implant is a small electronic device, which stimulates nerve fibers in the cochlea by electrical charge [7]. Currently, cochlear implants are effective in sensorineural hearing loss. The device consists of a microphone, a speech processor, a transmitter, and an electrode ray. The microphone picks up sounds from the environment, while the speech processor selects sounds to send to the transmitter. The transmitter then converts the signals from the speech processor into electric impulses. An electrode ray collects the impulses from the transmitter and sends them to regions of the auditory nerve [7]. The auditory nerve is what carries the charges to the brain. The problem that exists is the idea that in order to surgically plant this device, doctors will have to first go through various tissues and anatomy of the ear. Additionally, other issues governing the cochlear implants regard replacing any external equipment that can become damaged, for example, batteries [5].

1.4 Piezoelectricity

In the late nineteenth century it was observed that certain materials generate an electric charge when under pressure. In 1881, Hermann Hankel suggested using the term piezoelectricity, which is derived from the Greek word "piezen" or "piezo" meaning to press [8]. Piezoelectricity is electrical energy produced in response to applied mechanical stress. Once pressure is applied to the object, a negative charge is produced on the expanded side and a positive charge on the compressed side [9]. After the pressure is relieved, electrical current flows across the material.

1.5 Electrospinning

Electrospinning is a method whereas the electrical force of a liquid solution overcomes the surface tension to produce very fine fibers. [10] This technique uses electrostatic forces to produce fibers from polymer solutions, thus the fibers produced have a thinner diameter. Electrospinning is performed at room temperature, with major components involved. When high voltage is applied to the liquid, the liquid becomes charged and drips out of the Taylor cone. It extends in a straight line for a while and then it begins to spiral out in various directions. The solvent will then evaporate resulting long fibers onto a ground metal sheet.

III. Experimental Results

The experimental setup is pictured below. The positive terminal is in the needle of the syringe by the power supply for electrospinning and the metal collector. After the platform is moving and the metal collector is rotating, the distance from the tip of the needle to the collector is measured 10cm apart. The power supply for electrospinning is turned on using 10kV while maintaining a 1cm to 1kV ratio. Furthermore the pump is turned on and was set at 1mL with a volume of 0.7mL/h as the ratio. The fibers are collected using two methods. The first method was cutting the fibers using a razor, and the second method required putting a piece of silicon on top of the metal collector so the fibers will land on the silicon.

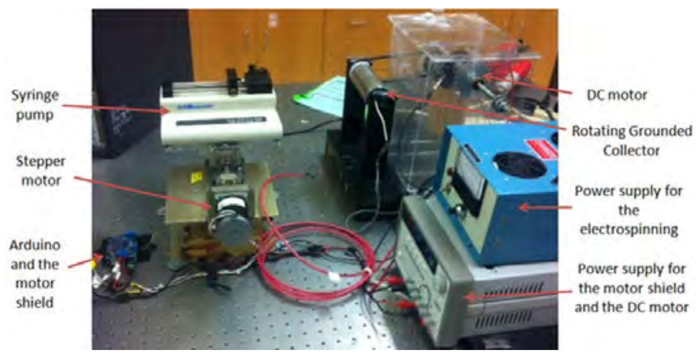

Figure. 2. Experimental Setup for the Electrospinning.

2.1.3 Solutions

Two types of solutions were created, one contains PVDF and DMF and the other contains PVDF and 3:1 ratio of DMF to Acetone at different weight percents (wt%) for each. The solutions were kept on a hot plate between 50°C and 75°C with a magnetic stirrer overnight. The charts below

Creating our solutions

	Polyvinylidene fluoride (PVDF)	Dimethylformamide (DMF)	Viscosity
24 wt%	3.02g	10mL	2.39 Pa·s
26 wt%	3.32g	10mL	16.52 Pa·s
30 wt%	4.01g	10mL	8.90 Pa·s

Caveat: Viscosity measurements did not result as expected

	Polyvinylidene fluoride (PVDF)	3:1 Dimethylformamide (DMF) + Acetone		Viscosity
		DMF	Acetone	
18 wt%	1.99g	7.5mL	2.5mL	0.15 Pa·s
20 wt%	2.33g	7.5mL	2.5mL	4.54 Pa·s
22 wt%	2.55g	7.5mL	2.5mL	10.90 Pa·s
25 wt%	3.02g	7.5mL	2.5mL	20.58 Pa·s

3.1 Viscosity of the solutions
The rheometer is the instrument measure used to measure viscosity of the solutions. The rheometer uses Newton's law of viscosity going at different rates or velocity.
CAVEAT: Viscosity measurements did not result as expected

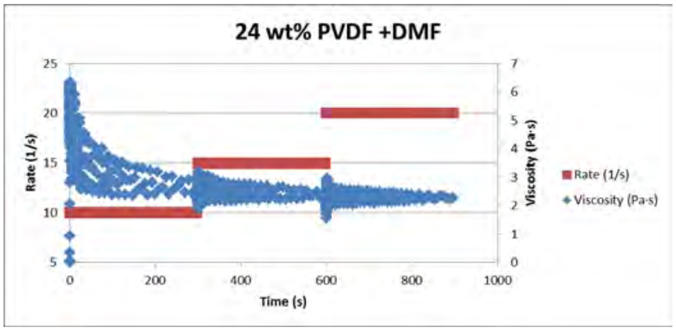

Figure.4. Graph created by the measurement by the rheometer

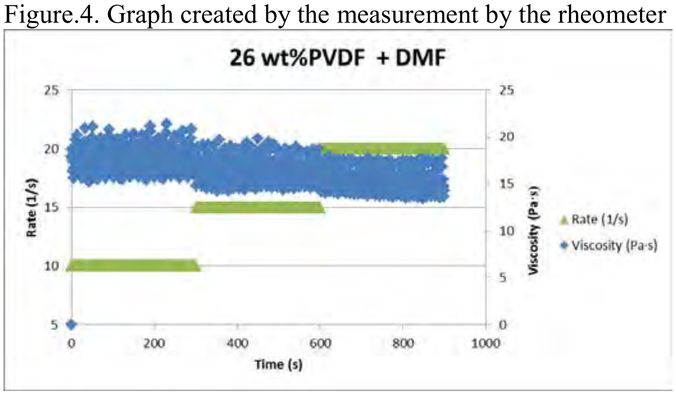

Figure.5. Graph created by the measurement by the rheometer

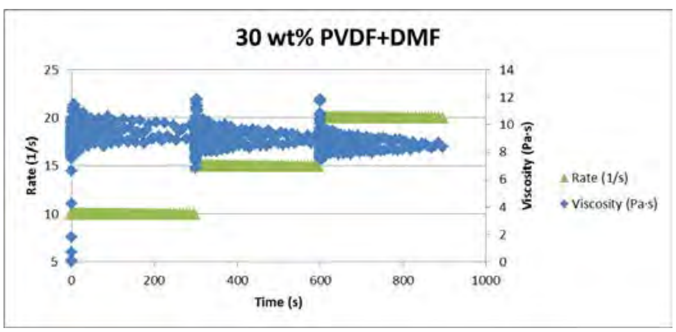

Figure.6. Graph created by the measurement by the rheometer

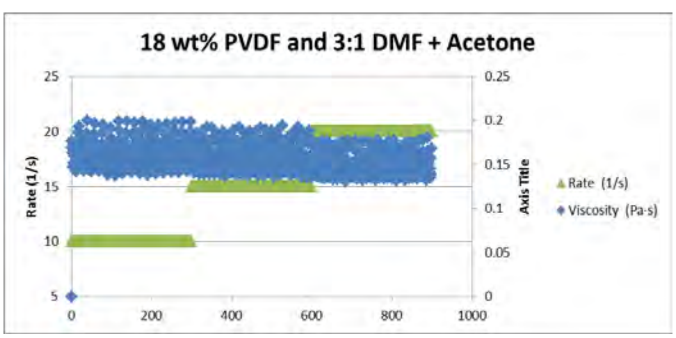

Figure.7. Graph created by the measurement by the rheometer

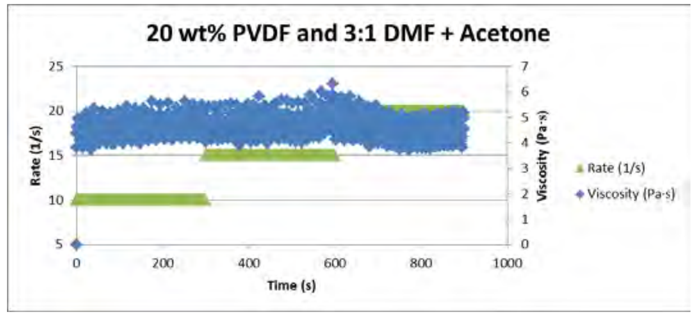

Figure.8. Graph created by the measurement by the rheometer

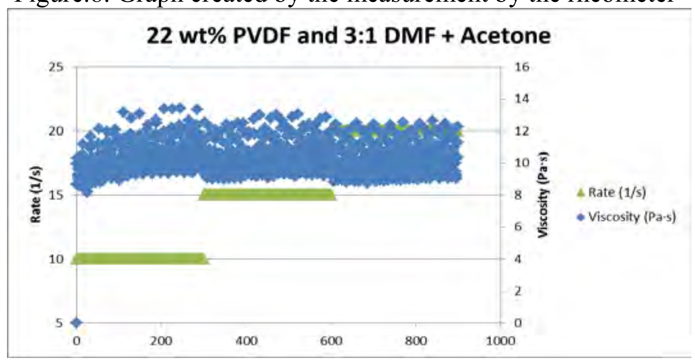

Figure.9. Graph created by the measurement by the rheometer

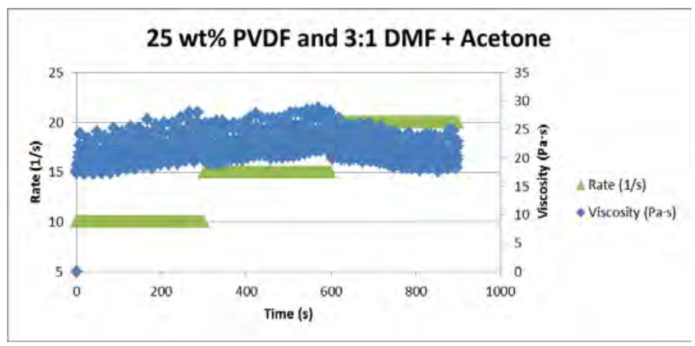

Figure.10. Graph created by the measurement by the rheometer

Table 1. Show the viscosities of each of the solutions created depending on their wt%.

PVDF + DMF	Viscosity
24 wt%	2.39 Pa•s
26 wt%	16.52 Pa•s
30 wt%	8.90 Pa•s

Table 2. Show the viscosities of each of the solutions created depending on their wt%.

PVDF + 3:1 DMF, Acetone	Viscosity
18 wt%	0.15 Pa•s
20 wt%	4.54 Pa•s
22 wt%	10.90 Pa•s
25 wt%	20.58 Pa•s

IV. Discussion and Conclusion

3.2 Fibers

The size dimensions of the nanofibers are to range from 100nm to 250nm. The size of the fibers produced from the solution which fibers were thinnest contained PVDF with DMF between 24.1 wt% to 26 wt%. In 24.1 wt% it is shown that some of the fibers were very thin but also produced some droplets. At 26 wt% there were no droplets, but the fibers were a little too thick. Solution 29.8 wt% produced very thick fibers.

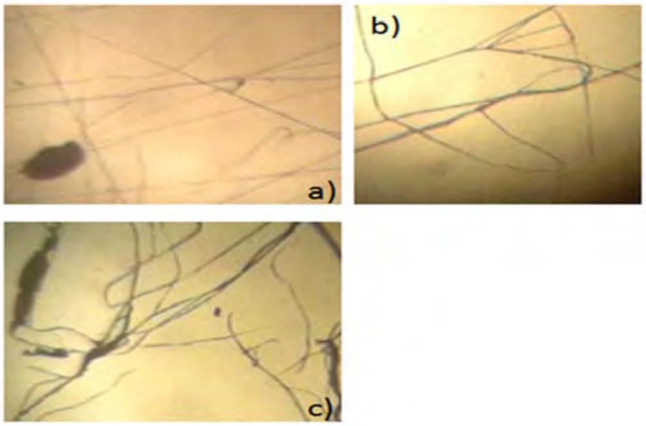

FIGURE.11. PHOTOGRAPHS TAKING THRU THE MICROSCOPE A) 24.1 WT% PVDF + DMF, B) 26 WT% PVDF + DMF AND C) 29.8 WT% PVDF + DMF.ACKNOWLEDGMENT

The solution containing PVDF with 3:1 ratio of DMF and Acetone which gave the thinnest fibers was 22 wt%. In 18 wt% you can see that there were all droplets. At 20 wt% you can see that there were some very thin fibers with some droplets. The 22 wt% produced very thin fibers and no droplets. The 24.9 wt% produced very thick fibers that are not in our range.

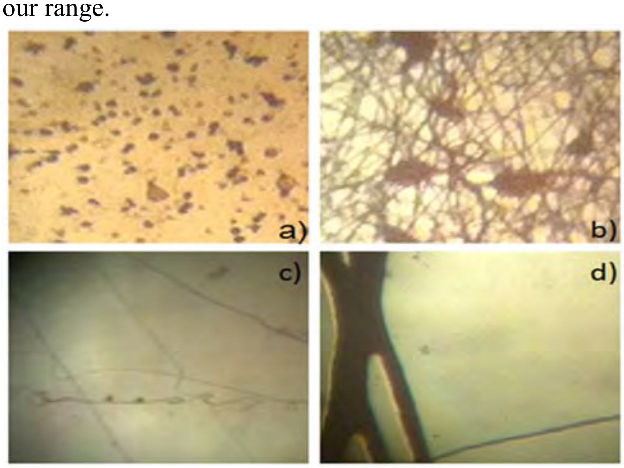

Figure.12. Photographs taking thru the microscope a) 18 wt% PVDF 3:1 DMF + Acetone, b) 20 wt% PVDF 3:1 DMF + Acetone, c) 22 wt% PVDF 3:1 DMF + Acetone and d) 24.9 wt% PVDF 3:1 DMF + Acetone.

The solution of 22 wt% PVDF 3:1 DMF + Acetone was the better solution, because the nanofibers were within the ranges of 100nm to 250nm. A solution between 24 wt% and 26 wt% of PVDF + DMF to be a good solution to also create nanofibers in the range required.

ACKNOWLEDGEMENTS

The author would like to acknowledge the support of the National Science Foundation, through NSF REU grant no. 1062672. Thank you to my advisor Dr. Jorge Santiago at the University of Pennsylvania, my mentors Dr. Carlos Perez, and Timothy Jones, as well as my lab partner Raymond Lopez.

REFERENCES

[1] Kurzweilai.net, 'A future cochlear implant with no exterior hardware required | KurzweilAI', 2014. [Online]. Available: http://www.kurzweilai.net/a-future-cochlear-implant-with-no-exterior-hardware-required. [Accessed: 16- Jul- 2014].

[2] Physicsclassroom.com, 'The Human Ear', 2014. [Online]. Available: http://www.physicsclassroom.com/class/sound/Lesson-2/The-Human-Ear. [Accessed: 16- Aug- 2014].

[3] Etd.ohiolink.edu, 2003. [Online]. Available: https://etd.ohiolink.edu/rws_etd/document/get/ucin1065654653/inline. [Accessed: 16- Jun- 2014].

[4] Lolatbio.wikispaces.com, 'lolatbio - The Ear', 2007. [Online]. Available: http://lolatbio.wikispaces.com/The+Ear. [Accessed: 16- Jun- 2014].

5. Asha.org, 'Types of Hearing Loss', 2014. [Online]. Available: http://www.asha.org/public/hearing/Types-of-Hearing-Loss/#sthash.a5mAsIdY.dpuf. [Accessed: 05- Jun-2014].

[5] Cochlear.com, 2013. [Online]. Available: http://www.cochlear.com/wps/wcm/connect/in/home/understand/hearing-and-hl/what-is-hearing-loss-/types-of-hl/sensorineural-hearing-loss/sensorineural-hearing-loss. [Accessed: 16- Jul- 2014].

[6] Nidcd.nih.gov, 'Cochlear Implants', 2012. [Online]. Available: https://www.nidcd.nih.gov/health/hearing/pages/coch.aspx. [Accessed: 16- Jul- 2014].

[7] M. Trimarchi, 'HowStuffWorks "Harvesting Energy from Human Movement "', HowStuffWorks, 2013. [Online]. Available: http://science.howstuffworks.com/environmental/green-science/house-music-energy-crisis1.htm. [Accessed: 04- Jul-2014].

[8] M. Trimarchi, 'HowStuffWorks "Harvesting Energy from Human Movement "', HowStuffWorks, 2008. [Online]. Available: http://science.howstuffworks.com/environmental/green-science/house-music-energy-crisis1.htm. [Accessed: 16- Jun-2014].

[9] B. Kandell, 'Piezoelectric Polymer (PVDF) Ribbon for Cochlear Implantation – Guidelines and Comparisons with Toothbrush Style Prototypes', 2006.

[10] Fluid.ippt.gov.pl, 'Slawomir Blonski - Electrospinning of polymer nanofibres', 2005. [Online]. Available: http://fluid.ippt.gov.pl/sblonski/nanofibres.html. [Accessed: 06- Jun- 2014].

[11] Flavio Noca, Jimmy Xu. Nanoscale Ears based on Artificial Stereocilia. ASA/NOISE-CON 2000 Meeting, Newport Beach, CA, December 5, 2000.

Design of a Frequency Selective Structure Using Space Filling Curves

Antonio Basukoski – Columbia University (Electrical Engineering)
NSF Summer Undergraduate Fellowship in Sensor Technologies - University of Pennsylvania
Advisor: Prof. Jan Van der Spiegel, Matt Zhu, Dr. Milin Zhang

Abstract-- **Mechanoreceptors are organic sensory receptors present in the skin that respond to mechanical pressure or distortion. At present, people who undergo amputations are fitted with prosthetics that provide a variable range or motion, but cannot replicate the function provided by mechanoreceptors. A totally passive wireless sensor network with multiple sensor nodes can be used to sense stretch, strain or pressure and address the lack of mechanoreception in prosthetics. A sensor node consists of a sensor antenna, a switch, an RF-DC converter and an identification antenna. Flexible compact size space-filling curve-shaped antennas serve as sensor antennas, and non-flexible antennas excited with a unique ID frequency serve as identification antennas. The sensor antenna works as a dipole antenna and uses the change in resonant frequency to measure the amount of stretch or pressure. This paper provides some characterization of the change in resonant frequency of the sensor antenna based on changes of different antenna properties, such as the length of the Hilbert curve, the width of the Hilbert curve, its thickness, and different background materials. Our simulation results show that the change in the length of the antenna produces a significant shift in the resonant frequency, whereas the change in width and thickness produce negligible shifts. These results are also verified experimentally and compared with our simulations. The experimental results are consistent with our prediction about the factors that change the resonant frequency of the sensor antenna, and further work can show how these shifts in resonant frequencies can be better quantified.**

I. INTRODUCTION

Today there are limited options for people who have suffered amputations. One of the most notable and severe repercussions of the procedure is the loss of a host of functionalities of our natural limbs, such as mechanoreception and thermoreception. They are both part of what we call tactile sensation, which uses our own natural sensory receptors embedded in the skin. We have four different types of mechanoreceptors: Meissner corpuscules to sense heavy pressure, Pacinian corpuscules to sense vibration, Merkel disks to sense light touch and Ruffini endings to sense stretch. They are a building block of our very complex somatosensory system, our body's own 'tactile sensor grid', which is constantly relaying information about our surroundings to our brain, necessary to handle objects and perform delicate tasks in our environment based on the tactile sensory feedback we receive.

Artificial limbs can restore some of the function of our natural limbs, and at present, this is generally restricted to the motoric function of the musculoskeletal system. Advancements have made it possible for artificial limbs to be controlled by superficial EMGs (electromyogram), so users could move limbs by twitching different muscles, but they have no way to gauge the strength of their grip, making this an incomplete, and in some applications, impractical solution. There has been some success in using electronic sensors in prosthetics for sensing, but these solutions require active circuits, which require a power source to operate. Such energy sources are prohibiting because they are finite and need to be recharged in order to stay mobile.

Our proposed flexible sensor antennas are completely passive (as opposed to active), which means that they do not require a power source (such as a battery) to be attached to the antenna, giving it more utilitarian flexibility and efficiency. Our passive scattering antenna sensors make use of their resonant frequency, a property that is intrinsic to their material and geometry, and as such requires no additional inputs. The scattering antenna works similarly to a dipole antenna. The passive antennas make use of space-filling curves, which are compact fractal geometric structures, so by bending and stretching the flexible antennas we can vary the length of the line segments of these curves, which changes the total electrical length of the antenna, and therefore changes the resonant frequency of the antenna. We use this resonant frequency to determine the extent to which the antenna has been stretched or bent, and from that information we can deduce the amount of pressure used or force applied. Our challenge now is to characterize all the different parameters that affect the antenna performance, such as size and environmental factors, and use the characterization to build a fully functional model and later, a prototype.

II. Background

2.1. Hilbert Curves

A space filling curve is special type of curve whose range contains the entire 2-dimensional unit square, and can be described by a continuous function whose domain is the interval [0, 1]. It can intuitively be thought of as a point moving through the endpoints of the unit square. This results in a curve which never intersects itself and whose complexity can be easily increased. The complexity of a space-filling curve increases with the number of its order. Hilbert curves are continuous, space-filling curves described by mathematician David Hilbert. Because of their geometry, Hilbert curves are very compact. This fact is important to us because a Hilbert curve flexible antenna with a small enough footprint to fit on a fingertip can achieve a sufficiently wide range of resonant frequencies to be used as a sensor. The sensor antenna is a passive scattering antenna, and it operate similarly to a dipole antenna, with each of its line segments polarized separately.

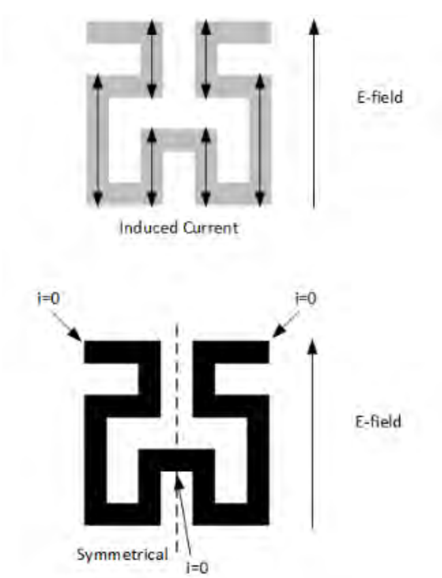

Figure 1. Operation principle of a Hilbert curve-shaped passive scattering antenna

A Hilbert curve shaped antenna has a lot of line segments whose length can be changed at once by the same applied force which achieves a multiplication effect in the change of the electrical length of the antenna. This is the reason why this antenna can achieve a greater range of resonant frequencies than a straight line dipole antenna. Fig. 1 shows the first six orders of the Hilbert curve with increasing complexity (left to right, bottom to top). We are mainly using the second order curve for its relative simplicity in fabrication and calculation relative to the higher order curves.

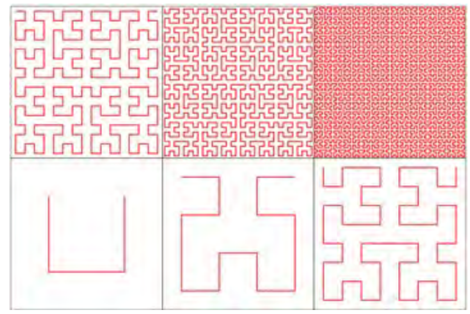

Figure 2. Family of Hilbert curves, orders 1-6, left to right, bottom to top

Figure 3. Flexible scattering antennas, liquid metal in PDMS

2.2. Computer Simulation Technology

In order to characterize the electromagnetic scattering response of the Hilbert curve antenna sample, we use CST (Computer Simulation Technology) Microwave Studio, which is part of CST, a specialized software suite for EM simulations in the microwave spectrum. CST allows users to model EM waves and their interactions with any arbitrary 3D structure. Using simulations to characterize the behavior of the antenna is preferable because it allows us to introduce idealized environments and therefore focus on the parameters of the antenna that we want to investigate without having to worry about artifacts from the testing environment. It also allows is to vary different antenna parameters to the extent which would be impractical with experimental methods. We want to investigate the effects of changing those parameters, such as the geometry of the curve, the distance from the EM wave source, and characterize them. In addition, once we have the model for the behavior of the antenna, we can introduce different environments and study its performance under different conditions.

2.3. Sensory nodes

The flexible passive scattering antenna is one endpoint of a sensory node. The sensory node is the implementation of the pressure/stretch sensing system. The proposed node utilizes the mapping between the resonant frequency of a passive scattering antenna to the change of shape or size of the antenna. Each sensor node consists of a sensor antenna, an identification antenna, and a radio-frequency (RF) to DC converter. A switch controlled by the identification antenna and the RF-DC converter selects the sensor node. To maximize the utilization of spectrum, the sensor antennas in all sensor nodes are designed to work over the same sensing spectrum range (1.5-2GHz). Identification antennas are designed to be narrow band and are excited with a unique ID frequency for each sensor node. Space-filling, Hilbert curve-shaped, compact-size flexible scattering antennas serve as the stretch/strain/pressure sensor. The identification antennas are made non-flexible.

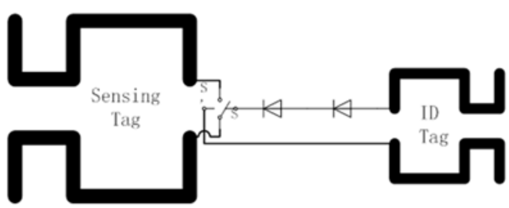

Figure 4. Proposed structure for the wireless stretch/strain/pressure sensor node.

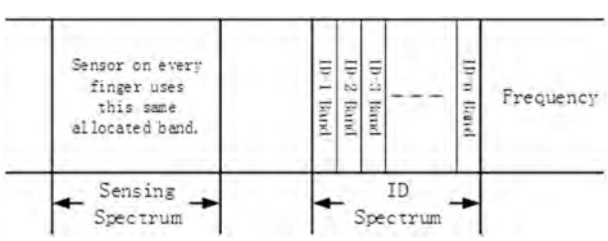

Figure 5. Spectrum allocation for the wireless sensor network.

2.4. S11 Parameter

The S11 parameter is known as the reflection coefficient (also called return loss and denoted by Γ). It measures how much power is reflected from the antenna back to the transmitter and is calculated as the ratio between the reflected wave and the incident wave. A higher S11 parameter The S11 parameter is often described in decibels (dB), which are a logarithmic unit used to represent the ratio between two quantities (from which one is always a reference value, as is the incident wave in our case) and is calculated as $10\log_{10}$(ratio).

2.5. Photolithography

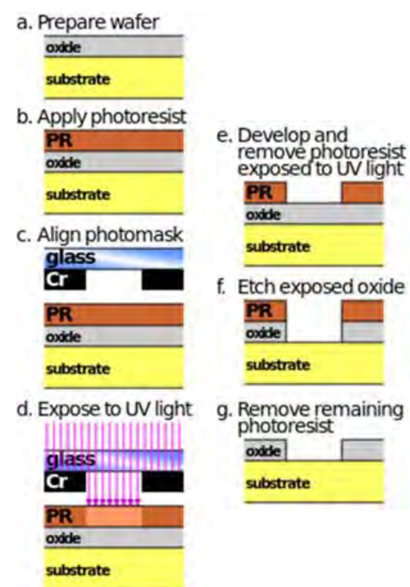

Figure 6. Photolithographic process

Photolithography is a micro fabrication process used to create patterns of a thin film material on a bulk of substrate material. The fabrication requires a sequence of chemical reactions and UV (Ultraviolet) light exposure. The process starts with cleaning the surface of the wafer to remove any impurities or residues coming from the environment. The next step is the application of a viscous liquid chemical known as photoresist which reacts when exposed to UV light. The photoresist is deposited by a machine that performs a procedure known as spin coating, which spins the sample at great velocity to form a micrometers-thick layer of the photoresist on the wafer. The wafer is then removed and exposed to heat in order to solidify the photoresist layer. Once it is solid, a prepared photomask with the desired pattern is applied on the wafer. The waver with the applied mask is exposed to UV light. The photomask pattern blocks the UV light from reaching the photoresist. The next stage called development requires the immersion of the waver in a developing solution which clears away the photoresist exposed to the UV light, so the pattern of the photomask is transferred on the wafer. The next step is the etching of the thin film material (a metal oxide) which is a chemical reaction that removes all of the exposed metal oxide material except the pattern protected by the photoresist. Now, with the desired pattern present on the substrate, the last step is to remove the photoresist. Fig.5 describes the photolithographic procedure. We used this photolithographic procedure to fabricate 2nd order Hilbert curve antenna testing samples.

III. METHODS AND MATERIALS

3.1. Simulation setup

We used the Finite Difference Frequency Domain (FDFD) method to calculate the S11 parameter for different samples in order to characterize and map different sample parameters with shifts in resonant frequency. The FDFD method is incorporated in the Frequency Domain Solver in the CST Microwave Studio software. We tested frequencies ranging from 1GHz to 10GHz.

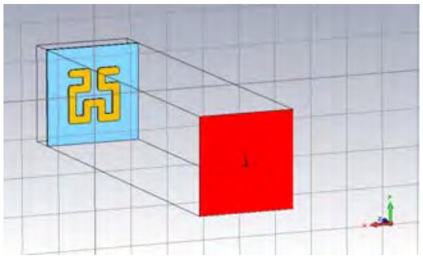

Figure 7. CST simulation model

Our model is built in an orthogonal axis 3-dimentional space. (Fig.7) The sample is centered at the XY plane, and placed at Z=0. The copper layer is 0.1mm thick, and the background material is 1.5 mm thick. The simulation boundaries are given by the thin black lines. The blue object represents the different background material on which the conducting Hilbert curve antenna material is placed. In our simulations, we used paper, FR-4, and just vacuum as a background material and copper for the antenna itself. We used perfect electric conductor boundary condition at the X plane (parallel) boundary, and a perfect magnetic conductor at the Y plane (parallel) boundary, and open (with space) boundaries at the Z plane (parallel) boundary. These idealized conditions simulate an infinite array of antennas, so that we can easily detect the resonant frequency of the sample. There is only one port, and it is placed at the edge of the Z boundary and it is pointed in the +Z direction. It uses the CST default excitation signal, and it has zero angle polarization.

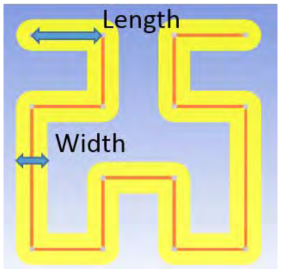

Figure 8. Antenna length and width parameters

We were interested in characterizing the different resonant frequency shifts due to change in length, width, and thickness of the antenna, as well as different background materials.

We also instigated the response of background materials with different relative electrical permittivity, and different thickness.

3.2. Photolithographic fabrication procedure

Our testing samples were fabricated using photolithography. The wafer used contains a 0.1mm copper layer on top of a 1.6mm FR-4 substrate.

- We applied Shipley Microposit S1818 positive photoresist to the surface of the sample
- We spin coated our samples at a velocity of 800 RPM, with 300 RPM/s acceleration, for 45 seconds.
- The samples were then baked on a hot plate at 110°C for 3 minutes.
- After application of the masks the sample was exposed to 500mJ/cm^2 dose of UV light.
- The samples were developed by soaking in a tetramethylammonium hydroxide aqueous solution
- We used an aqueous solution of one part HCl, one part H_2O_2, and three parts H_2O for etching the copper layer.
- After the etching, we used ethanol to remove the remaining photoresist.

We fabricated 2nd order Hilbert curved with 6mm, 7mm and 8mm length, and 3mm width. (Fig. 9)

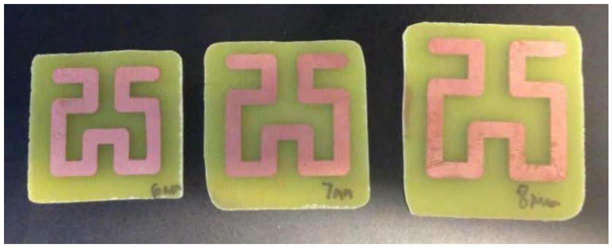

Figure 9. 6mm, 7mm and 8mm length 2nd order Hilbert curve antennas fabricated using photolithography

3.3. Experimental setup

The samples were tested in an anechoic chamber to remove any environmental factors. (Fig. 10)

Fig. 10. Experimental test configuration

We used a 2 port Agilent 8720ES network analyzer and a horn antenna with a 2-5GHz bandwidth to measure S11. The array sample was placed perpendicular to the horn antenna opening at distances of 1.2m, 2.4m and 3.6m.

We tested array sizes of 3x3, 4x4 and 5x5 built by equal length antennas of 6mm, 7mm and 8mm lengths and 3mm width. (Fig.11)

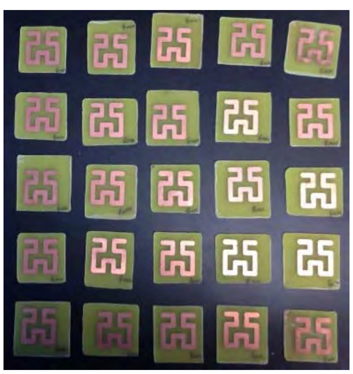

Figure 11. 5x5 array of 8mm length antennas

IV. Results

Our simulation showed that the relative conductivity and relative permittivity affect the response of the sample. Specifically, we showed that increasing the relative permittivity increases the magnitude of S11 as is shown in Fig. 12. This has implications on choosing an appropriate background material for the antenna, so that the background material will not distort the response of the antenna itself.

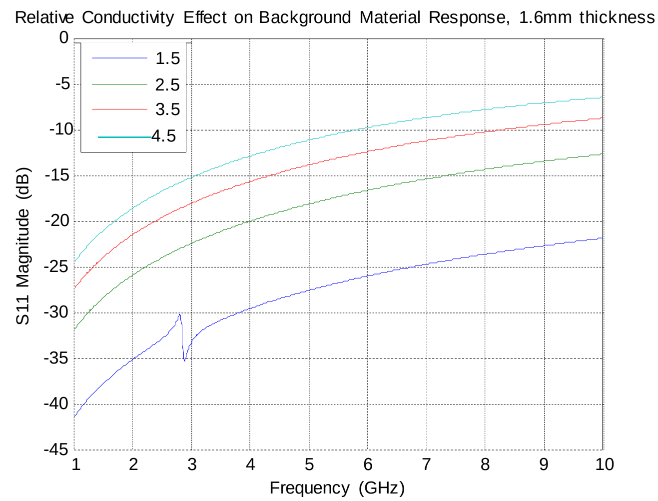

Figure 12. Relative conductivity effect on S11

Another parameter is the thickness of the background material. We showed that increasing the thickness of the background material makes its response more dominant in the total sample response, as shown in Fig. 13. We can see that the 2.5mm and 3.5mm thick background materials have S11 higher than -10dB even in the 1-4 GHz range, which would make them unsuitable for our use. This has implication on choosing a material which can support the antenna at a suitable thickness.

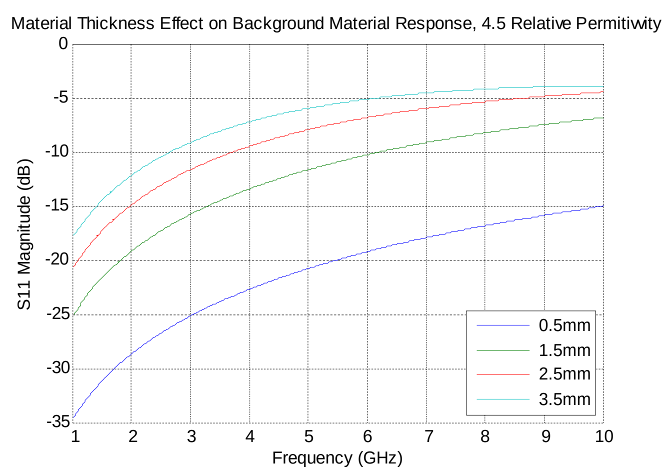

Figure 13: Thickness effect on S11

We also showed in a simulation that changing the length of the Hilbert curve shifts the resonant frequency regardless of the background material. Fig. 14 shows the S11 for the copper layer only, with not background material, and Fig. 15 shows the response of the copper layer on top of a 1.6mm FR-4 substrate. We can see the shift of resonant frequency clearly in both figures.

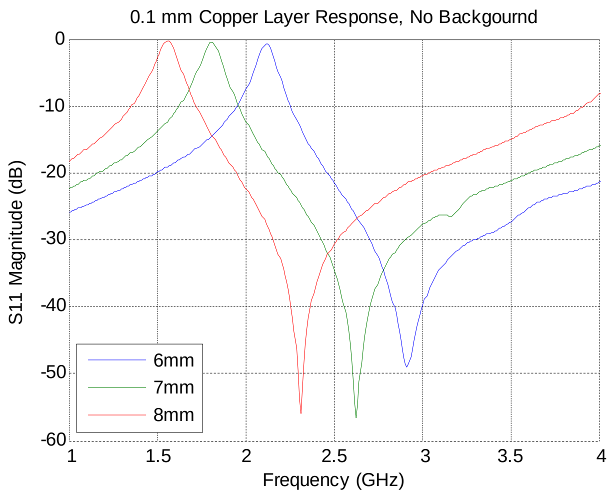

Figure 14. Shift in resonant frequency due to length change, copper layer with no background material

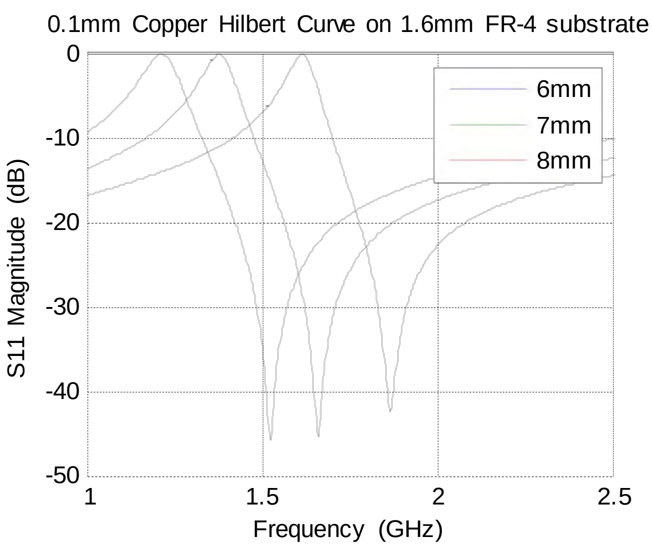

Figure 15. Shift in resonant frequency due to length change, copper layer on 1.6mm FR-4 substrate

We also simulated changes in the width and the thickness of the Hilbert curve. From the simulation results, we established that the change in width and thickness produces, for the purposes of our application, a negligible shift in the resonant frequency.

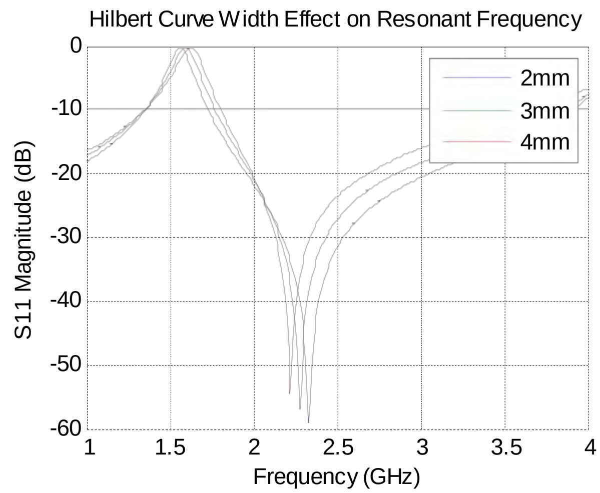

Figure 16. Shift in resonant frequency due to width change, copper layer only with no background

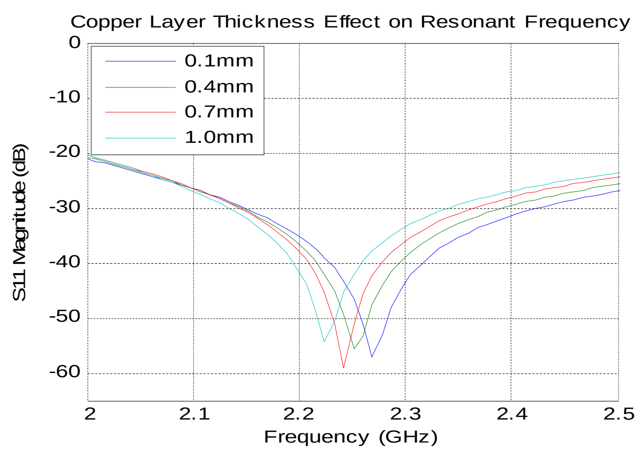

Figure 17. Shift in resonant frequency due to thickness change, copper layer only with no background

We verified experimentally that changing the length of the Hilbert curve changes the resonant frequency. The results in Fig. 18 are of a 5x5 array of antennas placed at 1.2m distance from the transmitting horn antenna. We can see that increasing the length of the Hilbert curve decreases the resonant frequency of the testing sample.

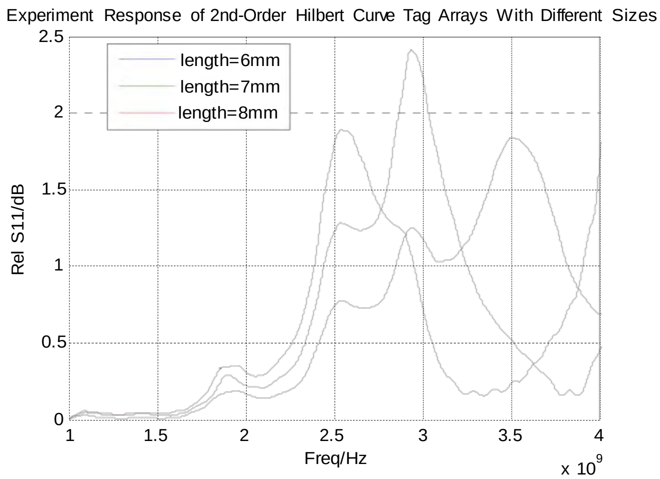

Figure 18. Experimental results of shifting resonant frequency due to length change

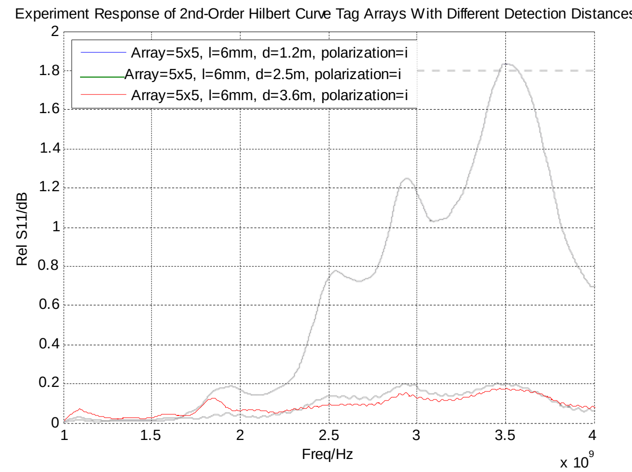

Figure 20. Change in magnitude of S11 due to increase in testing distance

We also observed that changing the array size produces a change in the magnitude of the sample response, but not a shift in the resonant frequency, which concurs with our theoretical prediction. We measured the strongest response with a 5x5 array, then a 4x4 array and the weakest response with a 3x3 array. (Fig.19)

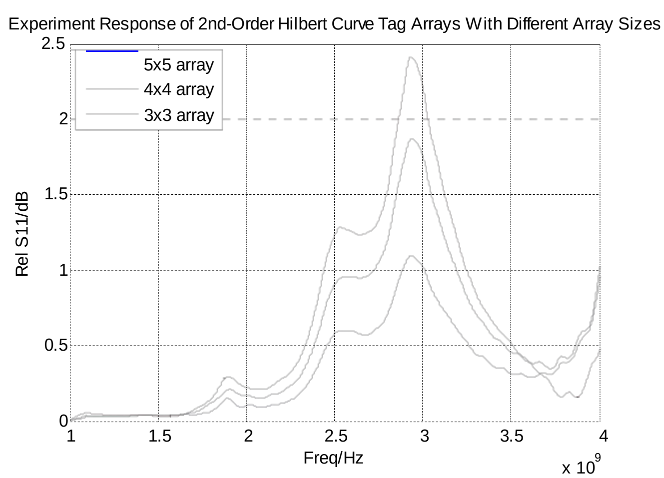

Figure 19. Change in the magnitude of the response due to change of array size

We also measured the response of the antennas arrays at different distances from the testing horn antenna. We measured at a distance of 1.2m, 2.4m and 3.6m. We observed that increasing the distance decreases the magnitude of the response. The results in fig. 20 are for a 5x5 array of 8mm length, and we can notice that the response at 2.4m and 3.6m are hard to distinguish from one another.

V. CONCLUSION

Our experimental findings support our simulation results that increasing the length of the Hilbert curve lowers the resonant frequency of the sample linearly. We also established that the length of the antenna is the primary factor that affects the resonant frequency, whereas the thickness and the width of the Hilbert curve, for our purposes, have a negligible effect.

Replicating the exact testing conditions in a simulation would require an impractically large calculation domain and cannot account for the exact testing conditions. A perfect conditions simulation setup allowed us to focus solely on the response of the Hilbert curve itself. The difference between the simulation results and our experimental measurements can be attributed to experimental error and the chosen simulation method and parameters.

VI. ACKNOWLEDGEMENT

I would like to thank Prof. Jan Van der Spiegel for giving me the opportunity to work in his lab this summer. I would also like to thank Matt Zhu, a graduate student in Prof. Van der Spiegel's lab, for all his help, patience and mentorship and Dr. Milin Zhang, a post-doctoral researcher, for all her support and guidance.

I would also like to thank the University of Pennsylvania for enabling research for undergraduates, the organizers of the SUNFEST program, and the National Science Foundation for providing the funding for this research.

REFERECNES

1. Saladin KS. Anatomy and Physiology 3rd ed. 2004. McGraw-Hill, New York.
2. IEEE online newsletters. Laursen, L., ‘Amputee Successfully Feels Prosthetic Grip Strength Via Arm Electrodes’ http://spectrum.ieee.org/tech-talk/biomedical/bionics/sensitive-prosthetic-hand-gets-a-grip. Feb. 2014
3. D. Hilbert: Über die stetige Abbildung einer Linie auf ein Flächenstück. Mathematische Annalen 38 (1891), 459–460.
4. Moon, B.; Jagadish, H.V.; Faloutsos, C.; Saltz, J.H. (2001), "Analysis of the clustering properties of the Hilbert space-filling curve", IEEE Transactions on Knowledge and Data Engineering 13 (1): 124–141
5. McVay, J.; Hoorfar, A.; Engheta, N., "Space-filling curve RFID tags," Radio and Wireless Symposium, 2006 IEEE , vol., no., pp.199,202, 17-19 Jan. 2006
6. Help and Examples Manual, CST Computer Simulation Technology AG, CST Microwave Studio 2014
7. Hayt, W.; Buck, J., “Engineering Electromagnetics”, McGraw-Hill Science/Engineering/Math; 8 edition, January 28, 2011

Miniature Hull Cell Device for Determining Effects of Additives in Copper Electrodeposition

Jennifer Bourlier (University of Michigan, Mechanical Engineering), *SUNFEST Fellow*

Dr. Haim Bau, Department of Mechanical Engineering and Applied Mechanics

***Abstract*— Over time, the charging capacity of rechargeable batteries declines. This is due to irregularities in the shape of the growth front that forms during the charging cycle. The ideal front is a smooth line but irregularities can occur. These instabilities make it more difficult for all of the particles to be converted back to energy during battery usage. Some attempts have been made to control the shape of the front using additives in the electrolyte solution. A device is needed that can explicitly show the effects of these additives. This project created a miniature Hull Cell device that can be used to study the effects of additives across a range of current densities in one run. It was shown that the device was effective in demonstrating the differences between various additives. Further studies must be made to evaluate the effects of such additives combined with active current control on the shape of the growth front.**

I. Introduction

From powering cell phones to storing wind energy, rechargeable batteries are used in many ways. Often people complain that over time the battery in their cell phone or laptop loses its ability to hold a charge for long periods of time. Serious decline in battery capacity can result in needing to recharge an electronic device more frequently, impacting ease of use for people. It can also lead to needing to completely replace devices and is a major obstacle for effective renewable energy storage.

During the charging cycles of batteries, ions diffuse together to form a growth front. The ideal front is a smooth line but morphological instabilities can occur. Examples of these are dendrites and bubbles [1,2,3]. These instabilities make it harder for all of the particles to be converted back to energy during battery usage, which depletes the energy capacity of a battery over time [1,2]. In order to develop more effective, longer lasting batteries, we need to regulate the charging cycle in order to prevent instabilities such as dendrite formation.

It has been suggested by Schneider *et al.* that adding lead to the electrolyte solution during copper electrodeposition could produce a smooth growth front [1]. It can, however, be difficult when testing additives to determine if a desired effect is being achieved because of the additive or due to other factors. It can also be tedious to test multiple additives and multiple current densities.

II. Background

A. Modeling Copper Electrodeposition

A model has been developed that demonstrates the behavior of the particles. Cu^{3+} particles engage in Brownian Motion with diffusion, essentially random movement with a random probability that they will move at any given time, until they reach a deposition surface [2]. Upon hitting the surface, the copper particles are reduced to Cu^{2+} [2]. They now engage in random motion along the surface of the electrodeposition, with random probability that they will move. If they randomly select to stay in place, they are now permanently stuck and become a Cu^{+} ion [2]. This simulation in MATLAB effectively simulates the way in which these particles behave.

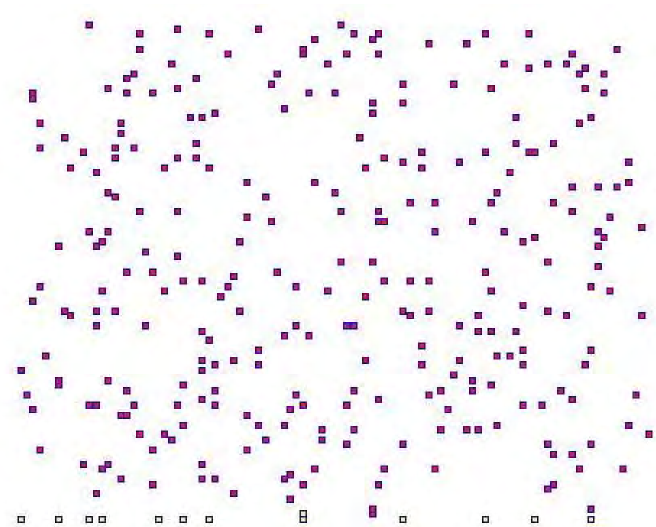

Figure 1. A still from the simulation. Particles on the bottom edge are forming the growth front.

B. Hull Cell

A Hull Cell is frequently used to perform small scale tests for large electroplating baths. This smaller test of large experiments shows the effects of certain additives across a large range of current densities. West *et al.* developed an equation that relates cell size to the current densities, allowing the current density to be determined at any point along a working electrode [5].

$$\frac{i(x)}{i_{avg}} = \frac{\left(x/_{L_H}\right)^{1.2733}}{\left(1-x/_{L_H}\right)^{0.359}}\left(1.733 - 0.763x/_{L_H}\right)$$

L_H is the length of the anode while x is the distance along the cathode. This design was repurposed to demonstrate the effectives of additives in solution on the micro scale by making a miniature version.

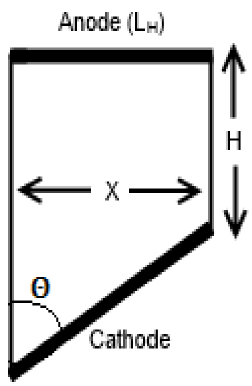

Figure 2. A diagram of a Hull Cell [4].

Due to the trapezoidal shape of the cell, the current density along the working electrode varies greatly [4]. Using the equation by West *et al.* and an applied current of 5 µA, a large range of current densities can be observed.

x(m)	L (m)	iavg(A/m^2)	**i(x) (A/m^2)**
0.0001	0.001	236.2204724	**21.66149093**
0.0002	0.001	236.2204724	**52.10468119**
0.0003	0.001	236.2204724	**87.18113973**
0.0004	0.001	236.2204724	**126.1628815**
0.0005	0.001	236.2204724	**169.395496**
0.0006	0.001	236.2204724	**218.4118956**
0.0007	0.001	236.2204724	**277.0622124**
0.0008	0.001	236.2204724	**355.6946096**
0.0009	0.001	236.2204724	**493.9815703**
0.0009999	0.001	236.2204724	**6252.707698**

Table I. Range of current densities observed in the cell.

III. FABRICATION

The miniature Hull Cell device is laser cut out of a chip of 0.02 meters by 0.02 meters by 0.0032 meters acrylic plastic. The device is 0.001 meters long and 0.000127 meters deep. There are lines extending off of the trapezoidal edges to allow for the electrodes to be placed. These lines are etched slightly deeper than the rest of the cell to allow for easier placement of the electrodes. Two pieces of 0.0001 meter copper wire approximately 0.1 meters long were cut. One inch on both sides of the copper wire was placed under a flame to burn off the plastic coating on the wire to ensure there would be no barriers to deposition. One wire was placed on each side of the cell and taped onto the chip. These measurements follow the ratio of $H/L_H = 0.7385$ as outlined by West *et al.* [5].

Figure 3. The fabrication process.

IV. TESTING

Each copper lead was connected to a wire, which was connected to a power supply. The flat edge was the anode and thus connected to the positive plug. The diagonal edge was the cathode and was connected to the negative plug. A small droplet of solution was placed into the cell using a micropipeter. The power supply was turned on with a current of approximately 0.01A for 20 seconds. We repeated this experiment for three different solutions: commercial Ag platting solution, 0.1M $ZnSO_4$ in 0.5M H_2SO_4, and 0.1M $CuSO_4$ in 0.18M H_2SO_4.

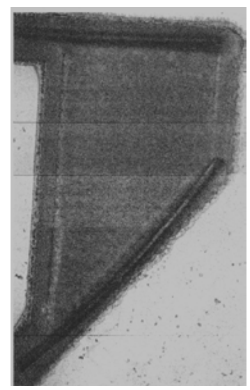

Figure 4. The Hull Cell under the microscope.

V. EXPERIMENTAL RESULTS

It was found that the solutions had a significant effect on the way that the growth front formed. The commercial Ag platting solution (containing proprietary additives) has a clean growth front. The front stretches completely down the electrode and has a uniform growth width. The acidified copper sulfate solution produced a different growth pattern. There was a large average amount of growth but the front is focused further up the electrode where the current density is higher. The acidified zinc sulfate solution produced a low average amount of growth that was very focused at the tip of the electrode where the current density is the highest.

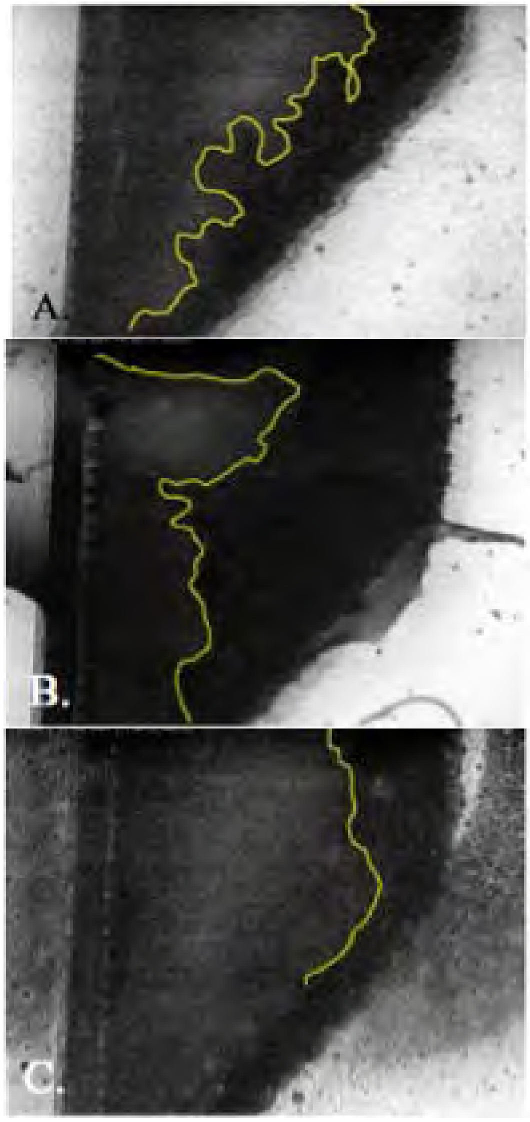

Figure 5. The growth fronts after electrolysis was completed.
A. The commercial Ag platting solution.
B. The acidified copper sulfate solution.
C. The acidified zinc sulfate solution.

VI. Discussion and Conclusion

These differences between the solutions indicate that solution chemistry has a large impact on the shape and size of the growth front. They also show the effectiveness of the miniature Hull Cell design in demonstrating the differences between growth fronts based on additives and the electrolyte solution composition.

This cell can be successfully used as an aid in maximizing the efficiency of deposition with the goal of improving the charging capacity and lifetime of batteries.

VII. Recommendations

Future testing should be done to implement the miniature Hull Cell in the testing of a lead additive in the electrolyte solution. The Hull Cell would be able to show if the improved growth front and charging efficiency is due to the lead or other factors.

Acknowledgment

This study was funded and supported by the National Science Foundation, through NSF REU grant no. 1062672, and the Microsoft Corporation through the Summer Undergraduate Fellowship in Sensor Technologies at the University of Pennsylvania. The author would like to thank Dr. Haim Bau of the Department of Mechanical Engineering and Applied Mechanics for the research opportunity and for his help and guidance this summer and Nicholas Schneider for his mentorship and support. Additionally, the author would like to thank the coordinators of the program, specifically Dr. Jan Van der Spiegel, Linda Kalb, and Josh Taton, for their tireless efforts throughout the program.

References

[1] Nicholas M. Schneider, Jeung Hun Park, Joseph M. Grogan, Suneel Kodambaka, Daniel A. Steingart, Frances M. Ross, and Haim H. Bau. “Visualization of Active and Passive Control of Morphology during Electrodeposition”. *Microscopy and Microanalysis,* 2014.

[2] Ross, F.M., Schneider, N.M., Park, J.H., Kodambaka, S., Steingart, D.A., and Bau, H.H., “Visualizing the effect of pulse plating during electrochemical deposition,” Materials Research Society Spring Meeting, 2014, San Francisco, CA.

[3] Schneider, N.M., Park, J.H., Grogan, J.M., Kodambaka, S., Steingart, D.A., Ross, F.M. and Bau, H.H., “In-Situ Electron Microscopy of Electrochemical Deposition, Dendrite Growth, and Etching,” 2013 IMECE Photogallery – Heat and Mass Transfer Visualization, 2013; San Diego, CA.

[4] A.C. West, M. Matlosz, D. Landolt. “Primary current distribution in the Hull cell and related trapezoidal geometries”. *Journal of Applied Electrochemistry,* vol. 22, pp. 301-303, Mar. 1995.

[5] Alan C. West. Electrochemistry and Electrochemical Engineering. An Introduction. 2012, pp. 140-143.

Playing with Transition Metal Dichalcogenides

Jamie Johnson (Electrical Engineering, Broward College), *SUNFEST Fellow*

A.T. Charlie Johnson and Carl Naylor, Nanotechnology

***Abstract*— Introductory background: Transition metal dichalcogenides (TMD) are semiconductors that have complementary properties of graphene. However, unlike graphene, these semiconductors have a band gap. The band gap is significant, because when the conduction band and valence band are separated, this enables the FET that are made with this material to have an on and an off state, unlike graphene that doesn't have band gaps in both states.**

Open Question or issue: Graphene was highly used in the making of biosensors until scientists found evidence that these sensors had no band gap. In my lab, we are using transition metal dichalcogenides, such as MoS_2 and WS_2, which have band gaps in both states, high on/off ratio, and are very sensitive in the detection of chemical analytes.

How the issue is being addressed: In this study, my lab group and I are working on making MoS_2., an n type semiconductor, into field effect transistors by growing MoS_2 flakes on a silicon wafer. Monolayer MoS_2 can be achieved by exfoliation or by Chemical Vapor Deposition (CVD), we will be using the later method to achieve our material. First we apply a dot of MoO_3 onto a silicon wafer and we slide this into our furnace, we then slide in a sulfur chip upstream. By using Nitrogen as our carrier gas we set the growth temperature for 800C and we wait 30 minutes.

Results: From experimentation, we have succeeded in growing these MoS2 flakes areas across the wafer.

Discussion: These TMDs are the best material for these biosensors because of their intrinsic properties. Scientists desire high electron carrier mobility, and a great on/ off ratio. Biosensors are needed in the medical field and homeland security, as well as in the agricultural industry. Also another TMD that we are doing work on is WS_2. This is a p type semiconductor that models the MoS_2 in many ways. The final objective is to put MoS_2 and WS_2 flakes together to make a P/N junction for solar cells. This is the future of nano and bio-sensing.

***Index Terms*—Biosensors, field effect transistor, graphene, monolayer, MoS_2, semiconductors, transition metal dichalcogenides, TMDs**

I. Introduction

With the discovery of graphene, monolayer transition metal dichalcogenides (TMDs) became the new hot topic for biosensors. TMDs are materials that have complementary properties of graphene, but these transition metals include a band gap. Having a band gap (tunable) is very important because it allows the material to have an on/off ratio. An on/off ratio means that when these materials are made into biosensors, they will be able to turn completely off after detecting. In graphene, there is no band gap meaning that the electrons are always shaking around and therefor the device will never turn off. Graphene is made of pure carbon in the form of a very thin (one atom thick), transparent sheet. It is very strong for its light weight and it conducts heat and electricity efficiently. Researchers have identified the bipolar transistor effect, ballistic transport charges and large quantum oscillations. Graphene is the basic structural element of other allotropes including graphite, carbon nanotubes, and charcoal. These allotropes were produced in the lab in 2004. This carbon allotrope was used for electro-optic devices because of its carrier mobility and its sensitivity. However, as further investigation went on, scientist found that graphene-based sensors had a zero band gap. This finding was the birth of TMDs. The whole objective scientist had in mind was to find materials that possess these properties (carrier mobility, on/off ratio, and high sensitivity). Molybdenum disulfide is one of the TMDs that are interesting. This TMD occupies a trigonal prismatic coordination sphere that is bounded to six sulfide ligands. An interesting property that this material possesses is that it has a tunable band gap, indeed when one switches from monolayer to bulk MoS_2, you are changing from a direct to an indirect band gap. Tunable is used in applications for photoluminescence.MoS_2 has high crystallinity, excellent optical properties, high on/off ratio and a carrier mobility of 10 cm^2. These properties will make this semiconductor a highly reliable biosensor.

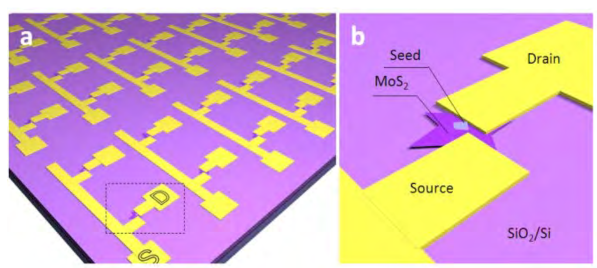

Figure 1 : When the Molybdenum disulfide flakes become much uniformed, adding a source and drain makes it into a device known as a Field effect Transistor.

There are two ways of producing these MoS_2 flakes which is chemical vapor deposition or exfoliation. When exfoliating, individuals use what is called the "scotch tape method". Scotch tape is used to peel bulk MoS_2 until it becomes monolayer. This is not a great way because the tape leaves behind residue and it makes the monolayer non- homogenous making it very complicated to use for the application of biosensors. Another way to produce flakes is by chemical vapor deposition (CVD). When doing CVD the monolayer flakes comes out perfectly shaped. This is due to the high intense temperatures of the furnace that yields single crystal monolayer MoS_2 flakes. Calculations have indicated that Molybdenum based transistors would consume on the order of 100,000 times less energy than silicon based transistors in the "off" state. The usage of these biosensors came about when reports went viral of dogs sniffing patients and sensing that they have diseases. Dogs have mu-optoid receptors in their noses that make their sense of smell so keen. Unlike humans that have only olfactory receptors, dogs have over 220 million olfactory receptors and smell parts of a trillion. This was a very interesting finding, so scientist thought of a way to replicate dog's keen sense of smell. The only possible option was to build an "electronic nose".

II. Experimentation

Making monolayer MoS_2 flakes is what we are doing in the laboratory. There are two types of growths that are used to make a MoS2 flake which is random and patterned. Random growths are done only when looking for flakes all over the substrate. This is usually a procedure used when looking for flakes at random areas, making sure that the flakes are not etched and monolayer. These samples are usually used for measurements such Atomic force microscope (AFM) or the Raman spectroscopy to look at the flakes up close and to measure the thickness of the triangular flakes. The thickness is usually 0.6nm high meaning that they are indeed one layer thick. Random growth is usually done by taking a stray piece of silicon wafer and electron spins it with sodium cholate. Then put a dot of AHM in two random edges of the substrate. Make a solid sulfur chip and place in the furnace. Growth conditions are 800 c for 30 minutes. This differs heavily from the patterned growth.

Figure 2: This diagram shows the way these flakes are obtained. Flow in the carrier gas of nitrogen; place a solid sulfur chip upstream and the substrate with a dot of Ammonium HeptaMolybdate downstream. The growth condition for this process is 800 c for 30 minutes.

These flakes are essential because if growing the flakes comes out successfully, then contacting them and making Field effect transistors will be in full effect. When the flakes grow in predetermined areas, we can make FET much easier. This led us to growing MoS2 in only predetermined areas. The four steps of making these flakes is lithography, evaporation, annealing and then finally growing. The first step of this process is to do optical lithography. Using the e beam machine and making wells on the substrate so that the Molybdenum (IV) oxide powder can be place into these wells. After that we take the substrate, put it into the evaporator, deposit up to 50 nm of Molybdenum oxide powder in the wells When the evaporation is done, lifting off the polymer by bathing the substrate in acetone and IPA is the next step.

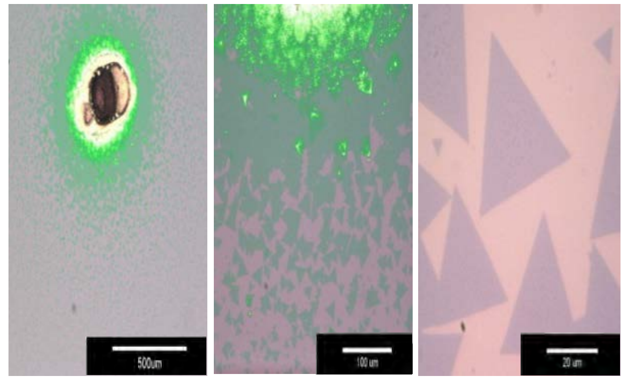

Figure 3: The flakes after a random growth process in the Chemical Vapor Deposition furnace. The three images show different magnifications of the scattered monolayer crystalized Molybdenum disulfide triangular flakes.

When all polymers are removed the substrate should be strictly Molybdenum disulfide. Annealing is the next step, cutting the substrate into two rectangular pieces and anneal at 300C for 20 minutes in a constant Nitrogen flow, is the process taken to start exposing the wafer to extreme temperatures. This is the last preparation step taken before actually growing. As for the growing process, many measures are taken to keep the wafer out of any harm of being damaged. Pretreatment of the SiO_2 surface has been shown to promote

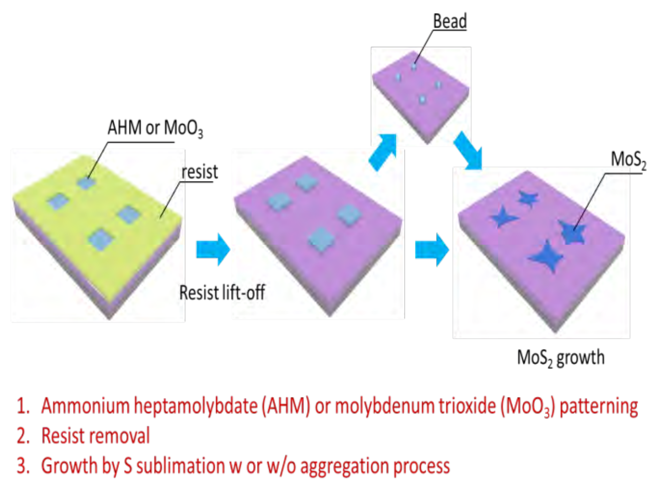

Figure 4: With patterned growth, there is four steps done in this procedure such as Lithography, evaporation, annealing, and the growth (CVD).

growth of MoS_2. Reports have shown that growths rapidly increased when the surface was coated with materials that contain carbon ring structures that persist at growth temperatures (reduced graphene oxide). When the wafer is done annealing put it in the UV radiation chamber for five minutes, pretreatment wafer with solution and electron spin it so that the solution is dispersed evenly over the substrate. Finally put the wafer in the CVD once again along with a solid sulfur chip and grow at 900c for 1 hour. These flakes usually come out in more predetermined areas and shaped very triangular. These two growth conditions are very important in this experiment and they show two different perspectives of the growths.

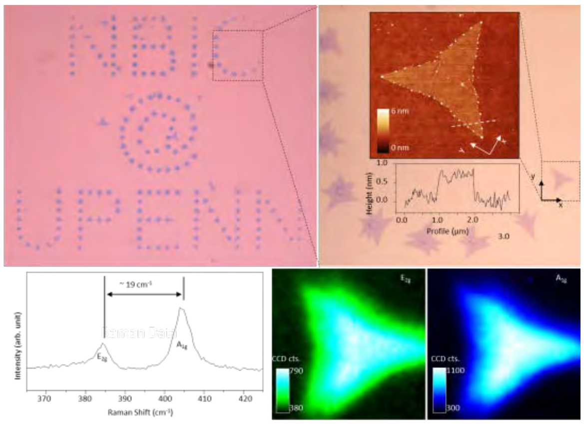

Figure 5: These flakes were done by a more sophisticated way of growing the flakes which is the Patterned Growth method. Images show from Atomic force Microscopy and Raman that these flakes are characteristics of monolayer flakes.

Atomic Force Microscope study shows that the height of one of the flakes is 0.6nm which is precisely an monolayer of MoS_2. Raman data also shows that the distance between the two characteristic peaks off MoS_2 is $19cm^{-1}$ which is also an indicator of monolayer MoS2. Further studies which include TEM show that these flakes are single crystal. So we were able to achieve pattern, monolayer and single crystal MoS_2. We can then imagine making arrays of devices and achieve thousands of FET and biosensors on one small chip.

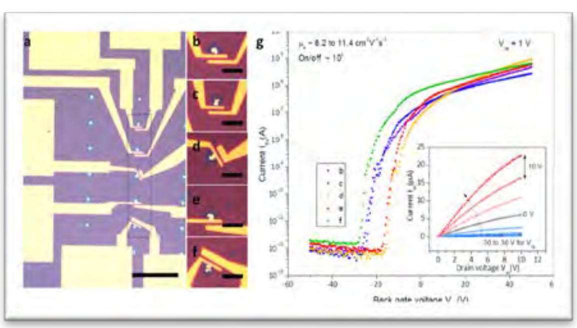

Figure 6: When flakes are contacted with the Field effect transistors they show their electrical properties which implies that they have band gaps. From the graph it shows that the current does start close to zero so it has an on/off ratio.

An etch step is used to define individual devices from a continuous layer of material, but this can run the risk of degrading a two dimensional material. Patterned growth approaches of creating the monolayer MoS_2 have the advantage of direct array fabrication without the etch process. To compare process compatibility with the conventional manufacturing, an array of MoO_3 growth seeds was patterned by lithography and the MoS2 monolayers were synthesized.

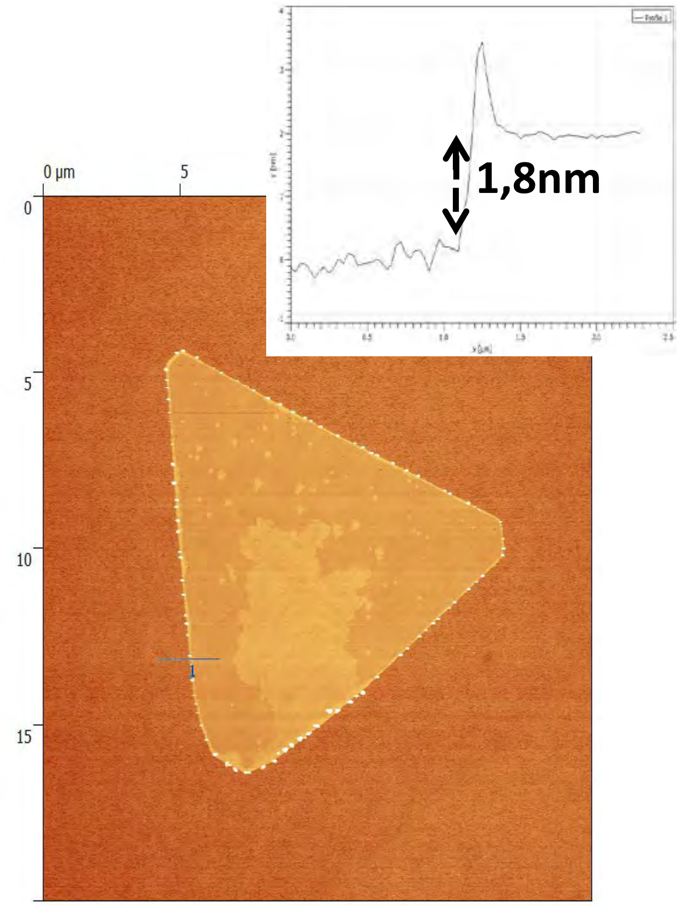

Figure 7: This image shows that we have successfully obtained a tungsten disulfide flake and the graph shows that it is indeed bilayer.

Tungsten disulfide is another TMD that is interesting because of its properties. WS_2 adopts a layered structure related to MoS_2, with the W atoms situated in a trigonal prismatic coordination sphere. In 1992, WS_2 was the first material found to make inorganic nanotubes. This emerging 2D layered semiconductor has a variable band gap (1.2 eV – 1.8 eV) and has shown promising applications in nano electronics. Reliable carrier mobility and conductivity are the desired properties of a great opto-electronic device. Even though there are papers all over the globe explaining ways to produce crystalized flakes of Molybdenum, WS_2 is not as popular because many individuals have not been successful at growing these flakes. Trying lithography, evaporation, and annealing theses flakes does not produce the same results. Studies showing that pretreatment to the silicon wafer has produced growth must not have meant in the case of dealing with tungsten. This one procedure of producing the flakes showed that it is not constant but it works. Evaporating tungsten powder on a silicon wafer is the first step. After evaporation, lift off the polymer so that the substrate will be pure WS_2. Anneal the wafer for 300 c for 20 minutes. Place

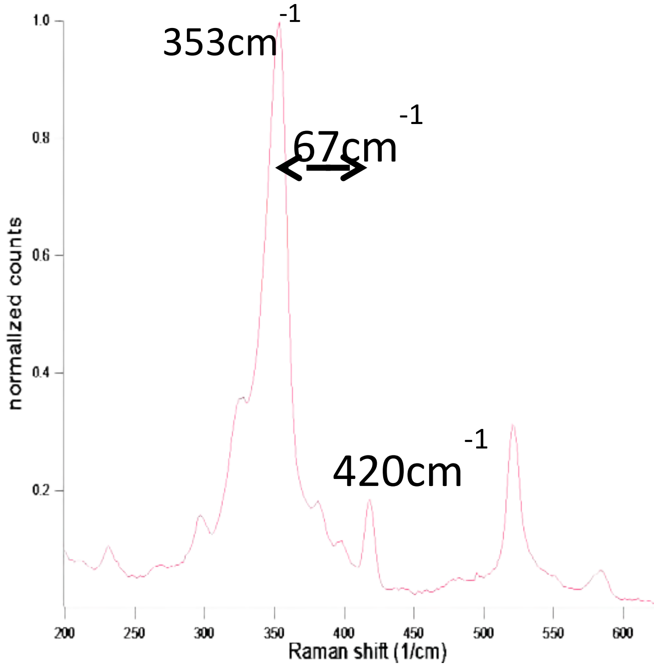

Figure 8: This graph is from Raman. The two peaks show that this flake is indeed tungsten disulfide. Also the difference between these two flakes shows that the flake is bilayer.

the substrate in a UV radiation chamber after the annealing process for five minutes. Next pretreat the wafer with the sodium cholate to diffuse the atoms and place it in the electron spinner. Make a solid sulfur chip and put both the chip and the wafer in the furnace (substrate in the middle and chip in the upstream). Growth conditions were 800 c for 1 hour and 500 sccm of nitrogen. Examining the substrate under the microscope, an array of WS_2 grew only under the markers not

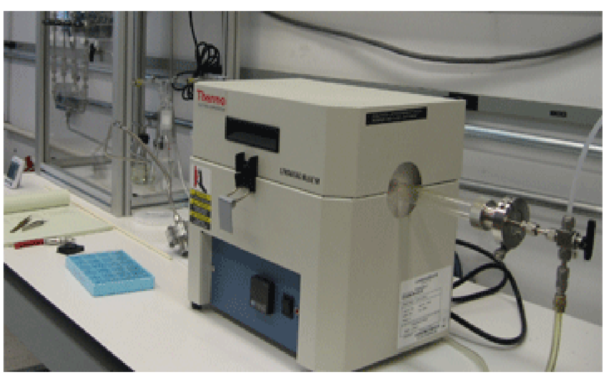

Figure 9: This is an image of the CVD furnace that is used in the lab to obtain random and patterned growth flakes. Exfoliation is not a great method because it leaves behind tape residue so it makes the flakes non-homogenous.

the whole substrate. Atomic Force Microscopy study of this flake showed it was bilayer, also Raman data also showed that the two peaks characteristic of WS_2 were present and that the distance between the two peaks was $67cm^{-1}$ which corresponds to a bilayer of WS_2.This was a sign of progression because other groups have tried growing these flakes but was not successful. The only way to finding solutions is to keep experimenting, changing conditions and observing how the flakes grow. Conquering this problem will open up endless possibilities for optical devices.

III. Results

Different conditions bring about different results of the MoS_2 flakes. This is a brief overview of a condition that worked perfectly. The silicon wafer was annealed at 300 c for 20 minutes. The nitrogen flow was at 500 sccm. When the 20 minutes was done, the substrate would then be put in a UV radiation chamber for five minutes. Then the substrate is put in the electron spinner and sodium cholate is put on the wafer to diffuse the atoms. As this process is in play, a solid sulfur chip is being made in the process. After all preparations are finally complete, the substrate and chip is put in the furnace (substrate in the middle and chip in the upstream). Setting the growth temperature to 900 c for 1 hour and at 500 sccm of nitrogen worked for growing an array of MoS_2 monolayer flakes. The flakes were much uniformed and they were monolayer thickness. These are results that are needed to be able to contact the field effect transistors.

IV. Discussion

Carbon nanotubes have the properties of detecting different chemical analytes by making these biological detections into electric signals. These nanotubes are placed on a silicon wafer with an oxidation layer, and electrodes are put on both sides formally known as the source and the drain. A gate voltage is applied to the channel and this helped to detect proteins and chemical analytes. Nanotubes are used to detect explosives, body odor, and even pesticides in the foods that we consume. MoS_2 is a N-type semiconductor meaning that impurities are added to permit electrons across the conductor. Seeing as how essential these biosensors are human life, scientists have been working extensively to improve the accuracy of these instruments. The three vital human applications these biosensors are used for is medicine, military usage, and in the food industry..

V. Applications

Biosensors have extensive applications in the food and agriculture industries. These devices contain a transducer and a biological element such as antibody, microbe, or organelle. Enzyme biosensors detect traces of organophosphates from the pesticides that may be harmful residues on farm products. These biosensors also are very sensitive in detecting ammonia and methane. But the most important role that biosensors play in the agriculture industry is that these biosensors can detect carbs, alcohols, and acids in fermented foods. They must be kept sterile, frequently calibrated and they require analyte dilution. With all of these life sustainable functions, biosensors are very important devices that are in demand. Humans consume foods on an everyday basis; many of us don't know what is in the foods that we eat so we must rely on the FDA and their reliable biosensors to make sure our health is not jeopardized.

In health care, biosensors have been the cream of the crop in detecting deadly diseases. In the emergency rooms, external biosensors are used as point of care diagnostic units. One example is the lab on a chip, which shows if a patient is in cardiac arrest from blood test samples. In point of care P.O.C) diagnostics, the instruments that patients use are small and hand held so that they can detect early signs of being sick. The success of a potential shift from curative medicine, to predictive, personalized and preemptive medicine could rely on the development of portable diagnostic and monitoring devices for P.O.C testing. Today the emphasis of care is shifting toward prevention and early detection of diseases, as well as management of multiple chronic conditions. In P.O.C, biosensors are used clinically for toxicology and drug screens, measurements of blood cells and blood coagulations, and the detection of cardiac markers in blood for heart disease. In the future, these devices are going to improve so rapidly that clinicians may be able to improve the regulation metabolism through bedside monitoring. Researchers are also working on efficient ways to find metabolism irregularities by developing a chemical sensor using a sample of blood from a finger stick. If a color change is detected as a metabolism defect, then the doctors will be able to help the infants as soon as possible. These sensors are very beneficial to the patients, because if they know what their illnesses are, then all the doctors have to do is just give them routes to getting better. With the technology of biosensors evolving so rapidly, many physicians are looking to have a wireless controlled biosensor that can detect an acute condition. From this information, another biosensor will be able to approximate an artificial organ and respond automatically without any user interruption. Biosensors can help save a lot of lives, and when this point of care diagnostics hit the market, the death rate should drop tremendously. In another five years these devices are going to be everywhere in the medical field.

The most important aspect of these biosensors is when they are used to detect biological warfare agents (BWA) for military purposes. Biological warfare agents may have different molecular structures/ mutations, but antibodies are only efficient for one type of BWA. Radio frequency identification is a critical sensor system that helps the military and homeland security personnel to identify potential terrorist attacks and take timely actions to minimize the dangers. Another tremendous benefit of these sensors is that the Air force can use these devices to locate, trace, and engage BWAs behind walls and containers. They can also continuously monitor camps and other properties to quickly identify these hazardous. If the government could get their hands on these devices, they could detect early signs and this could drop the casualty rate in the military tremendously. Biosensors used for these purposes are categorized in four groups such as electrochemical, nuclei acid, optical and piezoelectric. The need of a light weight instrument capable of performing immunoassays of toxins or infective diseases in warzones is very demanding. Another type of biosensor that is needed for this application is a diode-laser based sensor. This sensor detects particles over a wide range of area and is very time efficient. The invention of these highly demanding sensors are much needed so transition metal dichalcogenides are what scientist need to make these reliable sensors.

VI. Conclusion

At the end of this experiment, we have grown high quality MoS_2 flakes. MoS_2 has helped make devices used for sensing chemical analytes and different proteins binded to each other. Many more devices are in the making but much needed research has yet to be done on some aspects of the sensors. Also we have successfully grown flakes of WS_2 but it cannot make actual devices yet because the flakes are not reproducible. Tungsten disulfide is very tricky because with the random and patterned growth process, we were only able to grow around the markers but not on whole substrate. I firmly believe that the sodium cholate that we are using is not working for the silicon wafer when tungsten is evaporated on the substrate. Research is still in effect on this semiconductor so hopefully more research will show exactly what promote the growth of these WS_2 flakes. But with the work we have performed, we are getting closer to unraveling the mystery of WS_2 monolayer flakes. The only downside to the growth conditions is that they are very climate dependent. From the humid weather, our flakes have come out very distorted and etched. They are not very consistent because of this effect so one growth may grow but the other growth you do may not go and the conditions are totally the same. Studies have shown that the flakes of both MoS_2 and WS_2 have been more consistent in the winter then in the summer. Only thing possible to fix this problem is to keep experimenting and follow the trends of the flake.

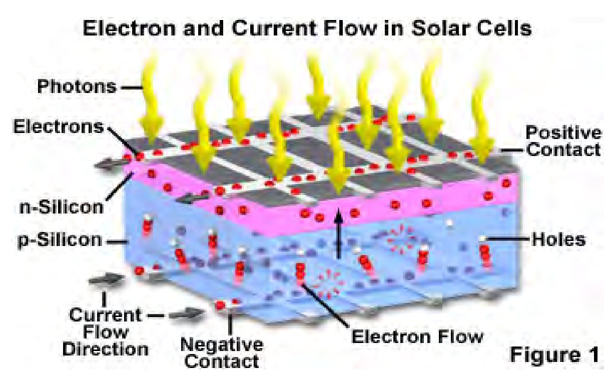

Figure 10: This is the future of bio-sensing. If we could get tungsten disulfide which is a P-type semiconductor and molybdenum disulfide which is an N-type semiconductor to grow simultaneously and link them together we can obtain a P/N junction for FETs or a solar cell.

Acknowledgment

The authors would like to acknowledge the support of the National Science Foundation, through NSF REU grant no. 1062672.

REFERENCES

[1] www.news-medical.net/heallthy/biosensors-and
[2] www.pcmag.com/articlez/
[3] http://report.nih.gov/nihfactssheets/viewfactsheet.asp
[4] www.pubs.acs.org/doi/full/
[5] www.connection.ebscohost.com/
[6] www.sbir.gov/sbirsearch/detail/

Signal Processing for a Directed Audio Warning System on Buses

Marcus Pan, University of Pennsylvania, Electrical Engineering, SUNFEST Fellow

Advisors: Dr. Daniel Lee, Electrical and Systems Engineering, University of Pennsylvania

Alex Burka, Electrical and Systems Engineering, University of Pennsylvania

Research Partner: Justin Aird, Electrical Engineering, Virginia Polytechnic Institute and State University

***Abstract*—Bus-pedestrian collisions often take place at road intersections, while buses turn and pedestrians cross the street distractedly. A warning system that alerts pedestrians in front of a turning bus would decrease the number of collisions. To build an effective warning system, we propose the use of directed speaker technology. This would alert only the pedestrians in the way of the bus and not disrupt an entire street corner.**

This paper discusses the design of the signal processing components for a directed audio warning system. Sound is first modulated to an ultrasonic frequency for transmission. This high frequency signal would travel in a narrower beam compared to a low frequency signal from a source of similar dimensions. It would then be demodulated back to the audible range by nonlinearities in air pressure. Such a system requires precise signal processing to obtain a result with low distortion. This paper will discuss the modeling of that signal processing in MATLAB and its implementation in a microcontroller. The MATLAB model was compared to a working prototype that involved mainly analog components, and the results discussed where significant. Various issues and challenges regarding the microcontroller implementation are also discussed, and compared to issues with the analog circuit prototype. The MATLAB model and microcontroller implementation is aimed at making the system more robust by enabling the testing of different parameters and reducing part count.

***Index Terms*—Acoustic signal processing, audio compression, band-pass filters, digital signal processing, microcontrollers, pulse width modulation, road accidents, ultrasonic transducers**

I. Introduction

Many bus-pedestrian collisions occur at road intersections. The Pennsylvania Department of Transportation, in its crash facts and statistics handbook for 2013, reported intersections as the most common place for accidents that involve pedestrians (see Fig. 1) [1]. Road safety studies, and an interview with a bus driver, show that intersections are accident prone because of the bus driver's blind corner when turning [2], as well as the distracted nature of pedestrians who focus on mobile devices while walking [3].

A possible solution to this problem would be to install an audible warning system on buses that would alert pedestrians

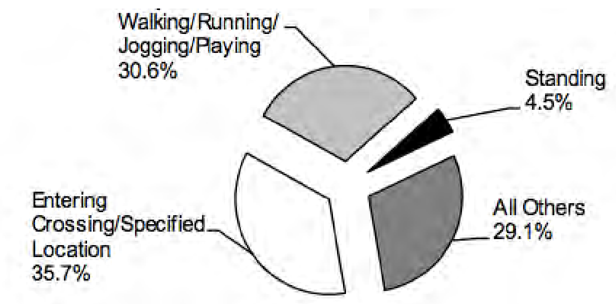

Figure 1—Pedestrian Activity during Crashes [1]

to the turning bus. Such a system has already been implemented by the Cleveland Regional Transit Authority, where a turning detection system was fitted into the steering column of buses and a vocal warning played from speakers inside and outside the bus [4]. However, complaints about public noise abounded after its installation, and one can imagine the same concern in any urban city already saturated with noise from traffic and construction.

This raises the following research problem: Can we design a warning system that effectively alerts only the pedestrians in the way of the bus? We propose such a system with directed sound technology. Research on this technology has increased recently, developing our understanding of how high frequency ultrasonic signals, which are more directed, produce audible frequencies when travelling through nonlinearities in the air [5]. However, few applications have employed this technology effectively as precise signal processing is needed to reproduce an audible signal with low distortion.

This paper will discuss the signal processing in our project to design a directed warning system for buses. The different signal processing units and their role in producing high quality sound from ultrasonic speakers are explained. The design process involved a simulation on MATLAB and implementation on a microcontroller (MCU). Important features and issues in the MATLAB model and MCU implementation are discussed.

II. Background

A. Principles of Sound Directivity

The directional speaker is a sophisticated and novel feature of our warning system. It ensures that our audio warning alerts only the pedestrians in front of the bus, without noisily disrupting the surroundings. The mathematical principles of sound directivity are presented in Pompei and Wooh's paper on phased arrays [6] and are explained further below.

The directivity of sound depends on the ratio of the speaker size to signal wavelength. To obtain this relationship, we start with the sound pressure as a function of distance *r* and angle θ from the middle of a source (see Fig. 2) [6]:

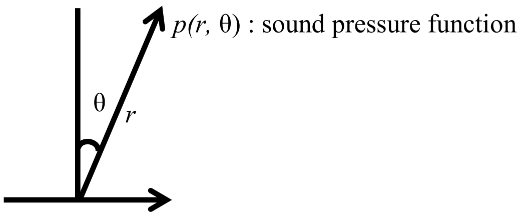

Figure 2—Diagram of Sound Pressure from a Point Source

$$p(r,\theta) = \frac{1}{r}e^{\frac{-j2\pi r}{\lambda}} \qquad x$$

s(x): source amplitude distribution
λ: signal wavelength

For a source with a uniform distribution function for the length of speaker, *L,* the amplitude distribution function can be replaced with initial pressure, P_0. Assuming the y-axis intersects the middle of the source, the integration interval is [-L/2λ, L/2λ]:

$$p(r,\theta) = \frac{1}{r}e^{\frac{-j2\pi r}{\lambda}} \int_{\frac{-L}{2}}^{\frac{L}{2}} P_0 e^{\frac{j2\pi \sin(\theta)x}{\lambda}} dx$$

For a simple model of directivity, we can disregard the constants, including terms involving *r.* We assume that *r* is constant while *θ* changes as we measure pressure around the arc of a circle. The following change of variables are also made for easier analysis:

$$x' = \frac{x}{\lambda} \quad ; \quad \beta = sin(\theta)$$

The scaled pressure equation with change of variables is represented by *H(β)*. We expand it further to obtain a function of the ratio *L/λ*:

$$\begin{aligned} H(\beta) &= \int_{\frac{-L}{2\lambda}}^{\frac{L}{2\lambda}} e^{j2\pi\beta x'} dx' \\ &= \frac{e^{j2\pi\beta x'}}{j2\pi\beta}\Bigg|_{\frac{-L}{2\lambda}}^{\frac{L}{2\lambda}} \\ &= \frac{e^{j\pi\beta\frac{L}{\lambda}} - e^{-j\pi\beta\frac{L}{\lambda}}}{j2\pi\beta} \\ &= \frac{j2\sin(\pi\beta\frac{L}{\lambda})}{j2\pi\beta} \\ &= \frac{\sin(\pi\beta\frac{L}{\lambda})}{\pi\beta} \end{aligned}$$

The relationship between sound directivity and the *L/λ* ratio can be visualized by plotting the absolute value of the equation above with different values of the ratio *L/λ* (see Fig. 3):

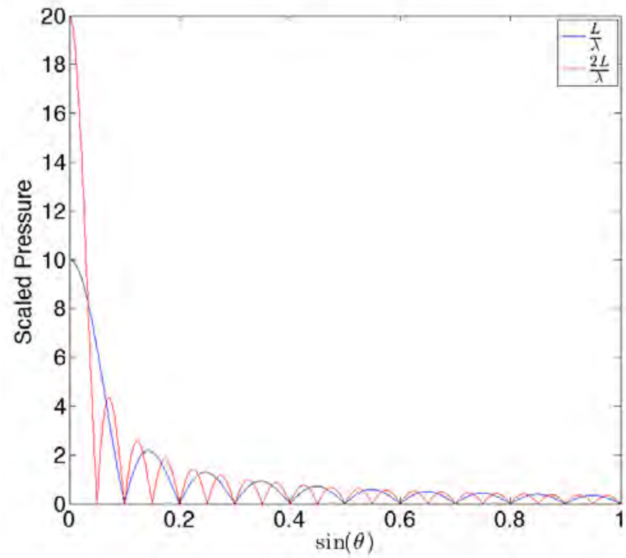

Figure 3—Plot of Sound Directivity with Different *L/λ* Ratios

Of the two signals plotted , one had a *L/λ* ratio twice as large as the other. The signal with higher *L/λ* ratio results is more directed. It has a higher maximum amplitude and attenuates more at wider angles. Hence we establish that a higher *L/λ* ratio results in more directed sound.

To obtain the higher *L/λ* ratio, we chose to emit a high frequency signal. Since our goal is to build a portable speaker set to be fit onto the front of the bus, increasing the speaker length extensively would not be feasible. Increasing the frequency however, which is inversely proportional to the wavelength, would increase the *L/λ* ratio.

However, the use of high frequency signals is restricted by the human hearing range (20 Hz—20 kHz). Nonetheless, nonlinear acoustical principles show that as signals travel through nonlinearities in air pressure, they change in velocity, and thus generate frequencies in the audible region [5] [7]. With precise signal processing, we can modulate a audio signal to an ultrasonic frequency, and it will be demodulated back to the audible range by nonlinearities in the air.

B. Experimental Verification for High Directivity of High Frequency Signals

We built a simple model for this directional speaker based on a public circuit schematic called the Soundlazer [8]. This system emits a 40 kHz wave through ultrasonic speakers. Initial testing of sound directivity was run in an empty classroom. The ultrasonic speakers were placed on a tabletop, and measurements of sound level were taken at distances along 3 lines—0°, 15°, and 30° from the source. The decibels readings from a particular speaker were normalized with the highest reading from that speaker, to account for different initial volumes across the speakers. The higher directivity of an ultrasonic speaker compared to regular speakers can be seen in the graphs below (see Fig. 4).

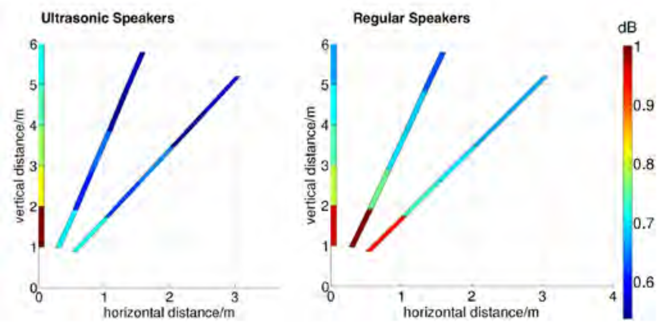

Figure 4—Comparison of directivity of Ultrasonic Speakers and Regular Speakers

The plots show that at wider angles, the signal from the ultrasonic speaker is more attenuated. This verifies its higher directivity.

III. SYSTEM ARCHITECTURE AND MATLAB MODELING

The mathematical and experimental proof for the higher directivity of higher frequency signals has been established. In this section, the signal processing involved that transforms an audio input signal to a high frequency output is discussed.

Our system architecture, derived from the Soundlazer design [8], has the following signal processing blocks.

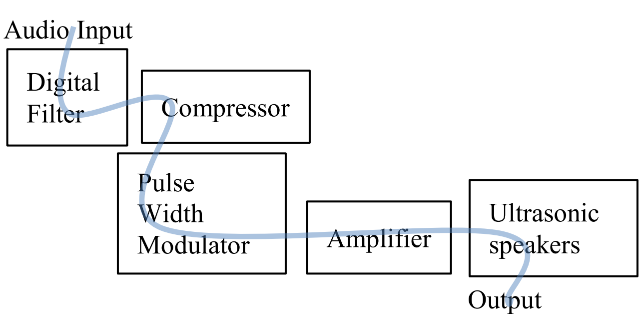

Figure 5—Signal Processing Blocks

The important, initial step before the implementation of these blocks was to simulate it in MATLAB. This would enable us to test different parameters easily, and analyze the output with MATLAB's plotting tools. A description of each component is offered below.

A. Digital Filter

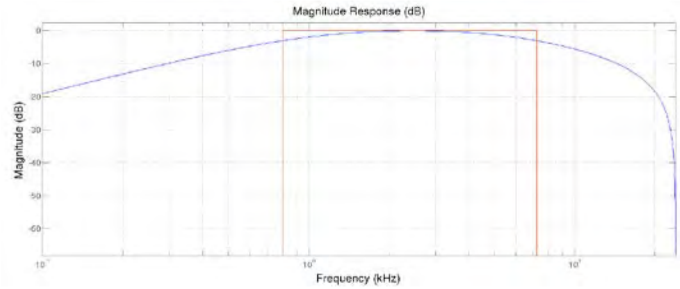

Figure 6—Frequency Response of Bandpass Filter

The digital filter modeled on MATLAB was a 2^{nd} order bandpass filter with a passband of 800 – 7200 Hz (see Fig 6). Human hearing is in the range of 20 Hz – 20 kHz, but the important frequencies of a warning signal would typically be less than 5 kHz. Hence our bandpass filter would eliminate frequencies that are not essential in our warning signal. We used the MATLAB filter toolbox, allowing us to change the 3dB frequencies (frequencies at which the magnitude of the signal changes significantly) of the filter easily.

We tested the model with an input 'siren' signal and plotted the spectrograph of the filtered and unfiltered signal. As can be seen in Fig. 7, the portion of the signal that is below 800 Hz is attenuated after filtering. With the low frequencies filtered out, the audio signal sounded sharper and more distinct, as the low frequencies had a muffling effect.

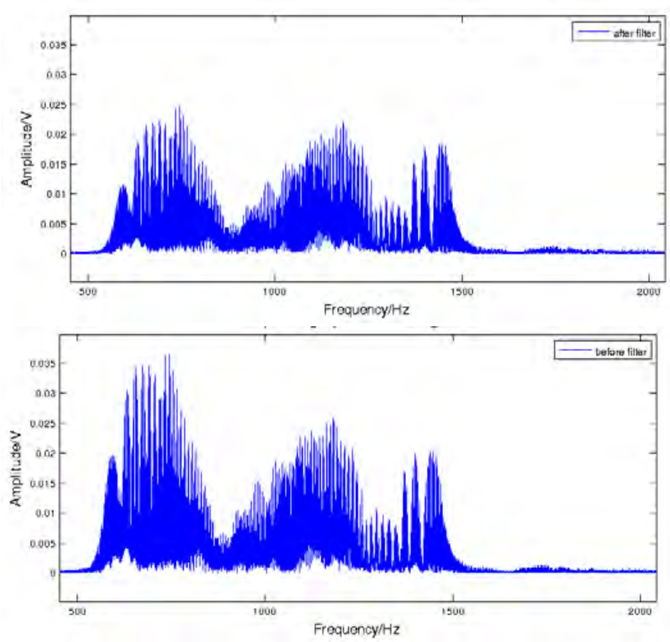

Figure 7—Spectrograph of Filtered and Unfiltered Signal

B. Compressor

The compressor allows the user to control the dynamic range of the audio input. The dynamic range is the difference between the loudest and softest levels. If a user wanted to reduce the dynamic range, the user could make loud signals softer, or soft signals louder. The compressor would thus provide specialized volume control of the output signal. In our model, this is achieved by plotting a compression curve, which maps the input dB level to the output dB level. This would be a piecewise linear mapping. The user can set the threshold points where the mapping function changes. Most audio compressors have an option of implementing a 'hard knee' or 'soft knee', which specify suddenness of the transition around the threshold points. This is can also be set in our model by plotting more points around the main threshold point to smoothen the change (see Fig. 8). The compression curve can be modified based on the volume characteristics of the input signal.

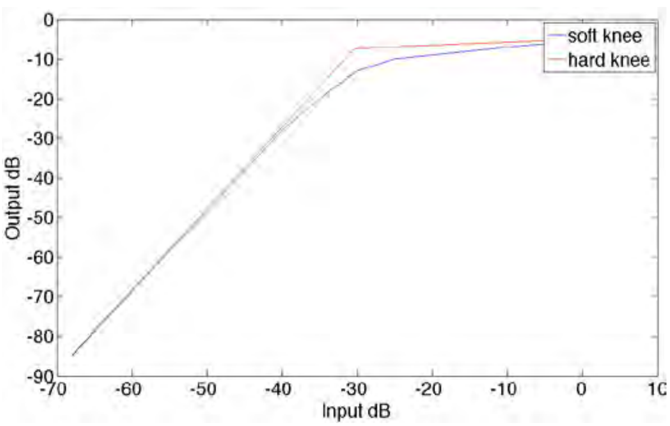

Figure 8—'Hard Knee' and 'Soft Knee' in Compression Curve

The dB levels are related to the signal's voltage amplitude based on the following equation:

$$V_{dB} = 20\log(\frac{V}{V_{ref}})$$

We used a Vref of 2.5 V, since it is the midpoint between a high (5 V) and low output (0 V). Since our input signal is a voltage amplitude signal, our compressor model first converts the voltage amplitude to its dB level, maps it to the output dB level, and then converts it back to an output voltage amplitude:

$$\boxed{V_{idB} = 20\log(\frac{V_i(t)}{V_{ref}})} \rightarrow \boxed{\text{Compression Curve Mapping}} \rightarrow \boxed{V_o(t) = V_{ref} \times 10^{\frac{V_{odB}}{20}}}$$

Figure 8—Block Diagram of Compressor Model

We collected data on the compressor implemented in the ADAU 1701 chip [9] used in the prototype, compared it to our model, and found to be satisfactorily close (see Fig. 9). The experimental results show a gentler initial slope and more ripple as the input voltage increases. The ripple could be due to reactive components in the actual circuit.

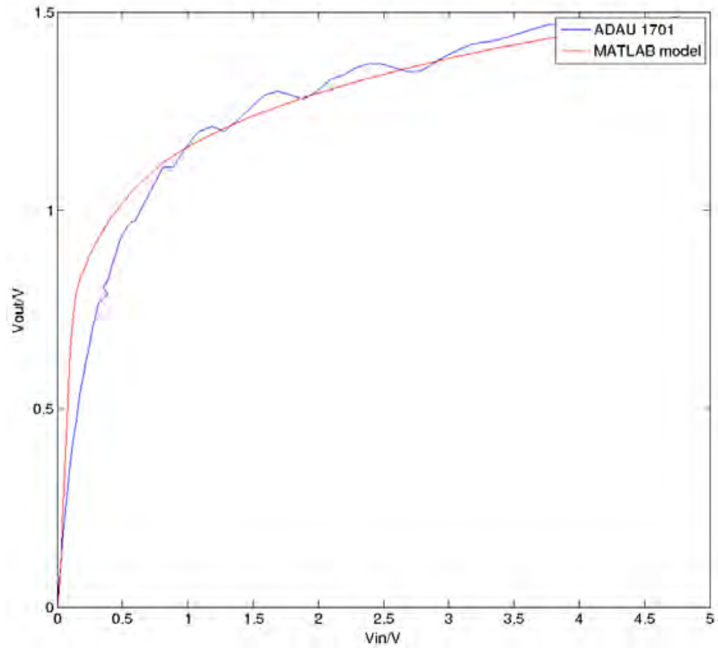

Figure 9—Comparison of Experimental Results and Compressor Model

C. Pulse Width Modulator (PWM)

After the input signal has gone through filtering and audio compression, it goes through a PWM that outputs a square wave at an ultrasonic frequency. The duty cycle of the square wave is modulated by the input signal. The ultrasonic speakers would eventually broadcast this square wave. Our model was based on the TL 494 PWM chip [10]. A high frequency 40 kHz sawtooth is generated as a comparator with the following conditions for the output (see Fig. 10):

Condition	**Output (HIGH = 5 V, LOW = 0 V)**
sawtooth > input	HIGH
sawtooth < input	LOW
input < 0	LOW

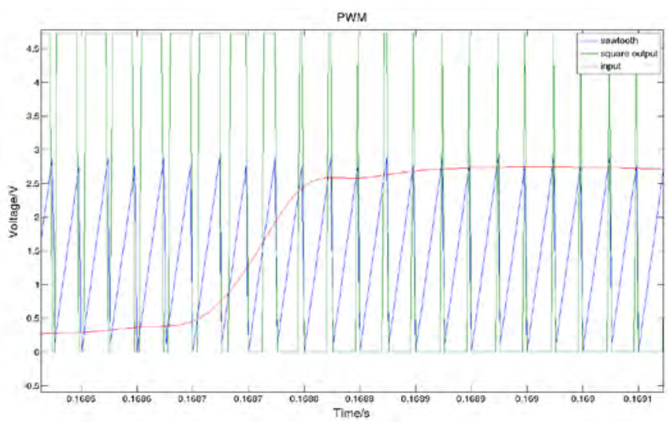

Figure 10—PWM Signal with Audio Input

Since the output just stays at 0 V when the input is negative or when the input is higher than the peak of sawtooth wave, the input signal is not modulated under these conditions. Hence, the input signal range should be within the upper and lower limits of the sawtooth wave. In the model, the user can ensure this range by changing the peak of the sawtooth, or of the DC voltage buffer. The DC voltage buffer will shift the input signal up or down by the value of the buffer.

We also implemented a dead time control (DTC) in our model. Without it, in the event that the input signal is always at 0 V, the output will be a constant HIGH. The DTC thus implements a maximum PWM duty cycle, so that the output will always be oscillating. In the example shown below, the duty cycle is capped at 80%.

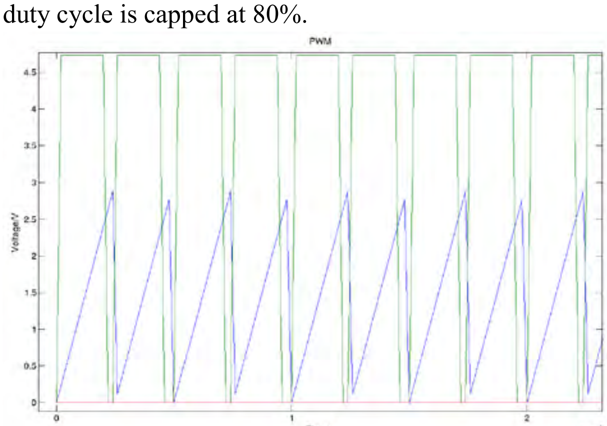

Figure 11—PWM Signal with Dead Time Control

IV. Microcontroller Implementation

For the microcontroller (MCU) implementation, we had a choice of using either a Digital Signal Processor (DSP), i.e. a microcontroller that specializes in signal processing, or just a general purpose MCU. We decided to start with the Intel Galileo, a relatively new general purpose MCU released in October 2013. Our evaluation of its suitability with our technical demands is summarized below:

Useful features:

1. Can install Linux, Python, and Node.js, providing a familiar development environment.

2. Many examples are provided in Arduino sketches. While we are not to using the Arduino libraries, these give good starting examples that we can refer to.

Limitations:

1. Most GPIO pins have a maximum throughput of only 230 Hz, which is too slow to output a 40 kHz signal.

2. Writing to the PWM driver through the Linux kernel only achieves frequencies of 14 kHz.

3. The external (outside the processor) Cypress PWM chip takes 2 ms to updates the output pins. We would need it to update before the end of a period (0.025 ms) to change the duty cycle for each period. We also could not use interrupts as they are only generated at the slowest clock speed (367 Hz)[11].

We started with just trying to output a PWM wave with changing duty cycle. To save processing power, the input signal could be preprocessed so that only the duty cycle information would need to be loaded onto the board.

However, as listed above, the Galileo could not output a 40 kHz pulse wave, with a changing duty cycle. This was mainly due to the slow communication bridge between the processor and the I/O pins.

The inability of the Galileo board to produce a high frequency output makes its unfeasible for our purposes. Unfortunately, I was unable to explore other boards before the end of the summer research program. The requirements of an MCU for our purposes are the following:

- high speed communication bridge between processor and I/O pins (update rate of at least 0.025 ms) OR
- the ability to generate interrupts at 40 kHz

V. Discussion and Conclusion

In the 10-week span of the research program, we managed to produce a working MATLAB simulation of the signal processing blocks. The model's results are very similar to the results of the prototype that we have. Coding a working algorithm for some of the blocks in MATLAB would also make the microcontroller implementation in C easier. Most parameters of the system, such as the bandpass frequency, or pulse wave frequency, are input variables in the model, making the testing of parameters easy.

However, one essential part of the model that is still missing is the demodulation of the signal to the audible range as it passes through nonlinearities. Nonlinear acoustics is a mathematically rich subject, requiring a firm grasp of its theoretical principles before its simulation. There is a lot of research on it that we could study to understand it further.

When the warning system has been implemented onto a microcontroller, the potential for the directional speakers is far reaching. For our project, we could then plan on mounting it on a bus. Since all the processing is on a microcontroller, it would be portable and easy to configure. On a broader level, there could be use for our system in other areas where directional sound is desired, such as an audio guide installed on pedestrian traffic lights to guide the blind, a directed honk for cars, or even a directed warning for animals on train tracks, given that they can hear ultrasonic frequencies too. A robust directional speaker implemented onto a microcontroller would motivate new ways of thinking about sound.

ACKNOWLEDGMENTS

I would like to thank Dr. Jan Van der Spiegel for the opportunity to experience research at Penn and Linda Kalb for coordinating the program.

I am grateful to my advisor, Dr. Daniel Lee for his motivation and advice, both on specific points of the project and on engineering as a whole. He gave me a bigger picture on engineering research by exposing me to his other students' research. I also appreciate the guidance from my graduate mentor, Alex Burka. He provided useful technical advice and gave me the opportunity to work on significant parts of the project. Finally, I thank Justin Aird, my research partner for supporting me with valuable ideas when I ran into problems and providing a lively environment in the lab.

REFERENCES

[1] Pennsylvania Department of Transportation, "2013 Pennsylvania Crash Facts and Statistics," 2013.

[2] O. Fleming, "SEPTA, Union In Dispute Over 'Death Mirrors.'"[Online]. Available: http://www.myfoxphilly.com/story/18901643/septa-union-in-dispute-over-death-mirrors. [Accessed: 26-Jun-2014].

[3] D. C. Schwebel, D. Stavrinos, K. W. Byington, T. Davis, E. E. O'Neal, and D. de Jong, "Distraction and pedestrian safety: how talking on the phone, texting, and listening to music impact crossing the street.," *Accid. Anal. Prev.*, vol. 45, pp. 266–71, Mar. 2012.

[4] K. Farkas, "RTA to install an audible system on buses to warn pedestrians at crosswalks." [Online]. Available: http://blog.cleveland.com/metro/2009/10/rta_to_install_an_audible_syst.html. [Accessed: 26-Jun-2014].

[5] F. J. Pompei, "Sound From Ultrasound : The Parametric Array as an Audible Sound Source," Massachusetts Institute of Technology, 2002.

[6] F. J. Pompei and S.-C. Wooh, "Phased array element shapes for suppressing grating lobes," *J. Acoust. Soc. Am.*, vol. 111, no. 5, p. 2040, 2002.

[7] P. J. Westervelt, "Parametric Acoustic Array," *J. Acoust. Soc. Am.*, vol. 35, no. 4, pp. 535–537, 1962.

[8] R. Haberkern, "Soundlazer Circuit Schematic." http://www.soundlazer.com/?page_id=7308, 2012.

[9] Analog Devices, "SigmaDSP 28-/56-Bit Audio Processor with Two ADCs and Four DACs." ADAU1701 Datasheet, Last Updated Mar. 2013.

[10] Texas Instruments, "TL494 Pulse-Width-Modulation Control Circuits." TL494 Datasheet, Jan. 1983 [Revised Jan. 2014].

[11] Cypress, "20-, 40-, and 60-Bit I/O Expander with EEPROM." CY8C9520A CY8C9540A, CY8C9560A Datasheet [Revised Sept. 2011].

Decentralized Autonomous Multi-Robot Communication Systems

Golden Rockefeller

Professor Camillo J. Taylor

University Information

Abstract

Coordinating many robots to do a task can, in many cases, be better than sending out a single robot to do it. However, different approaches in how the robots communicate under certain constraints are expected to have varying results. Our goal is to come up with different approaches and compare them with one another in the case of exploration. We also compared systems with no communication to those with decentralized communication to those with the more ideal, centralized communication. We simulated multiple robots interacting with each other in a grid-like world given the task to explore. The robots had a communication constraint that required them to be on the same grid to exchange information. We came up with the queen-ant system with robots occasionally returning to the home base to deposit and receive information about the world. We expect that this system will perform better than systems where the robots do not provoke communication and the transfer of information. The tests show that efficient rather than frequent communication in a multi-robot system will lead to more productivity.

Introduction

Multi-robot systems involve some amount of relatively simple autonomous robots coordinating with each other in ways that allow them to achieve greater tasks with a success than a single robot can. Mutli-robot are also less likely to fail at a given task when individual robots malfunction. Such systems can be ideal approaches to tasks that include and are related to exploration and coverage, search and rescue, and coordinated construction. However, potential limitations and problems exist in the real world that can lessen the effectiveness or plausibility of such systems, such as imperfect sensor data and communication signal interferences. Decentralized systems are attractive because there is often a lack of time, resources, or an ideal environment to set up a reliable centralized system to guide active robots. It is therefore the purpose of this study to simulate and evaluate the effectiveness of various implementations of decentralized systems. The system will have autonomous robots collaborating with one another under certain communication constraints in order to carry out tasks in a field that is initially unknown to them.

We plan to simulate ant-like robots exploring an unknown grid-like world coming from their home on the perimeter of the world. The simulation will be programmed and executed in MATLAB, because of the software's object oriented and graphic features. Success is measured by the number of time-steps the robot took to complete a task or by milestone. Different approaches in robot behavior will be explored and compared in how they handle different tasks, environments, and constraints. The effectiveness of each approach for a given task will most likely be affected by communication constraints. We suspect that centralized communication will be more ideal because each robot will always have an accurate view of the world, where decentralized systems will leave a great amount of uncertainty. It is also our goal to see how best to deal with inaccuracies and uncertainty and how these factors may determine which robot behavior is more capable for a given situation.

We plan to simulate a variety of scenarios that features robots with certain sensing and communication constraints. One goal may be to simulate robots coming from an origin location at the perimeter and exploring a field that is initially unknown to them. Any cell in this field would either be unobstructed or obstructed. The robots can only sense the eight cells around, and can only move to an unoccupied cell. Robots keep track of its own version of the map with representations of cells that are either occupied, unknown, or clear. They can update this map by exploring and sensing their environments or by communicating with other robots. If they choose to communicate, the communicating robots merge their versions of the map. Robots also keep track of where other robots are. The constraint for communication is that robots must be on the same position to exchange information.

Background

There are many existing algorithms and plans on multi-robot exploration. Possible approaches include different robot behaviors such as exploring by moving randomly, or exploring while moving away from other robots [1]. Morlok and Gini concluded that robots can spread out better when they have an idea of where close-by robots are. In a related piece, one might use the robots' zones of signal intensities to disperse robots. [2]. Robots may also explore efficiently by continuously moving to the closest unexplored location. This behavior will require the use of the depth-first search algorithm in combination with Dijkstra's_algorithm using a distance map [3]. Robots can also build communication networks. For example, a robot who wishes to relay information to others may stay in a location where it is most likely going to come in communication range of another robot [4].

Experiment and Simulation

We will create a 100 by 100 grid field with randomly placed obstacles. 10 robots starting from the top-left corner are tasked to explore the field. The simulation ends when all robots have explored the field. The robots can only sense the eight cells around it and use the information to build a map of the world for themselves. It can also move to any unoccupied cell around it. The robots may share information by communicating in which they both update the map using the information from the other's map. The criteria for communication is that the robots involved must be on the same cell. This simulation was created and executed in MATLAB.

The robots may behave differently depending on the system. As such, we are testing three different systems: No Communication, Simple or Opportunistic Communication, Provoked Communication, Queen based communication, and Centralized Communication. In the No Communication system, the robots do not exchange any information. In the Simple Communications system, the robots may communicate should they happen to occupy the same cell by chance. In the Provoked Communication system, robots may instigate information exchange with a sensed nearby robot should it believe it has some to share. Queen based Communication works by having robots go out and retrieve data. The robots can then decide to either use time to explore the world or return and communicate with the queen increasing the queen's knowledge as well as its own. The robot chooses to return if it believes that the queen has some information to offer it, and that information will be greater than what the robot should receive if it wastes the same amount of energy exploring. The amount of information the robot expects from the queen can be varied and used to control the rate of communication, like a tolerance. Queen15, Queen25, Queen30, Queen35, Queen40 are Queen based systems with various tolerances. Centralized communication is when the robot knows everything the other robot knows at every timestep. This is the idea case and is expected to outperform the others.

The simulation runs as follows:

Create Field

```
Create Robots
Initialize measurement variables
Set Timestep to 0
While Robots have not explored all cells
    For each Robot
        If Robots can communicate
            Robots communicate
        End
    End
    For each Robot
        Move somewhere depending on system implemented
        Case System Implemented:
            No Communication or Simple Communication:
                Move one cell towards closest unexplored cell.
            Provoked Communication:
                If near a Robot that it hasn't communicated with for some time
                    Move that Robot's cell to communicate
                Else
                    Move one cell towards closest unexplored cell.
                End
            End
        End
    End
    Increment Timestep by 1
    For each Robot
        Sense surroundings and update Map
    End
    Collect and Process Measurement data.
```

Results and Analysis.

The amount of time that the robots took for all to have complete knowledge of the field measured the success of the various systems. The better system is the one that uses less time to complete the task. We also calculated how many times the robots communicated until the end of the simulation in order to find the connection between communication and performance.

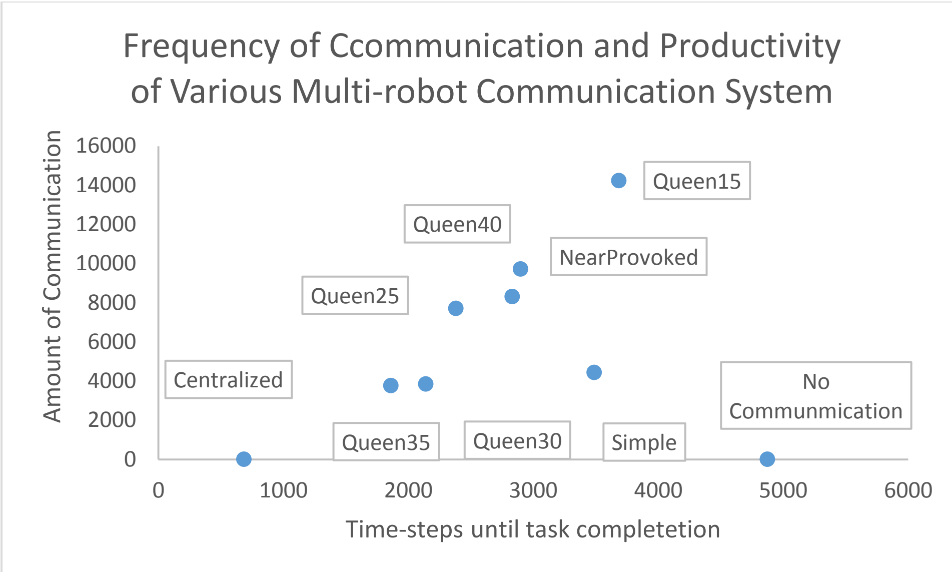

Figure 1 Results on the outcomes of various multi-robot communication systems. Systems towards the left are more ideal as they take less time to complete a task.

Conclusion

From the results we can confirm that the use of multiple communicating robots does aid in the task of exploration. We can see here that the Centralized Communication system was the most effective for exploration which was to be expected. Nonetheless, all decentralized systems did much better than the robots that did not communicating, the best of these systems is the Queen Based systems. However, it is important to note that though 10 robots collaborating is better than 10 that are not, the benefits are not 10 times better. What this means is that there is some overlap in the robots activities. An uninformed robot may explore regions that other robots have already explored. This adds inefficiency to the performance of the system and explains why the sum of the robots' maps have much more information that the average robot map. Such a problem will not exist in an ideal centralized system where robots are always informed. The Queen35 system was the best of the queen based systems because it had a perfect balance between communication and exploration. The robots returned to the queen at crucial times to lessen the overlap in their activities by learning about what has already been done.

Looking forward, systems that either promote more and frequent communication or prevent robot overlap should be experimented with. Additionally, these systems should be executed and analyzed when robots are doing other tasks such as search and rescue and collaborative construction. It will also be interesting to see how flexible these systems are and to see what effects robot malfunction can have on the effectiveness of the system.

Acknowledgments

References

[1] R. Morlok and M. Gini. “Dispersing robots in an unknown environment” 2004 Available: http://www-users.cs.umn.edu/~gini/papers/Morlok04dars.pdf

[2] S. Damer , L. Ludwig , M. A. LaPoint , M. Gini , N. Papanikolopoulos , and J. Budenske. “Dispersion and exploration algorithms for robots in unknown environments” Available: http://www-users.cs.umn.edu/~gini/publications/papers/Damer06.pdf

[3] A. Zelinsky. “A Mobile Robot Exploration Algorithm”. *IEEE Transactions On Robotics And Automation, VOL. 8, NO. 6,* December 1992. Available: http://ieeexplore.ieee.org/stamp/stamp.jsp?arnumber=00182671

[4] C. Amato, G. D. Konidaris1, G. Cruz, C. A. Maynor, J. P. How and L.P. Kaelbling. “Planning for Decentralized Control of Multiple Robots Under Uncertainty”. February, 2014. Available: http://arxiv.org/pdf/1402.2871v1.pdf

Simulating Electric Double Layer Capacitors

Abel Rodriguez, George Washington University, Biomedical Engineering, *SUNFEST Fellow*
Dr. Jorje J. Santiago-Aviles, University of Pennsylvania, Electrical Engineering

***Abstract*-It is vital to improve the energy storage of devices in order to better harness renewable energy and deliver it efficiently to essential electronics. In order to fulfill this need, an electrical component must be developed that has higher energy storage than a traditional capacitor, greater power rating than a battery, and can last many charge and discharge cycles. High surface area electric double layer capacitors (EDLC) have been developed, and appear to be able, to fill this void by storing charge in a layer of ions along the surface of electrodes. To optimize the performance of devices of this kind, we set out to run simulations where the limits of the device's charge storing capabilities can be explored using COMSOL, a finite element modeling software tool. The results indicate that the simulation is indeed able to replicate physical findings, meaning it is an appropriate method to predict results given parameters of an EDLC. The simulation profile can be used as a tool to strengthen experimental research, predict EDLC properties, and optimize their configuration for certain tasks. The next steps would be to refine the simulation to better suit the specific application and also expanded upon it by considering new parameters such as heat dissipation, fluid flow, and physical stresses.**

***Index Terms*- Analog Circuits, Application Virtualization, Capacitors, Computer simulation, Energy storage, Partial Differential Equations, Physics Computing, Supercapacitors.**

I INTRODUCTION

Energy is the promoter of great innovation. Without an intelligent way to power electrical devices, the advancements of renewable energy will be all for naught. It is very difficult to ignore this need for energy storing devices, and as such, a solution must be found. The supercapacitor is an energy storage component that mimics faradaic capacitor properties by using electrochemical redox reactions or an electrolyte double layer. These pseudo capacitors have a very high power density, and so, they charge and discharge at much faster rates than batteries. To allow for other technologies such as wearable electronics, electric motor vehicles, and renewable energy to advance, supercapacitors must be improved upon [1].

Available Performance	Lead Acid Battery	Supercapacitor (EDLC)	Conventional capacitor
Charge Time	1 to 5 hrs	0.3 to 30 s	10^{-3} to 10^{-6} s
Discharge time	0.3 to 3 hrs	0.3 to 30 s	10^{-3} to 10^{-6} s
Energy (Wh/kg)	10 to 100	1 to 10	< 0.1
Cycle life	1,000	> 500,000	> 500,000
Specific Power (W/kg)	< 1000	< 10,000	< 100,000
Charge/discharge efficiency	.7 to .85	0.85 to 0.98	> .95

Table 1: The differences between batteries, capacitors, and EDLCs [3].

In the last ten years, there has been a drastic increase in the need for a new level of energy storage devices. Portable technologies continue to have a great impact on consumer technologies, implantable medical devices, and mass power generation. These changes have put pressure on researchers to find adequate technologies to deliver to those in need. It becomes obvious that there are advantages to using EDLCs (Table 1). These advantages must then be improved upon to fill the need. From this pressure stems the desire to develop a study of the limits of the properties of these electrochemical pseudo capacitors. I hypothesize that with the ease of computational theoretical studies using COMSOL, versus actual experimentation, one can not only find more refined methods for current supercapacitor geometry, but also test very different approaches to the same problem [2] . In conjunction with researchers, one can focus on bringing this newly found geometry to a lab where it can be tested.

For the field of electronics it is vital to design a simulation platform that can predict the phenomena that operate within a supercapacitor. The study of supercapacitors is of great interest because of its power advantage over batteries and energy advantage over conventional capacitors (Table 1) [3]. The theoretical knowledge that is to be gained from the simulations ought to yield ideas for further research in the field of supercapacitors. Although many researchers have studied it, this particular attempt to review the physical phenomena through computation may advance the field. With the experience I have in electronics from my undergraduate training, along with the guidance of the Santiago research group at the University of

Pennsylvania, I aim to design and test supercapacitor models using COMSOL.

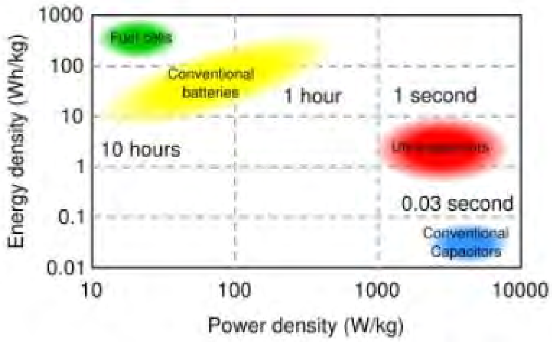

Figure 1: Ragone plot of Energy Density vs. Power Density of different energy storing devices [3].

II BACKGROUND

COMSOL is software that uses finite element modeling, a mathematical approach to solving boundary problems, and multiple physics equations to model physical phenomena such as heat flow, material stress, or in this case electrostatic properties [4]. This software is widely used, and has been referenced in many academic papers. The simulation space is used by inserting geometric materials into a space with a set study to be performed such as electrostatics, electric currents, or Partial differential equations. It uses a mesh to constitute the size of the individual places to which the computations occur. As the regions are smaller, the results are more precise but take longer to compute. This software will be heavily used to model supercapacitors in the pursuit to learn more about their behavior.

The Physics behind the EDLC begins with a Helmholtz layer which is a layer of oppositely charged ions on the surface of an electrode. The Gouy-Chapman model introduced a diffuse layer that better resembled the actual phenomena, in 1910. A stern model then combined the theories as ions in a diffuse layer further away from the electrode then the Helmholtz layer [5].

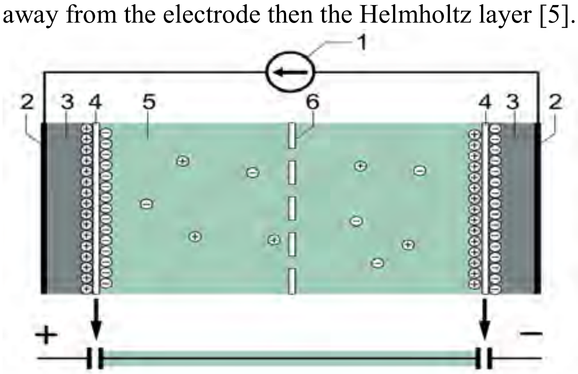

Figure 2: Schematic of an electric double layer capacitor. 1-power source, 2-current collector, 3-electrode, 4-helmholtz double layer, 5-electrolyte, 6-separator.

The research follows a design where the most basic of capacitor geometry are built and analyzed on the computational suite. After the simplest of designs have been supported, they are designed with further complexities to gain more and more insight into their functionality. Characteristics such as power, energy, voltage limit, and faradaic capacitance will be compiled. The first attempts are basic capacitors with common materials. Then electric double layer capacitors will be simulated. There is very little known on the topic when it comes to COMSOL simulation of these porous carbon membranes, which outlines the novelty of this work. I will use a linear approach increasing the complexity by combining distinct materials, geometries, and auxiliary components. The limitation of this research is the possible inability to confirm results experimentally due to the rigid structure of the simulation versus practical physical limitations. For example, in a simulation one is able to place structures exact distances apart whereas in experiments one can only assume that the procedure results in similar placement. This research does not offer a solution to the practical problems limiting the experimental creation of such devices, but rather simplifying the procedure of making aforementioned devices using different materials via simulation.

III METHODS

In order to complete the goal of simulating the physics behind an electrical double layer capacitor (EDLC) a simpler problem must first be solved. Using the methodology of Occam’s razor a very simple design was approached before ever attempting an EDLC model. This began with using COMSOL’s basic materials, physics models, and tools to simulate known physical phenomena in the form of a two-dimensional parallel plate capacitor. In this simple model a very close relationship was observed between the distance between the plates, their surface area, and the capacitance. The relationship followed the formula

$$C = \varepsilon_r \frac{A}{4\pi d} \quad [6]$$

C in the formula is for the capacitance of the device in question. ε_r is the permittivity of the substance between the plates. A is the area of the plates and d is the distance between the plates. Given this equation, one can see that the results of the simulation match that of the theoretical result. The model was then made more complex by making three-dimensional models with the same physics. Lastly time variant analysis was performed to measure the charge and discharge of the capacitor in a circuit model rather than a stand-alone element.

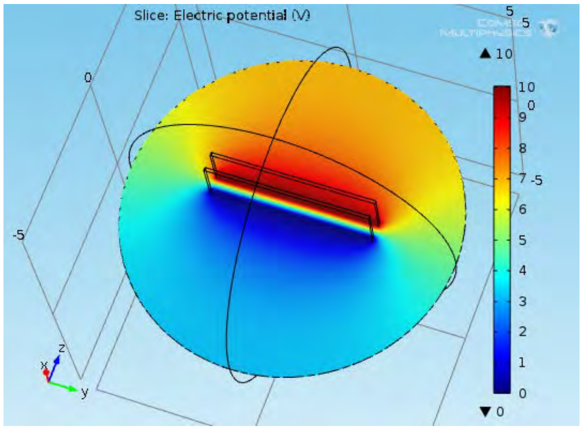

Figure 3: COMSOL slice of voltage gradient along an axis of a parallel plate capacitor.

After completing the simulations with standard capacitor models (Figure 3) it was time to complicate the physics and move onto EDLC simulations (Figure 4).

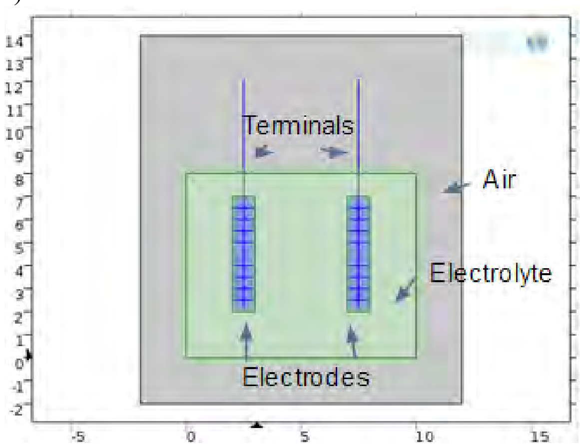

Figure 4: COMSOL simulation geometry for a 2D EDLC.

The most important difference between an EDLC and a common capacitor is the role of the ions adsorbing to the material to store charge. The variables become more complex as more and more parameters are introduced such as material porosity, concentration of electrolyte, and ionization of the electrolyte [7]. Mathematical solutions needed to be found of the diffusive properties of the electrolyte, in order to assure the model was measuring the charge storage of the molecules on the surface of the electrodes, rather than the capacitance between the two electrodes.

IV RESULTS

The resulting simulation model yielded promising charge storing properties. There was a small change in the capacitance with the movement of the electrodes as expected. The three-dimensional model was completed and provided strong correlation to other models in the literature. Considering that one is unable to fully observe the placement of the individual ions on the surface of the electrode the particular charge storing mechanism is yet to be fully validated.

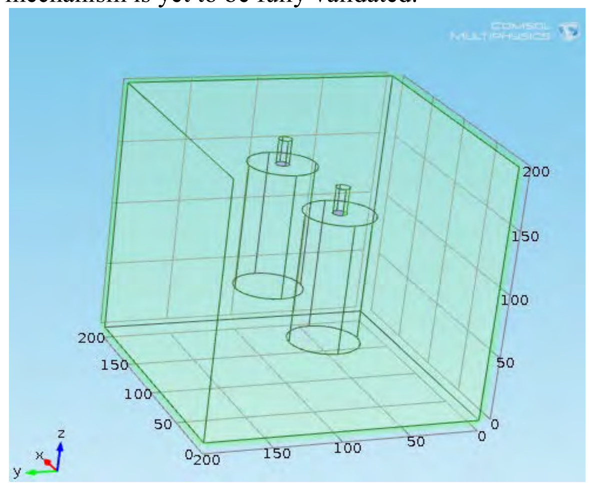

Figure 5: COMSOL simulation of the 3D geometry used for the EDLC simulation.

The final simulation shown (Figure 5) is an image of where the simulation geometry is currently standing. The two terminals are shown along with the electrodes made of a carbonaceous material and surrounded by an organic compound. The specific parameters associated with the materials in question are always being changed in order to fit the need of the tests run.

V CONCLUSION

Further solidification of the model is necessary to be certain of the charge storing mechanism. This can be achieved by continuing to monitor the changes of the system in reference to the standard capacitance model versus the diffusive model. When this occurs the model will be better validated and ready for comparison with experimental results. With the findings that have been gathered, one can begin to formulate ideas as to how to optimize said system and begin to develop a plan for physical construction of said element. Other geometries will also be explored to possibly better suit the demands of the research. The EDLC model will continue to be studied with hopes of both validating experimental findings and setting a premise for future experimentation.

VI ACKNOWLEDGEMENTS

This work was supported by the National Science Foundation and the University of Pennsylvania's Summer Undergraduate Fellowship in Sensor Technologies. With the great practical help of Timothy

Jones, Dr. Carlos Perez, and Dr. Jorje J. Santiago-Aviles. Special thanks to those who aided this research indirectly such as Linda Kalb, Joshua Taton, Jessica A. Leon, and Vinicious Ferreria. To those mentioned here and all who helped, thank you.

VII REFERENCES

[1] P. Simon, Y. Gogotsi,"Materials for electrochemical capacitors," Nature materials, vol. 7, pp. 845-847, Macmillan Publishers, Nov. 2008.
[2] G. Madabattula, S. Gupta. "Modeling of Supercapacitor" Excerpt of 2012 COMSOL conference in Bangalore.
[3] Tecate Group "ultracapacitors-supercapacitors" Webpage, http://www.tecategroup.com/ultracapacitors-supercapacitors/ultracapacitor-FAQ.php
[4] E. Mohamad, M. Mohamed, "Sensor Modeling for Portable Electrical Capacitance Tomography System Using Simulation By COMSOL Multiphysics", International Journal of Innovative Computing Information and Control. Vol 8, Number 10(B) October 2012.
[5] Kun-Lin Yang, Sotira Yiacoumi, "Elecric double-layer formation", Georgia Institute of technology.
[6] "Parallel Plate Capacitor." Georgia State University, n.d. Web. 28 July 2014.
[7] Julian Varghese, Hainan Wang, and Laurent Pilon. "Simulating Electric Double Layer Capacitance of Mesoporous Electrodes with Cylindrical Pores." Journal of The Electrochemical Society, pg 158, 2011.

A Wireless, Real-Time Embedded System for Closed-Loop Myoelectric Control of Sedated Primates

Jacob Sacks (The University of Texas at Austin, Biomedical Engineering), *SUNFEST Fellow*
Dr. Jan Van der Spiegel, Electrical and Systems Engineering

***Abstract*—Brain-computer interface (BCI) technology establishes a direct link between the nervous system and external hardware. An important application of such devices is myoelectric control, or the use of the electrical potential generated during muscle contraction as an input signal. This physiological information is heavily used in rehabilitation engineering and novel human-machine interaction. Current commercial systems are limited in their degrees of freedom for control, and are incapable of bidirectional communication with the nervous system. Such restrictions prevent intuitive use of myoelectric devices and closed-loop control with sensory information. This paper presents a microcontroller-based, wireless BCI system that recognizes simple hand gestures as input and produces a corresponding output signal. Surface electromyography (sEMG) is used to capture the myoelectric signals (MES) on the neural recording device, and a simple classification scheme produced offline by a supervised machine learning algorithm identifies each gesture. This allows for a continuous stream of gesture classification decisions within acceptable response time. A wireless link is implemented to directly output gesture decisions to external devices. Remarkably, the simple classifier employed on the microcontroller paired with the right signal features allows for gesture recognition within acceptable accuracy. Future studies will include communication between the analyzer and stimulator to allow for animal trials. In addition, more intelligent classifier algorithms will be coupled with additional sEMG channels to further increase recognition accuracy and include more gesture commands.**

***Index Terms*—Brain-computer interface, classification, data acquisition, electromyography, embedded system, feature extraction, hand gesture recognition, machine learning, myoelectric control, pattern recognition, real-time systems, surface electrodes, user intent recognition.**

I. Introduction

Myoelectric control of peripheral hardware is an expanding field which involves the conversion of neuromuscular activity into command signals for external devices. In particular, it has many applications in rehabilitation engineering, from controlling prosthetic limbs to human-assisting robots. While most commercial prosthetics use inconvenient body-powered mechanical control schemes, myoelectric systems are non-invasive and allow for hands-free control that follow a user's intent. The simplest myoelectric systems use an on-off control scheme with a single speed [1]. Some devices are level or rate coded, which means they estimate the amplitude or rate of change of the myoelectric signals (MES) to control actuation [2]. More complex systems incorporate a finite state machine with control proportional to signal intensity to carry out complex tasks [1]. However, all of these methods are unintuitive and involve a large amount of user training.

Current research utilizes pattern recognition algorithms to determine accurately the action intended by amputees or performed by able-bodied users [1]. Studies have shown that amputees are able to generate repeatable myoelectric signals (MES) during both static and dynamic contraction [1]. The information present in these residual neuromuscular pathways can be captured and artificially linked to external hardware and separate neural circuits. Similarly, able-bodied users can sample their fully intact MES during muscle contraction. Most of these systems use a dedicated computer, while those employed on an embedded system are generally wired. This constrains the system design and potential applications of the device.

To realize myoelectric control suitable for prosthetic applications, there are three important criteria to which researchers must adhere: the accuracy of movement selection, intuition of the control scheme, and the response time [1]. There is no established threshold for acceptability due to a lack of clinical trials. Accuracy is generally improved upon by extracting more information from muscles, utilizing more advanced pattern recognition algorithms, and increasing the number of muscles analyzed. An intuitive interface is one that decreases the amount of required training for the user. This is generally done by selecting natural muscle patterns as command signals, and developing a device that is adaptable to varying conditions. With respect to response time, there should not be a perceivable delay in operation. The general threshold for acceptable delay is about 300 milliseconds [2].

This study develops a wireless, embedded myoelectric system that is capable of recognizing various hand gestures in real-time. The device is realized with the PennBMBI system [3], which contains a wireless neural signal analyzer, two neural stimulators, and a computer interface that enables easily modifiable sensorimotor control. Unlike most neural prosthesis systems, the PennBMBI is capable of reconnecting with the nervous system to restore or augment normal functionality. Its neural signal analyzer was configured to decode the surface electromyographic (sEMG) signal from a human subject using pattern recognition techniques. The aim of the study is to then use the gesture determined in the analyzer to uniquely stimulate muscle in a sedated, non-human primate. This would demonstrate how artificial sensory information could be sent through the nervous system to help restore feeling in prosthetic devices, or even in previously severed neural pathways.

II. Background

A. Surface electromyography

The first step in the formation of a myoelectric control scheme is the collection of physiologically-relevant signals from the nervous system. Information on muscle activity is collected through electromyography (EMG), a technique which samples the electrical activity generated in skeletal muscles during contraction. It is dependent on the anatomical and physiological properties of muscle. Spikes in the output signal represent a summation of motor unit action potentials (MUAPs) created during the muscle contraction. Different gestures activate unique motor unit populations, resulting in distinctive patterns [4]. Unlike its invasive counterparts, sEMG is carried out by electrodes placed on the surface of the skin.

More information extracted from each sEMG channel increases the accuracy and degrees of freedom for control. To increase the amount of data, some researchers employ multichannel sEMG systems. This allows them to extract more localized information on a greater number of muscles. Since such an apparatus can be cumbersome, the preferred method is to utilize more efficient signal features. By carefully choosing the right parameters, complex sEMG signals can be broken down into their fundamental components. In this device, a single channel sEMG is used to extract muscle activity from the forearm. The signal acquires noise as it travels through the tissue, and must be appropriately amplified and filtered [5]. A differential amplifier filters noise and brings the input up to a level compatible with the analog-to-digital converter (ADC). The signal is converted to digital by the ADC and is captured by a microcontroller (MCU).

B. Pattern recognition

Pattern recognition algorithms involve three main steps: data segmentation, feature extraction, and classification. Data segmentation comprises of dividing the data into windows for analysis. Specifically, a moving window method was employed, meaning subsequent analysis windows were overlapped to provide more data and improve accuracy. Feature extraction involves computing a set of signal features for a given analysis window. A feature is defined as a quantifiable statistic that characterizes the nature of a signal. These features transform the complex input into a form capable of being analyzed. Choice of the signal features is a critical stage that affects both accuracy and response time.

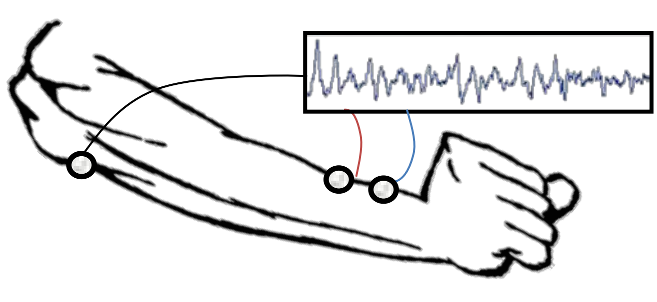

Fig. 1. Electrode placement on forearm during data collection and device testing

Classification divides the possible input into sets, and determines into which set an input resides. Each set is assigned a numerical representation that is output by the classifier once a decision is formed. Signal features are condensed into a vector and fed into the classifier algorithm to yield the class prediction. Supervised machine learning was employed, meaning the classifier must be trained with previously acquired data before it can be used to predict the gesture. Once trained, the classifier is fed features continuously extracted from the sEMG input to compute a decision for each window. Sometimes post-processing methods, such as majority voting, are implemented to eliminate jumps and smooth the output of the classifier. This generally must be done with real-time gesture recognition systems, because there is a lack of sensory feedback in most myoelectric devices.

III. System Design

A single channel analog front-end with a configurable pass-band, gain stage, and ADC was employed on the neural signal analyzer. An instrumentation amplifier was implemented on the board to help filter out noise. In this study, the pass-band was configured for 10 Hz to 1 kHz. The 16-bit ADC performed sampling at 5 kHz, though the lower byte is discarded in software. This was done because future implementations will include an 8-bit ADC, and the majority of the information is contained in the most significant byte. The device was powered up by rechargeable 950 mAh 3.7 V lithium-ion batteries.

Values from the ADC were then fed to an Atmel ATxmega128A4U 16-bit MCU, where neural feature extraction and classification was realized in the central processing unit (CPU). Its processor ran at 32 MHz, providing plenty of processing power for feature extraction and the potential addition of multiple channels. All MCU software was written in Atmel Studio and uses the Atmel Software Framework (ASF). The AVRISP mkII and AVR Dragon programmers were used to flash the program to the MCU through a PDI interface.

A SPI module facilitated communication with a RF transceiver from the MCU for data transfer between the computer and analyzer, as well as communication with the stimulator. The RF transceiver used was the NRF24L01 from Nordic Semiconductor, which features a maximum on-air data rate of 2 Mbps and runs in the 2.4 GHz frequency range. A PC interface containing a separate MCU and RF transceiver is connected to the PC through USB, and is used to receive data

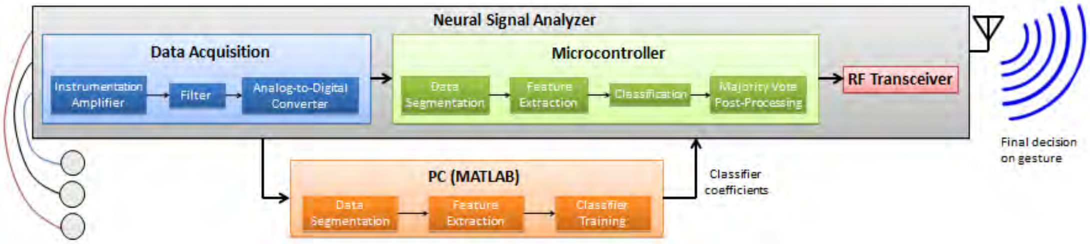

Fig. 2. System design for data acquisition, feature extraction, gesture classification, and decision output

from the analyzer. During training, the device transferred all data directly to the computer, which was easily visualized and stored using a MATLAB-based graphical user interface (GUI). For real-time testing, only the final decision was output from the device. The entire experimental setup can be seen in Fig. 2.

IV. Pattern Recognition Algorithm

A. Feature extraction

Several types of features have been used for myoelectric classification: time domain (TD), frequency domain (FD), and time-frequency domain (TFD). Frequency and time-frequency features have been shown to accurately predicate transient signals [1]. However, since the gestures in this study are held and classification occurs primarily at steady-state, there is no real advantage to using them. Time domain features were chosen because of their simplicity and lower computational cost.

Eight time-domain features were chosen: mean absolute value (MAV), root mean squared (RMS), number of zero crossings (ZCs), number of slope sign changes (SSCs), the waveform length (WL), and the third-order autoregressive (AR) coefficients. The MAV, RMS, and WL are defined as such:

$$MAV = \frac{1}{L}\sum_{i=1}^{L}|x_i - \mu| \tag{1}$$

$$RMS = \frac{1}{L}\sum_{i=1}^{L}(x_i - \mu)^2 \tag{2}$$

$$WL = \frac{1}{L}\sum_{i=1}^{L}|x_i - x_{i-1}| \tag{3}$$

Here μ is the mean of the data, L is the window length, and x_i is the sampled data at point i. The number of zero crossings is a measure of frequency obtained by counting the number of times the data crosses zero within a given threshold. This threshold is applied to reduce the effect of noise on the statistic. A zero crossing is said to occur if given two points,

$$(x_i > 0 \; and \; x_{i+1} < 0) \; or \; (x_i < 0 \; and \; x_{i+1} > 0) \tag{4}$$

and

$$|x_i - x_{i+1}| \geq \varepsilon \tag{5}$$

Here ε is the threshold applied to help filter out the influence of noise. The second measure of frequency used is the SSC count, which is said to occur if

$$(x_i > x_{i-1} \; and \; x_i > x_{i+1}) \; or \; (x_i < x_{i-1} \; and \; x_i < x_{i+1}) \tag{6}$$

and

$$|x_i - x_{i+1}| \geq \varepsilon \; or \; |x_i - x_{i-1}| \geq \varepsilon \tag{7}$$

An AR process is defined as

$$x_{i+1} = \varphi_1 x_i + \varphi_2 x_{i-1} + \cdots + \varphi_p x_{i-p+1} + \epsilon_{i+1} \tag{8}$$

where p is the order of the process, φ_i is the ith autoregressive coefficient, and ϵ is Gaussian white noise. While there are multiple methods for approximating the coefficients, the chosen method is to solve the Yule-Walker equations. These equations can be condensed into a matrix equation and solved by

$$\begin{bmatrix} \varphi_1 \\ \varphi_2 \\ \vdots \\ \varphi_p \end{bmatrix} = \begin{bmatrix} r_0 & r_1 & \cdots & r_{p-1} \\ r_1 & r_0 & \cdots & r_{p-2} \\ \vdots & \vdots & \vdots & \vdots \\ r_{p-1} & r_{p-2} & \cdots & r_0 \end{bmatrix}^{-1} \begin{bmatrix} r_1 \\ r_2 \\ \vdots \\ r_p \end{bmatrix} \tag{9}$$

Here r_i is the normalized autocovarience of the input signal for a lag of i. In software, this equation is solved by Gaussian elimination.

During training, the prerecorded EMG signal data was segmented into a series of fixed length, overlapping analysis windows. In each analysis window, the eight TD were extracted and condensed into a 9 x 1 feature vector $\bar{f}$. A moving window method of analysis was used, because it allows for efficient use of the MCU processing power, and provides semi-redundant data to help minimize classification error. The additional entry in each vector was a single one, which allows the classifier to introduce a constant term. These vectors were then used to form a 12 x M feature matrix, where M is the total number of training windows used for all gestures. The layout of this matrix is shown below:

$$\begin{bmatrix} f_{0,0} & f_{0,1} & \cdots & f_{0,12} \\ f_{1,0} & f_{1,1} & \cdots & f_{1,12} \\ \vdots & \vdots & \vdots & \vdots \\ f_{M,0} & f_{M,1} & \cdots & f_{M,12} \end{bmatrix} \tag{10}$$

Fig. 3. Gestures the classifier was trained to recognize

In the testing phase, each feature has one or more continuously updated variables containing a sum or necessary statistic used in a later calculation. This alternative method of feature extraction is performed to minimize the use of inefficient loops and excessive RAM access. However, the use of a moving window means adjacent windows overlap, and not all data can be thrown away after classification. To compensate, the shift length of the moving window is fixed, and each running statistic is buffered into an array of size equal to the number of shift lengths in a window plus one. Thus, each entry corresponds to a particular block of data in which all features are computed. When a new block of data becomes available, it is encompassed by the window, and the first block from the previous window is discarded. Statistics from each block are combined appropriately to form the desired features for the entire window.

B. *Pattern classification*

Various classification algorithms have been applied to EMG signals: neural networks, a form of artificial intelligence found in machine learning, fuzzy logic systems, which utilized variables with truth values that range between true and false, and probabilistic methods, such as linear discriminate analysis (LDA) and expectation maximization (EM) [1]. In this study, a linear classifier is used to keep the algorithm simple and capable of being implemented on an MCU.

The classification decision is made from a linear combination of the features weighted by coefficients determined during training. Linear regression is performed on the feature matrix (10), along with a vector containing the true gestures for each row, to provide the weights for each feature. During testing, the combined features for a given window are fed into the trained classifier by applying these coefficients as weights to each term. The overall sum is rounded to the nearest integer and serves as the decision for that particular window.

A majority vote post-processing method is also implemented, meaning each decision functions as a vote for the correct output. An array of size m holds each decision from the classifier, where m is the number of votes to consider. Once this array is filled, its mode serves as the final decision for the given gesture. The array is then emptied and the procedure repeated. This helps smooth the output from the classifier, and increase accuracy for smaller window sizes and less descriptive features.

V. Experimental Procedures

A. *Training data collection*

Four different hand gestures (Fig. 3) were recorded over a span of five seconds: a resting first, index finger extension, pinky extension, and a combination of the two extensions. Each gesture was performed twenty times, giving a total of one hundred seconds of data per gesture. These particular gestures were chosen, because previous experimental studies have shown high classification accuracy for wrist and finger extension motions [7]. During classification, each gesture was assigned a unique numerical value. The resting fist had a value of 0, index finger extension a value of 1, pinky extension a value of 2, and the combined gesture a value of 3.

Electrodes were placed on the upper forearm in locations known to be sensitive to digit extension (Fig. 1). The reference electrode was placed on the bony part of the elbow. Types of single-finger motion are more easily distinguished than multi-finger gestures, so the number of complex finger gestures was limited. Other digits were not selected, because of the similarities between the signals they produce. Both the index and middle finger, as well as the ring finger and pinky, yield similar features, making these pairs poor candidates. The index finger and pinky produced the most dissimilar response, improving the chances for their unique classification.

B. *Accuracy optimization testing*

K-fold cross-validation was used to determine the overall classification error from the training data. This algorithm partitions the data into k subsets, and classifier training is performed on all but one of these subsets. The leftover set is used to test the trained classifier and determine the prediction error. This procedure is then repeated for different partitions, and the validation results are averaged together. The resulting statistic was used to assess the accuracy of the classifier trained with specific features and generalize this performance to an independent data set.

To determine which window sizes and combinations of features would provide the most accuracy, cross-validation were performed under various conditions to yield the situation minimizing classification error. This simulation was performed in MATLAB, and then these scenarios were employed on the microprocessor and tested experimentally. For each window size and feature combination, one hundred classifier decisions were acquired and used to determine accuracy. The groupings were as follows: all features, all features except AR coefficients, the optimized feature set with AR coefficients, and the optimized feature set without AR coefficients. These conditions were repeated for the following window sizes: 32, 64, 128, 256, 512, and 1024 ms. The best performing combinations for each window size were then tested along with the use of majority vote post-processing. In addition, the power usage and feature extraction delay for each scenario was recorded.

VI. RESULTS

Average power consumption of the device was found to be about 80 mW, which corresponds to a battery life of about 35 hours. The average feature extraction time was 45 μs per sample. Table 1 shows the list of features selected by the validation error minimization when both autoregressive were included and left out. Window sizes larger than the acceptable delay of 300 ms were tested to determine the tradeoff in accuracy when size is decreased. According to the validation error (Fig. 4a), the best window size within an acceptable delay was 256 ms, with a best case error of 20.64%. With respect to experimental error (Fig. 4b), the 256 ms window size was only most accurate for the case without AR coefficients and when majority voting was used, providing a best case error of 5.5%. Overall, the best error was with a window size of 1024 ms, but this size is well over the acceptable delay threshold.

Table 1. Optimized feature list for different window sizes, both with and without autoregressive coefficients

Window Size	Optimized Feature List (With AR)	Optimized Feature List (Without AR)
32	MAV, RMS, ZC, SSC	MAV
64	MAV, RMS, ZC, SSC, Constant	MAV, ZC
128	All	MAV, RMS, ZC
256	ZC, SSC, WL, Constant	MAV, ZC, SSC, Constant
512	ZC, SSC, WL, Constant	RMS, ZC, SSC, Constant
1024	RMS, ZC, SSC, Constant	RMS, ZC, SSC, Constant

a)

b)

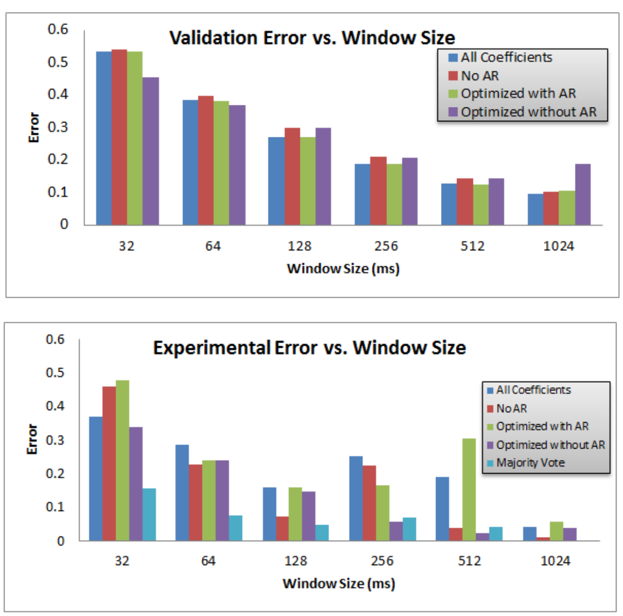

Fig. 4. a) Validation and b) experimental error found for the different window sizes and feature combinations

VII. DISCUSSION AND CONCLUSION

As expected, the validation error increased with a decreasing window size. Because there is less data from which to extract features, they are less representative of the gesture. There is more variance in the produced features, making the classifier more prone to error. Power usage remained fairly constant for different analysis window sizes. Since the computationally intensive part of feature extraction was calculating the running totals, which was done immediately after data acquisition, the delay remained uniform. This also circumvented the use of a buffer, meaning memory usage only changed when smaller window shifts were employed. Thus, the algorithm was both computationally efficient and minimized memory use.

Average experimental error was overall less than the validation error given the same scenarios. This can be attributed to the rounding mechanism employed during gesture classification. When the classifier produced a value greater than 3, the gesture output was still considered a combination gesture. Similarly, any gesture that produced a negative estimate was predicted to be a resting fist. Due to the placement of the electrodes, the system also seems to be highly sensitive to wrist movement. If the wrist is accidently elevated too high, the signal response will be stronger and classified greater or equal to a 3. Thus, if a combination gesture was simultaneously performed with a wrist extension, the gesture would almost always be predicted correctly. However, this does not occur when analyzing the training data, thereby increasing the validation error relative to the experimental error.

Another interesting discrepancy between validation and experimental error lies in the autoregressive coefficients. During validation, autoregressive coefficients consistently lowered error. However during testing, scenarios without these coefficients uniformly did better than their coefficient-bearing counterparts. This can most likely be attributed to the linear nature of the classifier. Not all coefficients followed a linear trend when increasing window size, indicating that linear regression is not the best choice of classifier. When pairing the nonlinear nature of the autoregressive coefficients with the sensitivity of the device to electrode placement, it is not surprising that they were not the best feature candidates.

Now that the neural analyzer has been implemented on the embedded system, the next step will be to alter the stimulator code to react appropriately to the decision output. Closed-loop communication between the two devices has already been achieved, but it needs to be modified to properly react to each individual gesture. Once this has been accomplished, the animal experiments with sedated primates can begin. A micro-electrode array will be implanted in the primate and connected to the stimulator, which will be capable of delivering various types of inputs. The gesture recognition system will send a continuous stream of decisions and dictate how the stimulator is to respond.

Using optimized settings and majority vote post-processing, classification accuracy was acceptable for many myoelectric control applications. However, the sensitivity of the system to setup suggests that much improvement must be made. A linear classifier, while hardware friendly, was too susceptible to slight variations in features and did not account for more complex relationships. Another important step in improving accuracy will be to employ multiple EMG channels. Since the sampling period is 2 ms, there is time to introduce more channels without affecting performance. While many improvements need to be made, this system demonstrates that wireless, embedded myoelectric control is feasible and practical.

ACKNOWLEDGMENT

The authors would like to acknowledge the support of the National Science Foundation, through NSF REU grant no. 1062672, as well as Linda Kalb and Joshua Taton for guiding the undergraduate researchers through the program.

REFERENCES

[1] M. Asghari Oskoei and H. Hu, "Myoelectric control systems—A survey," *Biomed. Signal Process. Control*, vol. 2, no. 4, pp. 275–294, Oct. 2007.

[2] K. Englehart and B. Hudgins, "A robust, real-time control scheme for multifunction myoelectric control," *IEEE Trans. Biomed. Eng.*, vol. 50, no. 7, pp. 848–854, Jul. 2003.

[3] L. Xilin, Zhang, Milin, Richardson, Andrew, Lucus, Timothy H., and Van der Spiegel, Jan, "The PennBMBI: a General Purpose Wireless Brain-Machine-Brain Interface System in Unrestrained Animals," *IEEE Int. Symp. Circuits Syst.*, 2014.

[4] D. A. Gabriel, S. M. Lester, S. A. Lenhardt, and E. D. J. Cambridge, "Analysis of surface EMG spike shape across different levels of isometric force," *J. Neurosci. Methods*, vol. 159, no. 1, pp. 146–152, Jan. 2007.

[5] G. R. Kanitz, C. Antfolk, C. Cipriani, F. Sebelius, and M. C. Carrozza, "Decoding of individuated finger movements using surface EMG and input optimization applying a genetic algorithm," in *2011 Annual International Conference of the IEEE Engineering in Medicine and Biology Society,EMBC*, 2011, pp. 1608–1611.

[6] X. Chen, X. Zhang, Z.-Y. Zhao, J.-H. Yang, V. Lantz, and K.-Q. Wang, "Multiple Hand Gesture Recognition Based on Surface EMG Signal," in *The 1st International Conference on Bioinformatics and Biomedical Engineering, 2007. ICBBE 2007*, 2007, pp. 506–509.

Creation of a Delta Leg Robot

Jordan White (Electrical Engineering, Hampton University), *SUNFEST Fellow*

Dan Koditschek, Avik De, and Gavin Kenneally, Robotics

***Abstract*—The problem is creating robot that can complete action similar to what humans can do is difficult. Currently what I am trying to do is develop a robot that can hop. The robot created was called the "Delta Hopper" which is a three-legged robot where all three legs are connecting to a base where it touches the ground. In this study after the robot was developed, the forward kinematics needed to be found, touchdown detection has to be calculated and detecting the bottom, which is when the robots legs are the most compressed. The result show that this robot it capable of hopping multiple times with the assistance of a "boon" which is just a device that helps the robot stands. The robot is not capable of hopping without a "boon" due to lack of information regarding the touchdown detection and finding where the legs are compressed the most. More time and research would be needed to get this robot to hop without any assistance.**

I. Introduction

The widespread use of robotics has increased over the years. These robots can be used for a variety of jobs, from surveying areas where it would be difficult for humans to look through, or just to do tasks that will make the human life easier. Many robots hope to perform task that humans can do, but humans are very complex. Reaching for an object on a table seems very simple for a human arm, but for a robotic arm it would require complex calculation to move the motors designed as the joints for the elbow and shoulder, to get to the desired point, as well as heat calculations.

Eventually there will be robots that can imitate what all life can do such as walking and hopping. All mammals, including humans, have multiple ways of completing the same task. A cockroach with six legs can walk normally over terrain similar to what a two-legged creature could do. Previous researchers from Nanyang Technological University in Singapore stated, "It was found that the cockroach changes its leg trajectory and body posture to adapt to uneven terrain. It was also found that the foremost leg takes some function of sensors during the course of walk" [1].This is similar to what two-legged creature such as human do.

When walking there are many things that come into play, whether you are trying to implement it into a robot or not. The one that my research project is mainly focused on is balance using a delta leg robot while it is hopping. This an important factor because if this robot were to hop, but have no sense of balance, it would waste time and energy trying to pick itself back up. Clearly the robot needs to be standing up to complete the task at hand.

II. Background

In my current project there are multiple important parts that go into the robot such as the motors, the software used to control it, and circuit boards. It is important however to know some background on the field of robotics.

A robot is defined by the computer science department of Carnegie Mellon University is, "A re-programmable, multi-functional manipulator designed to move material, parts, tools, or specialized devices through various programmed motions for the performance of a variety of tasks" [2]. These robots have been around since the creation of the first industrial robot created by General Motors called "Unimate." "The Unimate robots boasted remarkable versatility for the time and could easily pour liquid metal into die casts, weld auto bodies together and manipulate 500-pound (227-kilogram) payloads" [3].This was the start of widespread use of robots.

One of the main parts of a robot is the assembly. This robot requires it to be sturdy enough stay assembled after falling down, but it also needs to be light so that it can leap off the ground, and being fairly cheap would also be a bonus making aluminum the best option.

The delta robot was created in the early 1980s by Reymond Clavel. The original intention of the delta robot was to maneuver light and small objects at high speeds. "The delta robot is a parallel robot consisting of three arms connecting at universal joints at the base"

[10]. These machines are currently used in many pick and place machinery.

The assembly of each of the delta robot's arms consists of an electromagnetic motor, an upper link and two aluminum lower links with ball joints on each side.

Motors are an important part of this design. There are many types of motors, but in this design it requires three electromagnetic motors. The physics department at Georgia State University define an electric motor as, "Electric motors involve rotating coils of wire which are driven by the magnetic force exerted by a magnetic field on an electric current. They transform electrical energy into mechanical energy" [4]. A diagram on how this motor works is located below.

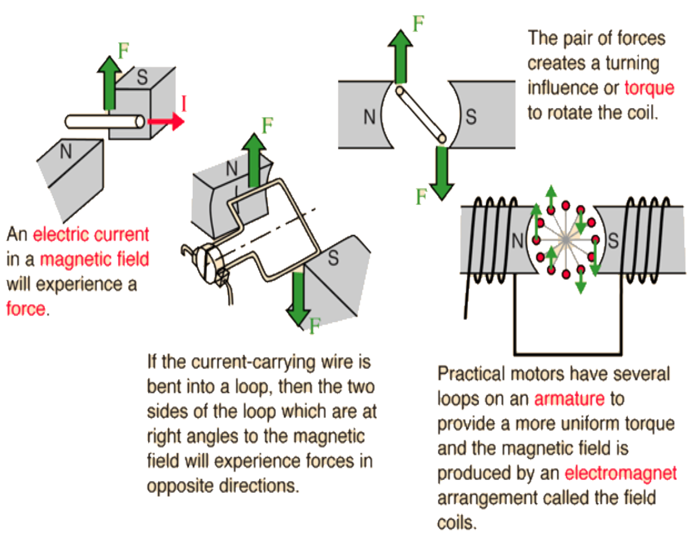

Figure 1: How an electromagnetic motor works [5]

Connected to the motors are the circuit boards. A circuit board defined by Webopedia is, "a thin plate on which chips and other electronic components are placed" [6]. In this device an expansion board would be used because the expansion board is for connecting a circuit board to a computer expansion slots, such as a USB slot. While the circuit boards are connected to the computer through USB cables, to control the motor position, a bit of programming is needed. The programming language planned on being used for this project is Python.

The final part of the process would be the design. As a delta leg robot it would have three legs and six joints [7]. The three legs would be connected to the same bottom base. Each of the legs' position would be controlled by one motor. The motor positions are defined by the programmed code created with the programming language Python, but this is not enough. The code most effectively used if the program knows the position of the base at any given angle. This is called forward kinematics. "The forward kinematics problem is to determine the position and orientation of the end-effector, given the values for the joint variables of the robot" [8]. These robot robots end-effectors have three degrees of freedom.

Starting from the origin of the base, each motor will have a predefined distance from origin at 0/360, 120, and 240 degrees, thus making the legs evenly spaced. Connected to the each of the motors respectively, is one sub-leg, all of which are the same length, height, and width. The opposite ends of these sub-legs are screwed to another sub-leg of equal measurements. The ends of those sub-legs are connected to a triangle base. Each leg has two joints, one at the motor and one at the connection point of the sub-legs. Each joint has one degree of freedom. The end result is that the entire device has three degrees of freedom based on how the motor is moved.

The delta leg robot has been used in multiple industries, for example the Flex picker [9] used in the pancake industry, and it was used to stack pancakes. According RG Luma Automation switching to these robots created these benefits: 20% increase cycle times, dramatically reduced turnaround times, improved workplace health and safety, and due to the integrated vision system, overlapping was made possible.

Figure 2: Pick and Place Machines: The Flexpicker. [9]

The problem is how would one make the robot land balanced every time? The simplest way would be to add a tail to the robot shift the center of mass somewhere else rather than the top of the robot.

To create the delta-leg robot the materials needed are two bases, made with the Computer Aided Design of Softworks, a socket for the boon, three millimeter screws at varying in length, three circuit boards used as motor controllers, a main circuit board to control the others, a circuit board for the battery, a twenty-five volt battery, six fourteen millimeter rod ends, and a triangular base.

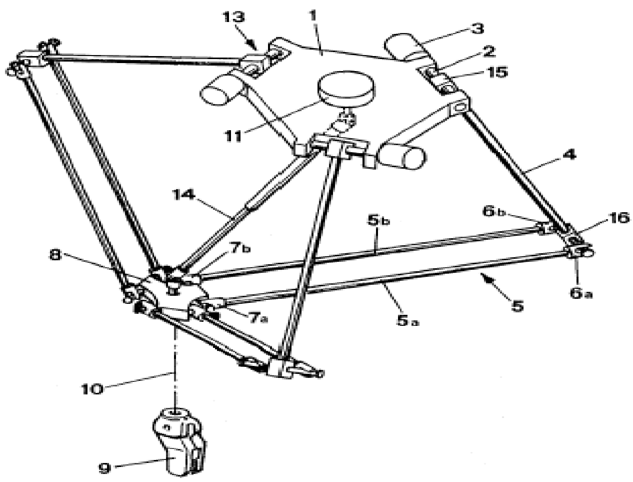

Figure 3: Patent for the delta robot from the early 1980s.

Once all the pieces are assembled correctly the next step is calibrate the motor so that they can spin and change directions quickly. Once the motor are calibrated the motor now need to be programmed so that the position "0" will be horizontal with the part it will be attached to. To figure this out, a person would go on the computer and run the code for that robot to constantly get the position of the motors. After this all the materials are put together correctly. At this point in time with the support of the boon the robot was able to hop around.

Next I needed to set D gains for each of the set P gains. The P stands for proportional which defines how much power are you putting into the motor. The D stands for derivative which works against the P gain to slow it down and resist it. This was necessary because without a D gain the motor moving to a specific position would overshoot by a noticeable amount. For the P-gains from 0.5 to 2 I used with a corresponding D gain that did not make the motors overshoot.

This robot has four stages, flight, touchdown, bottom, and takeoff. Flight is whenever the robot is in the air. Touchdown detection is when the robot touches the ground. Bottom detection is when the robots motors are most compressed. Takeoff is the stage right after bottom when the robot pushes itself into the air.

For the robot to be able to jump by itself the next steps needed were touchdown detection and bottom detection. Touchdown detection was located after the dramatic downward spike in velocity. This occurs because as the robot is about to touch the ground the motor will go up in position due to the speed that they are coming down from. To record this, a LED will shine when a certain velocity is reached; in this case it was when the absolute value of the velocity was greater than three. The light also had to shine with a very short reaction time, preferably less than twenty milliseconds. To make the reaction time shorter the range in which the robot velocity needed to reach had to be altered. Bottom detection occurs right after the touchdown and when the velocity equals zero. When the robot's velocity is zero and goes from negative to positive, the robot is about to switch directions. During this time another LED would light up in under twenty milliseconds after the range was reached. After the robot bottoms takeoff is when the robot leaves the ground.

III. Results and Conclusions

In experiments with the Delta hopper with the help of the boon the robot is able hop around multiple times without failure. Unfortunately many of the motor controllers continuously turn of while the robot is hopping. When this happens the motors tend to make the rods go under the motor and get stuck while the robot is trying to hop. This causes it to strain the rods and can start to bend them if the problem is not fixed. For the robot to be able to hop without any assistance the robot would need use the touchdown detection to find out where it needs put its leg next so that it can continue to hop.

References

[1]. Shaoping Bai, K. H. Low and Weimiao Guo. "Kinematographic Experiments on Leg Movement and Body Trajectories of Cockroach Walking on Different Terrain" Internet: http://ieeexplore.ieee.org/stamp/stamp.jsp?tp=&arnumber=846420. April 2000[June 26, 2014].

[2] "What is Robotics?" Internet: http://www.cs.cmu.edu/~chuck/robotpg/robofaq/1.html. August 1996. [June 25, 2014]

[3] Lamb Robert. "How have Robots Changed Manufacturing." Internet: http://science.howstuffworks.com/robots-changed-manufacturing.htm. [June 25, 2014]

[4] "Electric Motors." Internet: http://hyperphysics.phy-astr.gsu.edu/hbase/magnetic/elemot.html [June 25, 2014]

[5] "How does an electric motor work?" Internet: http://hyperphysics.phy-astr.gsu.edu/hbase/magnetic/mothow.html [June 25, 2014]

[6] “Printed Circuit Board” Internet:
http://www.webopedia.com/TERM/P/printed_circuit_board.html
[June 26, 2014]

[7] “Delta Robot Kinematics” Internet:
http://forums.trossenrobotics.com/tutorials/introduction-129/delta-robot-kinematics-3276/ July 27, 2009 [June 25, 2014]

[8] “FORWARD KINEMATICS: THE DENAVIT-HARTENBERG CONVENTION” Internet: http://www.ro.feri.uni-mb.si/predmeti/robotizacija/knjiga/kinematika.pdf [June 26, 2014]

[9] “Delta Robot Kinematics” Internet:
http://forums.trossenrobotics.com/tutorials/introduction-129/delta-robot-kinematics-3276/ July 27, 2009 [June 25, 2014]
[10] “Delta Robot” Internet: http://en.wikipedia.org/wiki/Delta_robot
[August 7, 2014]